UNIVERSITY OF LIÈGE

DOCTORAL THESIS

Characteristics of Jupiter's Polar Auroral Bright Spot based on Juno in situ and Remote Sensing Observations

---

by
Kamolporn HAEWSANTATI

Supervisor
Dr. Bertrand BONFOND
co-supervisors
Asst. Prof. Dr. Suwicha WANNAWICHIAN
Asst. Prof. Dr. Siramas KOMONJINDA

A thesis submitted in fulfillment of the requirements
for the degree of Doctor of Philosophy in Science
Specialization in Space Sciences

in the

Laboratory for Planetary and Atmospheric Physics (LPAP)
Department of Astrophysics, Geophysics, and Oceanography

Academic Year 2021-2022

Presented on September 2, 2022 in front of the jury members:

President:	
Assoc. Prof. Dr. Duangmanee WONGRATANAPHISAN	Chiang Mai University
Secretary:	
Prof. Dr. Denis GRODENT	University of Liège
Members:	
Dr. Bertrand BONFOND	University of Liège
Asst. Prof. Dr. Suwicha WANNAWICHIAN	Chiang Mai University
Asst. Prof. Dr. Siramas KOMONJINDA	Chiang Mai University
Prof. Dr. David RUFFOLO	Mahidol University

Statement of originality

I, Kamolporn HAEWSANTATI, declare that this thesis titled, "Characteristics of Jupiter's Polar Auroral Bright Spot based on Juno in situ and Remote Sensing Observations" and the work presented in it are my own. I confirm that this work was done wholly or mainly while in candidature for a research degree at this University. This thesis contains no materials that have been previously published or written by other people, or accepted for any other academic degree or diploma in any university or any other educational institution. Where I have quoted from the work of others, the source is always given. I have acknowledged all main sources of help.

The thesis has been submitted to Chiang Mai University and the University of Liège as part of a joint Doctoral Degree.

Abstract

This work focuses on the dynamics of one particular auroral feature in Jupiter's polar region, which we call Jupiter's polar auroral bright spot. The bright spot emission usually appears as a compact shape, which is very bright in UV aurorae. It was suggested to be the signature of the magnetospheric cusp and reconnection on the dayside magnetosphere, which is probably associated with the open magnetic field lines connecting to the solar wind. However, the importance of dayside reconnection to the Jovian magnetosphere is still a debated topic. Therefore, the dynamics and processes related to this feature are still unclear. The spacecraft of the recent NASA Juno mission was designed to fly on polar orbit around Jupiter. Juno's observations thus allow us to make in situ observations with various types of instruments over both poles in very close detail. In addition, Juno can observe Jupiter's nightside aurora, which cannot be observed by Earth-based instruments. We believe that Juno's observations provide important information which help us to better understand the bright spot emission and Jupiter's polar aurorae. In this work, the Juno observations provide detailed information on the bright spot feature.

Firstly, to analyze the bright spot characteristics, we used the data from the first 25 perijoves, observed by the Ultraviolet Spectrograph (Juno-UVS) from August 27, 2016, to May 29, 2019. Here we study their power emissions, sizes, positions, and local times in the ionosphere and their mapped positions and local times in the magnetosphere. The bright spot area is identified by the compact shape whose intensity is greater than twice the standard deviation above the background intensity. The elliptical fit was applied to determine the size of emissions. We found that the bright spot's power is in the range of gigawatt, while some spots exhibit power up to a hundred gigawatts. The bright spots are found to be located in various SIII longitudes corresponding to various local times, which means that the bright spots do not appear at only noon magnetic local times. Moreover, the bright spots are generally located at the edge of the swirl region, where high-energy particles are usually found. In addition, the bright spots tend to appear in the region with a magnetic field strength greater than 8 Gauss. The mapped positions and local times in the magnetosphere vary as well. These results could exclude the relationship of the bright spot with the noon-magnetospheric cusp process. However, Jupiter's magnetosphere is more complicated than we thought. The magnetic field can be twisted, implying that the noon magnetic local time might map to a position surprisingly distant from expectations based on a simple dipole assumption (Zhang et al., 2021). Therefore, the role of the magnetospheric cusp process needs further investigation to be confirmed or invalidated. The most interesting result is the reappearance of the bright spot with a time interval of 3 to 47 minutes between two consecutive brightenings. In addition, the bright spot in each perijove usually reappears at almost the same SIII position, implying the corotation of the plasma source with Jupiter. For the bright spot series found in PJ4 and PJ16, in which the observation sequence was long enough to see the bright spot recurring at the same SIII position, the analysis shows that the bright spots found in PJ4 and PJ16 reappear with the periods of 28 and 23 minutes, respectively. This periodicity is reminiscent of the periods observed in auroral radio and X-ray pulsations, which should be studied in deep detail in the future.

In addition, we found that there are three events in which the Juno positions according to the JRM09 magnetic model were above the bright spot positions. We assume that the spacecraft and bright spot emissions are connected by the same magnetic field line. Two cases were found from the first 25 perijoves, a northern spot observed during PJ3 and a southern spot observed during PJ15. An additional bright spot with the same characteristics is the southern spot found in PJ33. Juno carries many instruments for observing Jupiter's

magnetosphere and Jupiter's aurorae. Considered together, the observations from such instruments provide crucial information for understanding the mechanics related to the bright spot emissions. The particle observations provide characteristics of particles related to auroral emissions. The data of the plasma waves and magnetic field-aligned currents suggest some ionospheric-magnetospheric dynamics related to auroral emissions. Hence, we perform a comparison between the data of bright spot emission observed by UVS remote sensing and the in situ measurements of particles, waves, and currents, observed with JEDI, Waves, and MAG, respectively. During the bright spot detection time, the waves are travelling upward and propagate in Whistler-mode. Particles are dominated by upgoing electrons, suggesting that Juno is above the acceleration region where the downgoing particles in the opposite direction probably propagate down and cause the aurora. Two of three cases (in PJ3 and PJ33) show that the intensification of upward Whistler-mode waves and upward electron enhancement simultaneously occurred, suggesting the presence of waves-particle interaction. The PJ3 spot was also detected during waves-particles enhancement, while the PJ33 spot was detected a few minutes later. The PJ15 event shows that the upgoing Whistler-mode was first detected, followed by bright spot detections and some particle enhancements at the end. However, the signature of magnetic field-aligned currents is less significant. We propose that the imperfection of the magnetic mapping model is the main source of the time mismatch between the wave, particle, and bright spot detection. Even though the times do not exactly match, which may simply be due to the JRM09 mapping errors, we believe that the wave-particle interactions play the main role in accelerating particles causing the bright spot emissions. However, other processes may also play a role in causing the bright spot, such as the magnetic reconnection near Jupiter's polar magnetosphere (Masters et al., 2021) and the broadband acceleration due to the presence of an ionospheric Alfvén resonator (Lysak et al., 2021).

Résumé

Ce travail se concentre sur la dynamique d'une structure aurorale particulière dans la région polaire de Jupiter, que nous avons simplement appelée tache aurorale polaire brillante, ou plus simplement tache brillante. Les émissions de la tache brillante apparaissent généralement comme une forme compacte, qui est très brillante dans les aurores UV. Il a été suggéré qu'il s'agissait de la signature du cornet polaire magnétosphérique et de la reconnexion de la magnétosphère côté jour, qui est probablement associée aux lignes de champ magnétique ouvertes se connectant au vent solaire. Cependant, l'importance de la reconnexion diurne pour la magnétosphère jovienne est encore un sujet amplement débattu. Par conséquent, la dynamique et les processus liés à cette caractéristique ne sont toujours pas clairs. La sonde spatiale de la mission récente NASA-Juno a été conçue de manière à suivre des orbites polaires autour de Jupiter. Les observations de Juno nous permettent ainsi d'obtenir des observations in situ très détaillée avec différents types d'instruments aux deux pôles de Jupiter. En outre, Juno peut observer les aurores nocturnes de Jupiter, qui ne peuvent être observées par les instruments proches de l'orbite terrestre. Les observations de Juno fournissent des informations importantes qui nous aident à mieux comprendre l'émission de cette tache brillante et des aurores polaires de Jupiter en général. Dans ce travail, les observations de Juno fournissent des informations très détaillées de la tache brillante. Tout d'abord, pour analyser les caractéristiques des différentes occurrences de la tache brillante, nous avons utilisé les données des 25 premiers périjoves, observés par le spectrographe ultraviolet (Juno-UVS) du 27 août 2016 au 29 mai 2019. Nous étudions ici leur puissance émise, leur taille, leur position et leur temps local dans l'ionosphère, ainsi que leur position cartographiée et leur temps local dans la magnétosphère. La zone sous-tendue par la tache brillante est identifiée à une forme compacte dont l'intensité est supérieure à deux fois l'écart-type de l'intensité de fond. L'ajustement elliptique a été appliqué pour déterminer la taille de la région d'émission. Nous avons constaté que la puissance du point lumineux est de l'ordre du gigawatt, bien que cette puissance puisse aller jusqu'à cent gigawatts. La tache brillante apparait à diverses longitudes SIII et diverses heures locales, ce qui signifie que la tache brillante n'apparait pas seulement à midi magnétique. De plus, la tache brillante est généralement située au bord de la région de tourbillon (« swirl region »), où l'on trouve habituellement des particules à haute énergie. En outre, la tache brillante a tendance à apparaître dans la région où l'intensité du champ magnétique est supérieure à 8 Gauss. Les positions cartographiées et les temps locaux dans la magnétosphère varient également. Ces résultats pourraient exclure la relation entre la tache brillante et le processus magnétosphérique associé au cornet polaire, côté midi. Cependant, la magnétosphère de Jupiter est plus compliquée que nous le pensions. Le champ magnétique peut être tordu, ce qui implique qu'un point situé à midi en temps local magnétique pourrait se trouver fort éloigné de la position attendue dans l'hypothèse d'un dipole simple (Zhang et al., 2021). Par conséquent, le rôle du processus lié au cornet polaire magnétosphérique doit être étudié plus avant pour être confirmé ou infirmé. Le résultat le plus intéressant est la réapparition de la tache brillante avec un intervalle de temps de 3 à 47 minutes entre deux embrillancements consécutifs. De plus, la tache brillante dans chaque périjove réapparaît habituellement à presque la même position SIII, ce qui implique la corotation de la source de plasma avec Jupiter. Pour la série de taches brillantes trouvées dans PJ4 et PJ16, dans laquelle la séquence d'observation était suffisamment longue pour voir la tache brillante réapparaître à la même position SIII, l'analyse montre que la tache brillante trouvée dans PJ4 et PJ16 réapparait avec des périodes de 28 et 23 minutes, respectivement. Cette périodicité est à mettre en relation avec les périodes du même ordre de grandeur observées dans les pulsations aurorales radio et X, qui devraient être étudiées en détail à l'avenir. En outre, nous

avons constaté qu'il y a trois événements dans lesquels les positions de Juno selon le modèle magnétique JRM09 étaient juste au-dessus de la tache aurorale polaire brillante et étaient reliés par la même ligne de champ magnétique. Deux cas ont été trouvés à partir des 25 premiers périjoves, un au nord observé pendant PJ3 et un au sud observé pendant PJ15. Une autre tache brillante présentant les mêmes caractéristiques est observée au sud lors de PJ33. Juno embarque de nombreux instruments pour observer la magnétosphère de Jupiter et les aurores de Jupiter. Considérées dans leur ensemble, les observations de ces instruments fournissent des informations cruciales pour la compréhension des mécanismes liés à l'émission de la tache aurorale polaire brillante. Les observations des particules fournissent les caractéristiques des particules liées aux émissions aurorales. Les données sur les ondes de plasma et les courants alignés sur le champ magnétique apportent des informations sur la dynamique ionosphère-magnétosphère liée aux émissions aurorales. Par conséquent, nous effectuons une comparaison entre les données d'émission de la tache brillante observées par télédétection UVS et les mesures in situ des particules, des ondes et des courants, observées respectivement par JEDI, Waves et MAG. Pendant le temps de détection de la tache brillante, les ondes se déplacent vers le haut et se propagent en mode Whistler. Les particules sont dominées par des électrons ascendants, ce qui suggère que Juno se trouve au-dessus de la région d'accélération où les particules descendantes dans la direction opposée se propagent probablement vers le bas et provoquent l'aurore. Deux des trois cas (dans PJ3 et PJ33) montrent que l'intensification des ondes ascendantes en mode Whistler et l'augmentation des électrons ascendants se sont produites simultanément, ce qui suggère l'existence d'une interaction onde-particule. Le spot PJ3 a également été détecté pendant l'intensification des interactions onde-particule, tandis que le spot PJ33 a été détecté quelques minutes plus tard. L'événement PJ15 montre que le mode Whistler ascendant a été détecté en premier, suivi par des détections de la tache brillante et quelques renforcements des flux de particules. Cependant, la signature des courants alignés le long du champ magnétique est moins significative. Nous proposons que l'imperfection du modèle de cartographie magnétique soit la principale source du décalage temporel entre la détection des ondes, des particules et de la tache brillante. Même si les temps ne correspondent pas exactement, ce qui peut être simplement dû aux erreurs de cartographie de JRM09, nous pensons que les interactions onde-particule jouent le rôle principal dans l'accélération des particules causant les émissions de la tache brillante. Cependant, d'autres processus peuvent également jouer un rôle dans cette émission, comme la reconnexion magnétique près de la magnétosphère polaire de Jupiter (Masters et al., 2021) et l'accélération à large bande due à la présence d'un résonateur d'Alfvén ionosphérique (Lysak et al., 2021).

Acknowledgements

The PhD journey is a very challenging mission. Every step I have taken during my PhD period is a great test that I would never have gotten through if I had had no support from everyone around me. In particular, this thesis would not have been possible without the fruitful supervision and contributions of many people. I would therefore like to express my sincere gratitude to all of those who made my PhD life complete.

Foremost, I would like to thank my supervisors, Asst. Prof. Dr. Suwicha Wannawichian and Dr. Bertrand Bonfond, for all their support, comments, and kindness for giving me the opportunity to take the double degree programs at Chiang Mai University (Thailand) and the University of Liège. My special thanks to Dr. Suwicha for her understanding and her kind help in every step since I started this work. I would also like to thank Dr. Bertrand for accepting me into the LPAP group and for his kindness in teaching me how to be a great researcher. I appreciate being supervised by both of them.

My sincere thanks also go to my co-advisor, Asst. Prof. Dr. Siramas Komonjinda, who always understands and supports this study. I would like to heartily thank Prof. Denis Grodent and Dr. Zhonghua Yao for providing me with constructive comments to improve my work. A special thanks to Randy Gladstone and the UVS team for letting me join the meeting group and giving me the opportunity to share and discuss ideas until my articles were published. I would like to thank the jury members, Assoc. Prof. Dr. Duangmanee Wongratataphisan, Prof. Denis Grodent, and Prof. David Ruffolo, for agreeing to be on the jury and giving me comments and suggestions to improve this thesis. I would like to acknowledge the NASA Juno mission for providing the data set and Marissa Vogt for her permission to use the Jupiter ionosphere/magnetosphere mapping program.

I would also like to thank all staff members at the Astronomical Laboratory, Chiang Mai University, and LPAP, STIR institute, University of Liège, for their assistance in providing facilities and materials for my studies. Moreover, I would like to thank the Science Achievement Scholarship of Thailand (SAST) for the financial support. This work was also supported by the National Astronomical Research Institute of Thailand (NARIT) and the Department of Physics and Materials Science, Chiang Mai University.

Last but not least, I would like to warmly thank my family for their encouragement and support throughout the entire duration of my studies.

Contents

List of Figures

List of Tables

To my family

Chapter 1

Introduction

1.1 Motivation and Research Objectives

Jupiter is known as the largest gas planet in the solar system. The equatorial radius (R_J) is approximately 71,492 km (with the polar radius of 66,854 km (Weiss, 2004)), which is about 11 times greater than Earth's radius. Jupiter's average distance from the sun is 5.2 astronomical units (AU), where 1 AU = 1.496×10^{11} m. Jupiter's core is composed of a large layer of metallic hydrogen, which is electrically conducting fluid. Jupiter's rotation period is 9 h 55 min (Weiss, 2004) which is very fast for its large size. As a result, the fast rotation of conducting fluid generates a strong magnetic field with magnetic field strength at the surface up to 20 Gauss (1 Gauss = 10^{-4} T), while the Earth's magnetic field is only 0.6 Gauss. Combined with the large internal plasma source, a unique magnetosphere in the solar system is formed. The planetary magnetosphere is defined as the region around a planet dominated by the planetary magnetic fields. Auroral emissions are the result of collisions between atmospheric particles and accelerated charged particles guided towards the poles by the magnetic field lines. Jupiter's Ultraviolet (UV) aurorae have been studied for decades. The first UV spectrum image of Jupiter's aurorae was taken in 1979 by Voyager 1 during its encounter (Clarke et al., 2004 and references herein). Theoretical studies, modeling, and numerous observations, particularly from the Hubble Space Telescope's ultraviolet cameras, have substantially improved our understanding of Jupiter's aurora. However, the need for clear interpretation and many outstanding questions remains due to the complicated Jovian system and lack of in-situ measurements across the poles. While Earth's aurorae are clearly understood to be mainly caused by the solar wind particles penetrating the atmosphere, the dominating plasma particles for causing Jupiter's aurorae come from the source inside Jupiter's magnetosphere. In addition, there are bright emissions inside Jupiter's polar region, which for Earth it is mostly dark. That is one reason why Jupiter's polar aurora is poorly understood even though there are many interesting features. One particular auroral feature in Jupiter's polar region is Jupiter's polar auroral bright spot. It usually appears as a compact shape, which is very bright in UV aurorae. The bright spot was suggested by Pallier and Prangé, 2001 to be the signature of Jupiter's polar cusp, the region where external plasma particles can penetrate the planetary atmosphere. However, this suggestion is based on the results from Earth-based observations that are limited by viewing geometry and observation time. Therefore, the clear responsible process for causing the bright spot emissions is still in debate.

In 2011, the Juno spacecraft, the mission under the operation of National Aeronautics and Space Administration (NASA), was sent to closely observe Jupiter in detail. Goals of this mission are to understand the origin and the evolution of Jupiter, to look for the solid planetary core, to map the magnetic field, to measure water and ammonia in the deep atmosphere, and to observe the aurorae. This is a good chance to reveal information for solving the debated questions about Jupiter's magnetosphere and aurorae. Juno was launched on August 5th, 2011, and performed the Jupiter orbital insertion (JOI) on July 4th, 2016.

The interplanetary observation was started on May 15th, 2016 before encountering Jupiter's magnetosphere. The prime mission comprises 36 polar orbits and an additional 40 orbits during the extended mission. Juno trajectory is a highly elliptical (e=0.98) polar orbit with a 53−day period. The closest approach (perijove) is at an altitude below 8,000 km, between Jupiter's upper atmosphere and the main radiation belt, while the apojove is at the distance of $\sim$ 113 R_J (Bolton et al., 2017). The aurorae in each hemisphere are observed for a few hours during the perijove. However, the oblateness of Jupiter causes the orbit precession to grow by $\sim 1^\circ$ per orbit, as well as a $\sim 0.9^\circ$ closer to the equatorial crossing in each orbit (Bagenal et al., 2017). As a consequence, the observation time for the northern hemisphere decreases in later perijoves. Juno started the polar science orbits with nine instruments onboard the spacecraft. Five instruments are designed to study Jupiter in high latitude regions which can reveal the information for unresolved questions related to Jupiter's aurorae.

Hence, with the completed set of instruments on board the Juno spacecraft and the advantage of polar orbit which allows studying Jupiter in very close detail, we focus on studying the variations of the bright spot emissions including investigation of the possible sources of the precipitating particles related to this auroral feature and its dynamics. This thesis comprises two studies. The first investigation in this thesis focuses on the UV auroral images provided by the UV spectrograph, one of five instruments mentioned above. We study the power emission, the position and local time, the time variation of its location and emitted power. The second work combines data from other instruments for further discussions of the associated particles and waves during the bright spot emissions. The main scientific objectives of the study can be divided into two topics as follows:

- Try to understand the origin of the bright spot through a detailed study of the spatial and temporal characteristics of the bright spot in the UVS dataset, which avoids the selection bias for previous observations (HST).
- To investigate the sources and dynamics of precipitating particles that are related to the variability of the polar auroras.

The first study focuses on the characteristics of the bright spot emission. The study includes studying the time variation of their emitted power and the locations in the ionosphere. Moreover, the magnetic local times are studied by mapping in the equatorial plane along magnetic field lines. The study of the magnetic local time of the auroral bright spot could possibly suggest sources of the emission. The magnetic local times are used since Jupiter's magnetic field is complicated and doing otherwise would lead to absurd conclusions. I developed the software to obtain the intensity of bright spot emission from UVS instrumental count rate. The latitudinal and longitudinal positions of auroral features in the ionosphere are indicated based on the instrument's and Jupiter's position at the observing time. The mapped location of auroral emissions in the magnetosphere and local times corresponding to these features is obtained using the Jupiter Ionosphere/Magnetosphere mapping model based on Vogt et al., 2011; Vogt et al., 2015 with the SIII latitude and longitude of auroral emission and subsolar longitude as input parameters.

The second work relies on the second objective which is to investigate the sources and dynamics related to the bright spot emissions. I particularly focus on three cases where particles and waves data were observed by the in-situ observations simultaneously with the remote sensing observations of bright spot emissions. This study investigates the relation between particle energy flux and wave data with the bright spot emissions. The results will provide more understanding of the sources of auroral activities in Jupiter's polar region. The information can be applied to study other gas giants, which is very useful for a better understanding of the dynamics of plasma and waves in the planetary atmospheres.

In this study, the position of bright spot emissions is described by the System III (SIII) coordinates. This is the left-hand coordinate, in which the longitude increases from dusk

through noon to the dawn side. This coordinate is the Jupiter rotating frame defined by the rotation period of decametric radio. The longitude on SIII along the Earth-Jupiter vector is called the Central Meridian Longitude (CML). The $z-$axis is defined by the Jupiter spin axis. The $x-$axis corresponds to 0° SIII longitude or prime meridian, which is defined as the CML on a specific date in 1965. The $y-$axis is orthogonal to the $x-$ and $z-$ axes completing the left-hand system.

1.2 An Overview of Space Plasma Related to Aurorae

This section describes the behaviors of plasmas which contain electrically charged particles traveling along the magnetic field lines toward Jupiter's pole. The study of a single particle helps us to understand the behaviors of a particle under the influences of electric and magnetic fields. Moreover, the fluid approach will provide a further understanding of the characteristics of these particles on a big scale including their connections with the Jupiter magnetosphere.

1.2.1 Single Particle Motion

To study particle behaviors under the influence of magnetic and electric fields, the equation of motion is derived from the Lorentz force law. The Lorentz force $\mathbf{F}_L$ acts on a particle with charge q, while traveling with velocity $\mathbf{v}$ in the electric field $\mathbf{E}$ and the magnetic field $\mathbf{B}$, is given by

$$\mathbf{F}_L = m\frac{d\mathbf{v}}{dt} = q\left[\mathbf{E} + (\mathbf{v} \times \mathbf{B})\right]. \tag{1.1}$$

The simplest form of this equation is, the electric field is absent, or relatively weak, ($\mathbf{E} = 0$), and the magnetic field is uniform along the z direction ($\mathbf{B} = B\hat{z}$). Equation 1.1 can be separated into three components as follows:

$$m\frac{dv_x}{dt} = qBv_y, \quad m\frac{dv_y}{dt} = -qBv_x, \quad m\frac{dv_z}{dt} = 0. \tag{1.2}$$

The second derivative in x and y axes are rearranged by substitution $\frac{dv_x}{dt}$ and $\frac{dv_y}{dt}$ from equation 1.2;

$$\frac{d^2v_x}{dt^2} = -\left(\frac{qB}{m}\right)^2 v_x, \quad \frac{d^2v_y}{dt^2} = -\left(\frac{qB}{m}\right)^2 v_y, \quad m\frac{d^2v_z}{dt^2} = 0. \tag{1.3}$$

The equation for x and y axes describe a simple harmonic oscillator with the angular frequency of $\frac{|q|B}{m}$. This parameter is called gyro frequency or cyclotron frequency defined as;

$$\Omega_c = \frac{|q|B}{m}. \tag{1.4}$$

Defining the Larmor radius (or cyclotron radius or gyroradius) by

$$r_c = \frac{v_\perp}{\Omega_c} = \frac{mv_\perp}{|q|B}, \tag{1.5}$$

where $v_\perp$ is a velocity component perpendicular to the magnetic field. The solutions for equation 1.3 are

$$x - x_0 = r_L \sin \Omega_c t, \quad y - y_0 = \mp r_L \cos \Omega_c t, \quad z - z_0 = v_\parallel t, \tag{1.6}$$

where $v_\parallel$ is a velocity component parallel to **B**. The above equations describing a particle's position in x and y components imply that a charged particle moves in a circular motion around the guiding canter (x_0, y_0) with Larmor frequency Ω_c and Larmor radius r_c. The particle also travels along the $z-$axis with a constant velocity. Hence, a charged particle travels with a motion called gyromotion, appearing as a helix trajectory. With the different signs and mass of charged particle species, electrons will travel with a smaller radius and in the opposite direction from ion species. The angle between charge velocity and magnetic field vector is called "*pitch angle*", defined by

$$\alpha = \sin^{-1}\left(\frac{v_\perp}{v}\right). \tag{1.7}$$

This quantity describes the direction of the charged particle during its motion along the magnetic field line. The pitch angle $\alpha = 0^\circ$ means that the particle travels without gyromotion, only traveling along the magnetic field line, pitch angle $\alpha = 90^\circ$ means that particle motion is circular without moving along the magnetic field line, and pitch angle $\alpha = 180^\circ$ refers to no gyromotion, while particle travels in the opposite direction to the magnetic field line. The illustration of gyromotion in a uniform magnetic field and the pitch angle are shown in Figure 1.1.

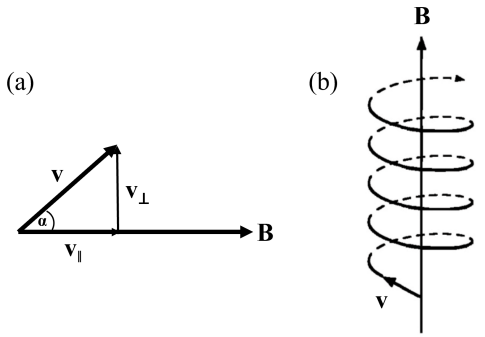

FIGURE 1.1: (a) Schematic diagram of pitch angle and related velocity components. (b) Schematic diagram of gyromotion of positive charge (ion particle) in a uniform magnetic field. (Tsurutani and Lakhina, 1997).

However, it is possible that the electric and magnetic fields are not uniform. For simplification, the electric field is again assumed to be zero and the magnetic field varies as a function of position. The common studies for the nonuniform magnetic fields are 1) the $\nabla B \perp \mathbf{B}$, which caused a grad$-B$ drift velocity, 2) a curvature magnetic field with a constant radius causing a curvature drift which is important for a charged particle motion in the ring current region, and 3) the $\nabla B \parallel \mathbf{B}$ which is a configuration in the planetary magnetic field at the pole. Here we discuss only the last type of nonuniform field.

Assuming that the magnetic field's direction is along the z axis, and magnetic field strength increases as the distance z increases. This time, the magnetic field is considered in cylindrical coordinates;

$$\mathbf{B} = B_r \hat{r} + B_z \hat{z}. \tag{1.8}$$

Then $\nabla \cdot \mathbf{B} = 0$ according to Maxwell's equation, which can be written as

$$\begin{aligned} \nabla \cdot \mathbf{B} = \frac{1}{r}\frac{d}{dr}(rB_r) + \frac{dB_z}{dz} = 0, \\ \frac{d}{dr}(rB_r) = -r\frac{dB_z}{dz}. \end{aligned} \tag{1.9}$$

At position close to $z-$axis (r$\approx$0), $B_r << B_z$;

$$B_r \cong -\frac{1}{2}r\frac{dB_z}{dz}. \tag{1.10}$$

A magnetic moment of gyrating particle is defined as

$$\mu = \frac{1}{2}\frac{mv_\perp^2}{B}. \tag{1.11}$$

In a static magnetic field, the magnetic moment remains nearly constant. This quantity is called the first adiabatic invariant, which is initially derived from the conservation of angular momentum along a completed path of one gyroperiod. Assuming that particle moves with perpendicular velocity $v_{\perp 0}$ from an initial z_0 position, in which magnetic field strength is B_0, to a position where the perpendicular velocity and magnetic field strength change to $v_\perp$ and B, respectively. The invariant of the magnetic moment shows that

$$\begin{aligned} \frac{1}{2}\frac{mv_{\perp 0}^2}{B_0} = \frac{1}{2}\frac{mv_\perp^2}{B}, \\ v_{\perp 0}^2 = \left(\frac{B}{B_0}\right)v_\perp^2. \end{aligned} \tag{1.12}$$

The above relation implies that if a charged particle travels toward a region of a stronger magnetic field (i.e., from the equator to the pole), the perpendicular velocity ($v_\perp$) will increase. Consider the conservation of energy where kinetic energy is dominant;

$$\begin{aligned} \frac{1}{2}mv^2 = \frac{1}{2}m\left(v_\perp^2 + v_\parallel^2\right) = const., \\ v^2 = v_\perp^2 + v_\parallel^2 = const. \end{aligned} \tag{1.13}$$

The stronger magnetic field results in faster $v_\perp$, but slower $v_\parallel$. Eventually, the parallel velocity reduces to zero and the particle starts to travel back in the opposite direction. This motion is called the *magnetic mirror*. The reflection of a particle gyrating around the $z-$axis, i.e., with $r = r_c$, can be explained by considering the Lorentz force in a component parallel to the axial magnetic field;

$$\begin{aligned} F_\parallel &= q\left(\mathbf{v} \times \mathbf{B}\right)_z = qv_\perp B_r \\ &= -\frac{1}{2}qv_\perp r_c\frac{dB_z}{dz} \\ &= -\frac{1}{2}qv_\perp r_c \nabla B_z, \end{aligned} \tag{1.14}$$

where B_r is replaced by equation 1.10. Where $\nabla B_z > 0$, $F_\parallel < 0$, causing $v_\parallel$ to decrease. Finally, when $v_\parallel = 0$, this force will therefore cause a particle to move backward.

By considering that $v_\perp = v \sin\alpha$, equation 1.12 can be rewritten as

$$\sin^2\alpha = \left(\frac{B}{B_0}\right)\sin^2\alpha_0, \tag{1.15}$$

where $\alpha = 90^\circ$ is the pitch angle at a position at which the magnetic mirror occurs, $v_\perp$ reaches the maximum value and $\sin\alpha = 1$. The magnetic field strength at this point is $B_m = B_0/\sin^2\alpha_0$. Figure 1.2 shows the magnetic field structure where particle moves from a position with B_0 toward a region of B_m.

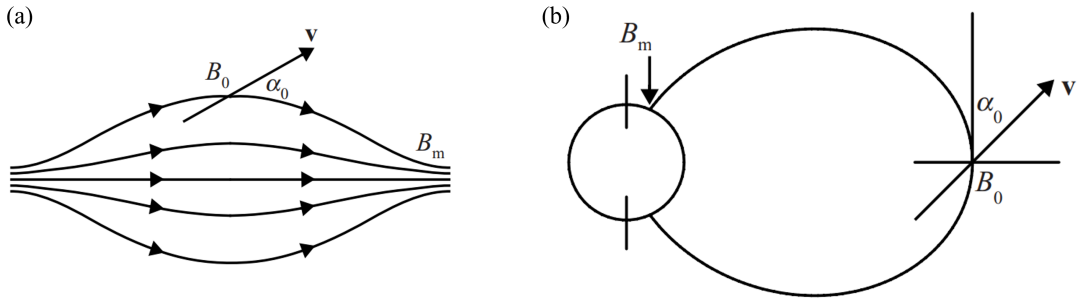

FIGURE 1.2: (a) Schematic diagram of magnetic field structure showing magnetic field strength B_0 in the middle where particle starts traveling with pitch angle α_0 toward a mirror point where the maximum magnetic field strength is B_m. Panel (b) Schematic diagram shows the same condition in the planetary magnetic field (Gurnett and Bhattacharjee, 2005b).

Once a particle reaches a mirror point, the particle returns to the z_0 position again and passes to another point, in which magnetic field strength is also B_m (i.e., a particle mirrored at a magnetic pole, then passing the equator to another pole). The particle is therefore confined in a magnetic field by traveling back and forth between the magnetic mirror points. This situation is called the *magnetic bottle*. A criterion of initial pitch angle for the confinement in the magnetic bottle is

$$\alpha_0 > \sin^{-1}\left(\frac{B_0}{B_m}\right)^{1/2}. \tag{1.16}$$

However, for a charged particle, whose initial pitch angle at z_0 is less than the minimum pitch angle as described by equation 1.16, the particle will still have a $v_\parallel$ component at a point of magnetic field strength B_m. Hence, a particle can escape the magnetic bottle. The particles, whose initial pitch angles do not meet the criteria of minimum pitch angle explained by equation 1.16, will be in a region called the *loss cone* in the velocity space. These particles can then penetrate the magnetic bottle's confinement and penetrate into the planetary atmosphere and cause auroral emissions.

1.2.2 Plasma Dynamics

An example of plasma in space physics is the solar wind plasma. The typical solar wind plasma density is in the order of 10^6 m^{-3} (Chen, 2016). It is a difficult task to study plasma behavior by following an individual particle. Instead, the fluid approach is used to study the plasma properties. In this case, plasmas are treated as electrically neutral fluids, whose numbers of electrons and ions are approximately equal. The mandatory equations to study fluid dynamics are the conservation of mass, momentum, and energy. In addition, the effects of electric and magnetic fields also need to be included. Hence, the multifluid equations

are introduced, which are related to magnetohydrodynamics (MHD) equations. The set of equations used to study plasma fluids is as follows.

i) Maxwell equations

$$\begin{aligned} \epsilon_0 \nabla \cdot \mathbf{E} &= \rho_c, \\ \nabla \times \mathbf{E} &= -\frac{\partial \mathbf{B}}{\partial t}, \\ \nabla \cdot \mathbf{B} &= 0, \\ \nabla \times \mathbf{B} &= \mu_0 \left(\mathbf{J} + \epsilon_0 \frac{\partial \mathbf{E}}{\partial t} \right), \end{aligned} \tag{1.17}$$

where ϵ_0 is the permittivity of free space, μ_0 is the permeability of free space, ρ_c is charge density, and $\mathbf{J}$ is the current density.

ii) Continuity equation for each species

$$\frac{\partial \rho}{\partial t} + \nabla \cdot (\rho \mathbf{v}) = 0, \tag{1.18}$$

where $\mathbf{v}$ is the bulk plasma velocity.

iii) Momentum equation for each bulk fluid

$$\rho \left(\frac{\partial \mathbf{v}}{\partial t} + \mathbf{v} \cdot \nabla \mathbf{v} \right) = -\nabla p + \rho_c \left(\mathbf{E} + \mathbf{v} \times \mathbf{B} \right), \tag{1.19}$$

where $p = nk_B T$ is thermal pressure, and

iv) Thermodynamic equation of state

$$p = C\rho^{\gamma}, \tag{1.20}$$

where C is a constant and $\gamma = c_p/c_v$ is an adiabatic index, where c_v and c_p are the specific heat capacity at constant volume and constant pressure, respectively.

The multifluid or MHD equations are widely used to study space plasma in various aspects. This section focuses on the study of waves in plasma by fluid approach. Waves are generally caused by a perturbation in a system. Since plasmas consist of charged particles under the influences of electric and magnetic fields, plasmas can have several wave modes. The general properties for different wave types are as follows.

A general plane wave equation, for the perturbation of the electric field, is written as

$$\mathbf{E}_1 (\mathbf{x}, t) = E_1 e^{[\mathbf{k} \cdot \mathbf{x} - \omega t]}, \tag{1.21}$$

where E_1 is the amplitude of the electric field oscillation, $\mathbf{k}$ is a wave vector with wave number $k = 2\pi/\lambda$, and ω is the angular frequency. The perturbation on the magnetic field, $\mathbf{B}_1(\mathbf{x}, t)$, can be explained by an equation similar to equation 1.21. For the plane wave, a simple sinusoidal wave propagates with a phase velocity of

$$v_{ph} = \omega/k. \tag{1.22}$$

For the superposition of many plane waves, a wave packet propagates with a group velocity,

$$v_g = \frac{\partial \omega}{\partial k}. \tag{1.23}$$

The frequency ω now is a function of k, $\omega = \omega(k)$, which is called the dispersion relation. The dispersion relation is specified for each wave type and can be obtained by considering fluid equations in combination with characteristics of the wave, as well as Maxwell equations. Wave characteristics are summarized in Table 1.1, where $\mathbf{B}_0$ is a large-scale (non-oscillating) magnetic field.

TABLE 1.1: Wave characteristics (Schunk and Nagy, 2009).

Wave type	Characteristics
Electrostatic wave	$\mathbf{E}_1 \neq 0, \mathbf{B}_1 = 0$
Electromagnetic wave	$\mathbf{E}_1 \neq 0, \mathbf{B}_1 \neq 0$
Longitudinal mode	$\mathbf{E}_1 \parallel \mathbf{k}$
Transverse mode	$\mathbf{E}_1 \perp \mathbf{k}$
Parallel propagation	$\mathbf{k} \parallel \mathbf{B}_0$
Perpendicular propagation	$\mathbf{k} \perp \mathbf{B}_0$
Cut-off ($\omega \approx$ constant)	$k \to 0$
Resonance ($\omega \approx$ constant)	$k \to \infty$

Each wave type is identified to be either electrostatic or electromagnetic, and by its propagation direction (e.g., parallel or perpendicular to the background magnetic field). In addition, the oscillating species (electrons or ions) are also considered. The electrostatic waves which are commonly studied are electron plasma waves, which are also known as plasma oscillations or Langmuir waves. This wave mode is oscillated by electrons with the dispersion relation

$$\omega^2 = \omega_{pe}^2 + \frac{3}{2}k^2 v_{th}^2, \tag{1.24}$$

where $v_{th}^2 = 2k_B T_e/m$ is the electron thermal speed and ω_{pe} is the electron plasma frequency defined by

$$\omega_{pe} = \sqrt{\frac{n_0 e^2}{\epsilon_0 m_e}}. \tag{1.25}$$

An example of waves oscillated by ions is ion-acoustic waves or sound waves, the dispersion relation is defined by

$$\omega^2 = k^2 v_s^2, \tag{1.26}$$

where $v_s^2 = (\gamma_e k_B T_e + \gamma_i k_B T_i)/M$ is the ion acoustic speed.

Other common waves associated with the planetary magnetosphere are the Alfvénic waves and Whistler mode waves, which are transverse and propagate along the magnetic field ($\mathbf{k} \parallel \mathbf{B}_0$). The Alfvénic waves are low frequency ion oscillations and related to cold plasmas. The dispersion relation is

$$\omega^2 = k^2 v_A^2, \tag{1.27}$$

where $v_A = B_0/\sqrt{\mu_0 \rho_0}$ is the Alfvén velocity.

For a high frequency electron oscillation, a specific wave that will be studied in this thesis is a right-hand circular polarization or R wave. The dispersion relation is given by

$$\omega^2 = k^2c^2 + \frac{\omega_{pe}^2}{1 - (\omega_{ce}/\omega)}, \tag{1.28}$$

where $\omega_{ce} = eB_0/m_e$ is the electron cyclotron frequency. The cutoff frequency for R waves, ω_R, is given by letting $k = 0$ in equation 1.28, while the resonance ($k \to \infty$) is at $\omega = \omega_{ce}$. This means that R waves has a stop band between ω_{ce} and ω_R, but waves propagate at regions $\omega < \omega_{ce}$ and $\omega > \omega_R$. For the propagation below ω_{ce}, the wave in this low-frequency region is called *Whistler-mode waves*, which is a very important wave mode for studying the ionospheric phenomena and will be discussed in this thesis.

For charged particles that travel with circular cyclotron motion and associating with polarization waves that reach a resonance frequency, charged particles and waves can interact with each other. The condition for cyclotron resonances is $\omega - \mathbf{k} \cdot \mathbf{v} = n\Omega_c$, where n is an integer number (Tsurutani and Lakhina, 1997). When the condition is satisfied, waves and particles are in phase, and energy and momentum can be exchanged between them. A case for $n = 0$ is called Landau resonance, in which waves and particles are traveling in the same direction. This waves-particle interaction can be found in planetary atmospheric studies. Elliott et al., 2020 proposed that upward-propagating Whistler-mode waves in the Jovian polar cap are produced by the upward electron beams (inverted-Vs) via a beam-plasma instability in Landau resonance. In addition, these broadband whistler mode waves can also accelerate upward traveling electrons to high energies as well (Elliott et al., 2018b).

1.3 Jovian System

To study aurorae, the structures and dynamics of the planetary magnetosphere need to be discussed. This section describes the configuration and dynamics of the Jupiter magnetosphere in each region, which are the inner, middle, and outer magnetospheres. The models of Jupiter's magnetic field, which are commonly used to analyze auroral positions in the ionosphere and assess plasma sources related to auroral features, are discussed. Then, in the next section, a comprehensive description of Jupiter's aurorae is presented, including its morphology, dynamics, and four primary components. The last section gives details on previous observations in the polar aurorae, which is the main objective of this work.

1.3.1 Jupiter's Magnetosphere

As mentioned before, Jupiter's magnetosphere is dominated by Jupiter's magnetic field. The magnetosphere can interact with external influence, such as the solar wind interacting with planetary magnetospheres. The solar wind is released from the solar corona, which contains highly energetic plasma, frozen-in with the interplanetary magnetic field (IMF), and propagates from the Sun toward the entire solar system. Let us start our description of a magnetosphere by making a simplifying assumption, which is that the planetary magnetic field can be described as a perfect dipole. The dayside of the planet, which faces the Sun, is where the solar wind first encounters the planet. Due to the solar wind dynamic pressure, the fast-flowing solar wind will compress the magnetosphere on the dayside. The total magnetic pressure in the magnetosphere withstands this compression until it reaches the balance point between these two pressures. The stand-off region between these two pressures roughly defines the boundary of the dayside magnetosphere. The bow shock is a standing shock front that slows the supersonic solar wind plasmas to be subsonic, heated, and deflected around the planet. The shocked solar wind flows around the magnetosphere,

and partly penetrates the magnetosheath. The magnetopause is a thin current sheet that separates the solar wind plasma from the magnetospheric plasma. In this layer, the solar wind dynamic pressure and the planetary magnetic pressure are balanced. The cusp is a funnel-shaped region in which the boundary layer extends deep into the magnetosphere and magnetosheath plasma has direct access to the ionosphere.

However, the magnetic field of Jupiter is not a perfect dipole. The magnetic axis is also tilted about 9.5 degrees from the rotational axis (Connerney et al., 1998). In addition, Jupiter's magnetic field strength is stronger than Earth's magnetic field. The greatest distinction between Jupiter's magnetosphere and Earth's magnetosphere is the source of plasma particles inside the planetary magnetosphere. The majority of plasma particles inside Jupiter's magnetosphere come from the volcanic moon, Io, and, to a lesser extent, from Jupiter's atmosphere. Io and its surrounding environment provide $\sim$1 ton per second into the Jovian magnetosphere, while the solar wind and the escaped atmospheric particles are $<$100 kg per second and $\sim$20 kg per second, respectively (Khurana et al., 2004). Electrons, sulfur, and oxygen ions are the primary types of magnetospheric particles. These particles originally escape from Io's atmosphere as neutrals, while Io orbits around Jupiter. Once ionized, these particles are carried away with the magnetic field and form a doughnut-shaped plasma cloud around Jupiter along Io's orbit, called Io's plasma torus. A schematic of Jupiter's magnetosphere is presented in Figure 1.3.

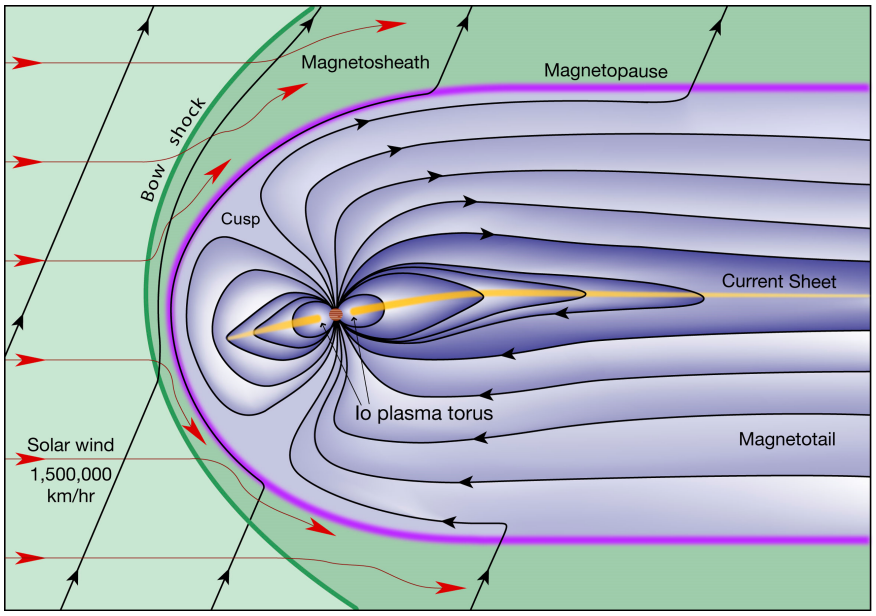

FIGURE 1.3: A schematic diagram of Jupiter's magnetosphere across the noon-midnight meridian seen from the dusk side. The dayside is located on the left in the direction toward the Sun and the nightside is on the right. Black solid lines present planetary and IMF magnetic field lines. The solar wind flows around the planetary magnetosphere in the direction shown by the red arrows. The purple contour stands for magnetopause. Region of solar wind plasma dominating is shaded in green and plasmas dominating by the internal source is shaded in lavender (Bagenal and Bartlett, 2013).

The interaction between the solar wind and a planetary magnetosphere may result in a magnetic reconnection process, on both dayside and nightside. Magnetic reconnection is the process of reconnecting two magnetic field lines from different regions. Dayside reconnection occurs when the IMF carried by the solar wind is antiparallel to the planetary magnetic field on the dayside magnetosphere (Dungey, 1961). This process can accelerate charged particles, allowing solar plasmas to flow into the magnetosphere and possibly resulting in auroral emissions. This is an important mechanism for Earth's auroral emissions. Whether

this process is important at Jupiter, in regard of Kelvin-Helmholtz instability in particular, is a debated issue (e.g., Kivelson and Southwood, 2003; Delamere and Bagenal, 2010; Desroche et al., 2012). The Kelvin-Helmholtz (K-H) instability is a flow shear-driven instability which can transfer plasma and momentum across the magnetopause boundary. It has been found at Earth's magnetopause during the quiet stage of the Dungey cycle.

The Dungey cycle is the process where plasma transportation is driven by solar wind interaction with the Earth's magnetosphere. This cycle starts from the dayside, where the open magnetic flux is formed by the dayside reconnection. The open magnetic field lines are then convected toward the nightside of the magnetosphere. Next, the open magnetic field lines sink toward the equatorial plane of the magnetotail and the nightside reconnection takes place again, where the open magnetic field lines become closed. The Dungey cycle, for example at the Earth's magnetosphere, is shown in Figure 1.4.

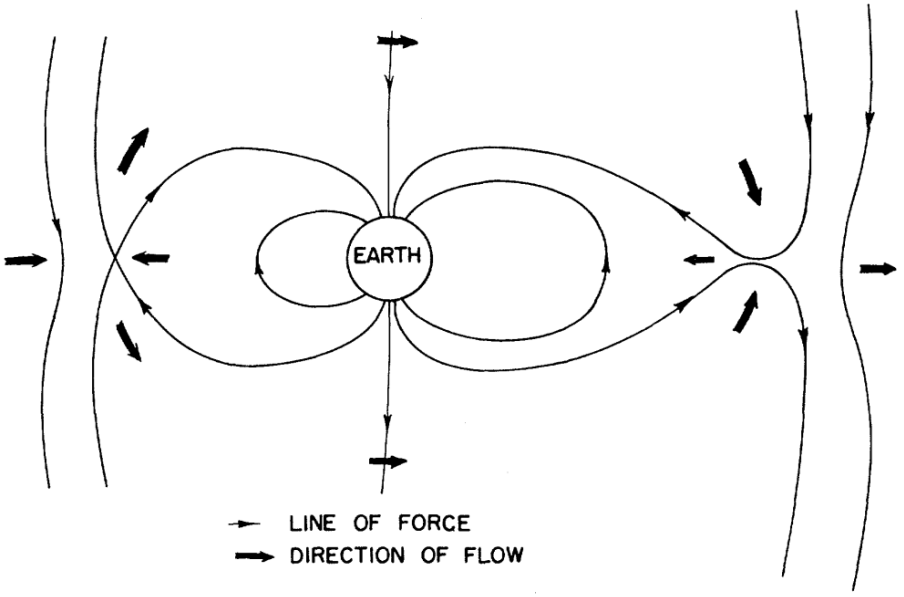

FIGURE 1.4: The side view of plasma flows in the Dungey cycle (Dungey, 1961).

However, the importance of the Dungey cycle on the plasma flow in Jupiter's magnetosphere is a debated issue (Delamere and Bagenal, 2013). The Vasyliunas cycle, which is a transport mechanism driven by internal processes, should dominate because this process is driven by the fast planetary rotation and the mass loading at Io. The plasmas inside the magnetosphere gain energy from the rotation and move outward from the planet, causing the centrifugal force to stretch the magnetic field lines down-tail. These stretched field lines create a thin current sheet on the equatorial plane. These closed magnetic field lines can then reconnect and release plasmoids in the tailward direction. The stages in this cycle are represented in Figure 1.5 (Vasyliunas, 1983).

1.3.2 Configuration and Dynamics of Jupiter's Magnetosphere

In order to better understand Jupiter's magnetosphere, it is typically divided into three regions: the inner, middle, and outer magnetospheres (Khurana et al., 2004).

The inner magnetosphere is a region within approximately 10 R_J from Jupiter. This area contains the orbits of Io and Europa, two of four Galilean moons. The mechanisms inside the inner magnetosphere are governed by the Jovian internal magnetic field. The main plasma source of Jupiter's magnetosphere, Io, and its plasma torus located at an approximate distance of $\sim 4 - 7$ R_J (Schneider and Trauger, 1995) are forced to corotate with the planet. The

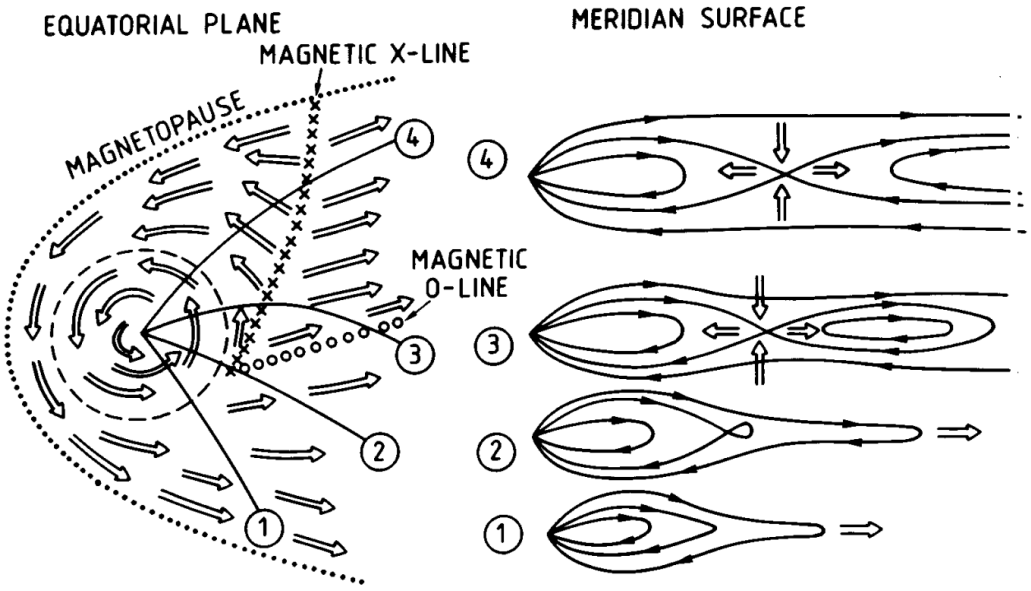

FIGURE 1.5: Plasma flows in the Vasyliunas cycle (left) on the equatorial plane. The side view illustrates (right) the plasma flows and the magnetic field lines along the meridian plane. The sequences are labeled by numbers (Vasyliunas, 1983).

plasma torus contains several million tons of plasmas, which diffuse outward away from the planet. The inner region is therefore relatively dense (42,300 amu/cm^3, Kivelson et al., 2004).

The middle magnetosphere is the region that ranges from 10 to 40 R_J. It is the region where the plasma stops rotating at the same angular velocity as the magnetic field because plasma is unable to conserve angular momentum as it flows outward. This phenomenon is called corotation breakdown. This process causes the azimuthal stretching of the magnetic field lines, while the radial stretching is the results of the balance between the centrifugal force and thermal pressure force on the plasma. As a result, the magnetic field lines lag behind the magnetic dipole systematically. This process leads the radial currents along the equatorial plane to flow, and connect with the ionospheric currents by field-aligned currents (FAC or Birkeland currents). The field-aligned currents are expected to form and accelerate electrons into the magnetosphere, which can lead to the formation of main auroral emissions. However, Bonfond, Yao, and Grodent, 2020 presented six observational results which contradict this concept which suggested that this theory might not be the main explanation for Jupiter's main emissions.

The region beyond 40 R_J is called the outer magnetosphere. However, its boundary is not fixed over time. On the dayside, the boundary of magnetopause varies between $\sim$60 and $\sim$90 R_J (Joy et al., 2002), depending on the strength of solar wind dynamic pressure. The magnetotail has a cylindrical shape with $\sim 300 - 400$ R_J in diameter. Its estimated length extends from at least 3,000 R_J, to distance more than 7,000 R_J beyond Saturn's orbit (Khurana et al., 2004).

1.3.3 Jupiter's Magnetic Field Model

For a better understanding of Jupiter's aurorae, the knowledge of magnetic field configuration should be as precise as possible. Generally, the model of Jupiter's magnetic field configuration is based on the magnetic field measurements by spacecraft flyby. The magnetic field

($\mathbf{B}$) can be represented by the sum of the internal field, $\mathbf{B_i}$, which can be derived from an internal potential field, V, and an external field, $\mathbf{B_e}$, which is associated to the magnetospheric currents in the middle and outer magnetospheres.

$$\mathbf{B} = \mathbf{B_i} + \mathbf{B_e} = -\nabla V + \mathbf{B_e}. \tag{1.29}$$

The potential field V can be expressed in terms of the spherical harmonics:

$$V = \sum_{l=1}^{\infty} \sum_{m=0}^{l} \left(\frac{R}{r}\right)^{l+1} P_l^m \left(cos\theta\right) \left[g_l^m cos(\phi) + h_l^m sin(\phi)\right], \tag{1.30}$$

where R is the planet's radius, r is the distance from the center of the planet, θ and ϕ are the colatitude and the longitude of the observer, P_l^m is the associated Legendre polynomial function, and g_l^m and h_l^m are Schmidt coefficients of order l degree m obtained by fitting to the observations.

For the external magnetic field $\mathbf{B_e}$, the field is partly generated by the current sheet in the middle magnetosphere. The current sheet model was first proposed by Connerney, 1981. This model accounted for the asymmetric of the magnetodisc magnetic field, which was fit well with the Voyager 1 and 2 and Pioneer 10 observations for the region within ~ 30 R_J very well. The Euler potential model of magnetodisc has been improved according to Galileo's observations (e.g., Khurana, 1997). The recent model presented by Connerney et al., 2020 focuses on currents in the inner to the middle magnetosphere. The best fit with Juno magnetic field observations is at the radial distance ranges from 7.1 to 51.4 R_J. This model provides a more accurate representation of the magnetic field in the inner and middle magnetosphere. Another source of the external field is the Chapman-Ferraro magnetopause current system, which is related to the outer magnetosphere.

The models of Jupiter's internal magnetic field have been developed, based on observations by many spacecrafts, i.e. Pioneer 10 and 11, Voyager 1 and 2, Ulysses, and Galileo, which obtained magnetic field data from their flybys or orbits near Jupiter (Khurana et al., 2004). Connerney et al., 1998 developed an internal magnetic field model of Jupiter called VIP4, which stands for Voyager, Io footprint, and Pioneer observations (VIP) and the maximum degree and order (4) of the fit. This model includes terms with Legendre polynomial coefficients up to order 4, using magnetic observations from two spacecrafts, Pioneer 11 and Voyager 1, combined with the location of Io footprints as constraints. However, later observations with better resolution revealed that footprint locations predicted by the VIP4 model do not match precisely with the observations, especially for footprints found near the kink region in the northern hemisphere. In addition, the VIP4 model does not precisely match the footprints of Europa and Ganymede.

Grodent et al., 2008 proposed the new magnetic field model called GAM, standing for the Grodent anomaly model, which was developed by adding the magnetic anomaly in the northern polar region to improve the prediction of the magnetic footprint's positions in the kink region. The model was able to fit the Io, Europa, and Ganymede footprints very well. However, this model is suitable only for the northern hemisphere.

Hess et al., 2011 proposed VIPAL magnetic field model which is based on the same in-situ Voyager and Pioneer magnetic field measurements as VIP4. This model covered the magnetic anomaly in the northern hemisphere and used longitudinal positions of Io's magnetic footprint as a constraint. This model is applicable to both hemispheres. Compared to VIP4 and GAM, VIPAL's prediction of the surface magnetic field strength is better in agreement with radio decametric observations.

The mapping model between Jupiter's ionospheric positions and their locations in the

magnetosphere was presented by Vogt et al., 2011. The model is based on flux equivalent calculation, in which the total magnetic flux passing through an area in the ionosphere is equal to the total flux through the mapped region in the magnetosphere. Accordingly, the effect of the internal magnetic field model on the flux equivalent calculation was investigated in Vogt et al., 2015. Several internal magnetic field models VIP4, GAM, and VIPAL were chosen for their analysis. These models were used to determine the locations of Ganymede's footprint in comparison with observed locations and were widely used to study positions of other auroral features, including the polar auroral features. However, by construction, the mapping model stops at magnetopause on the dayside and at 150 R_J on the nightside. Therefore, the mapping of a point in the ionosphere to a position corresponding to distance beyond 150 R_J in the magnetosphere is not possible with this model.

A new Jupiter magnetic field model was presented by Connerney et al., 2018, using magnetic field observations from Juno's instrument. The interim model, also known as the Juno Reference Model through Perijove 9 or JRM09, is derived from the first nine polar orbits of Juno. This model was presented since the first nine polar orbits provided the global coverage with an equatorial crossing in longitude of $\sim 45^\circ$ between perijove. The magnetic field was characterized by degree 10 spherical harmonic for the internal field combined with a simple magnetodisc model (Connerney, 1981) as an external field. This finding provided the first details on planetary dynamo processes occurring outside the Earth. The model also reveals Jupiter's magnetic field asymmetry in each hemisphere. The modified Vogt's magnetic flux mapping was updated to include JRM09 as an additional internal magnetic field model.

Recently, Juno's Prime Mission was completed. The 32 passes were done where PJ33 was operated on 15 April 2021 and the equatorial crossing is now $\sim 11^\circ$ separation in longitude. The JRM33 model is modeled with the spherical harmonic degree 18 (Connerney et al., 2022). This model provides the most detailed view of Jupiter's dynamo that we have ever had. The results suggested that Jupiter's magnetic field is generated by convective metallic hydrogen beneath 0.8 R_J and showed that Jupiter's magnetic field changed over time when compared to the JRM09 model.

1.4 Jupiter's UV Aurorae

For Earth's aurorae, the most dominant emission is from the collision between the auroral electron with atomic Oxygen at wavelength 557.7 nm, which is seen in green. However, atomic and molecular hydrogens make up the majority of Jupiter's upper atmosphere. Jupiter's aurorae can be seen in various wavelength ranges, i.e., UV, radio, infrared, visible, and X-ray (Grodent, 2015). This study focuses on the UV aurorae. An illustration of Jupiter's UV aurorae in the northern and southern hemispheres is shown in Figure 1.6. Jupiter's UV aurorae are complex and exhibit the most powerful auroral emissions in the solar system (the UV emitted power is in the order of 10^{12} Watts for Jupiter and 10^{10} Watts for Earth). The aurorae on Jupiter are extremely bright, approximately a hundred times brighter than those on Earth. In addition, Jupiter's magnetic field and Jupiter's magnetosphere are more complex than Earth's. Therefore, while Earth's aurorae are suggested to be strongly associated with the solar wind, the relation between Jupiter's aurorae and the solar wind seems to have some correspondence, but the timing does not exactly match, e.g., Clarke et al., 2009; Nichols et al., 2017b; Nichols et al., 2009b; Kita et al., 2019. Generally, Jupiter's aurora is divided into four regions categorized by the auroral behaviors and their relation to the specific originating processes, which are the main emissions, the equatorward emissions, the satellites' footprints, and the polar auroral emissions.

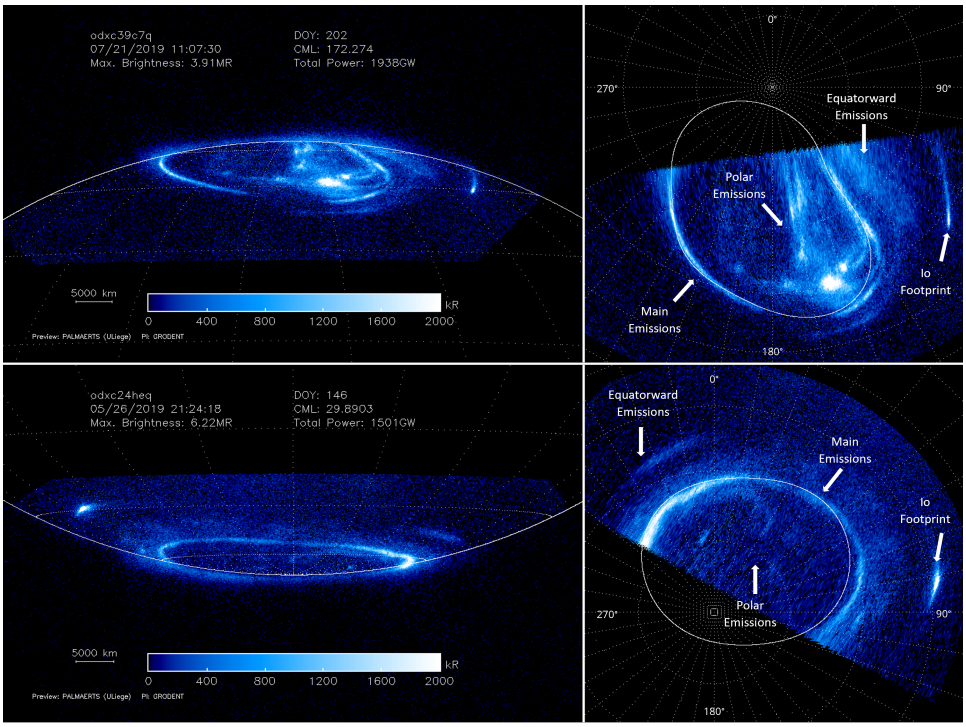

FIGURE 1.6: HST/STIS FUV images of (Top) Jupiter's northern aurora and (Bottom) Jupiter's southern aurora taken in 2019 during HST GO-15638 campaign. Figures on the right column present the polar projections of four main regions, which are the main emissions (indicated by white contour), the polar emissions, the equatorward emissions, and the satellite footprints (Denis GRODENT (NASA/ESA/Université de Liège)).

1.4.1 Auroral Morphology

The main auroral emissions are the brightest and most stable features. Its emitted power represents approximately one-third of the total emitted UV auroral power. The main aurora appears as a discontinuous contour centered at the magnetic poles. The shape of the main emission in the northern hemisphere is distorted due to the magnetic anomaly in a kink region (Grodent et al., 2008). The main auroral emissions are suggested to be mapped from the location in the ionosphere to the middle magnetosphere approximately at a distance of 20-60 R_J (Clarke et al., 2004; Vogt et al., 2011). Hence, Jupiter's main emissions are suggested to be driven mainly by the internal processes. According to Cowley and Bunce, 2001; Hill, 2001; Southwood and Kivelson, 2001, the magnetosphere-ionosphere coupling current system related with the corotation breakdown was suggested to be associated with Jupiter's main emissions. The current loop is closed by the field-aligned currents, which flow upward from the ionosphere to the magnetosphere in the low latitude, then return to the ionosphere (downward current) in the higher latitude in the ionosphere and connected to the upward field-aligned current via Pedersen current in the ionosphere. Through upward field-aligned currents, the precipitating electrons are transported to Jupiter's ionosphere where they cause the auroral emissions. The cross-section of the jovian magnetosphere showing the coupling current system is illustrated in Figure 1.7. However, the magnetic perturbations which are signatures of Birkeland currents were found to be weak in relation to the associated auroral intensity (Kotsiaros et al., 2019; Connerney et al., 2017a).

The second component is satellite magnetic footprints, which are fixed along magnetic flux tubes connected to three of Jupiter's Galilean moons (Clarke et al., 2002), i.e. Io, Europa, and Ganymede. The Io UV footprint brightness is in the order of a few tens of GW (Bonfond et al., 2013a), while the UV brightness from Ganymede and Europa footprints are in the

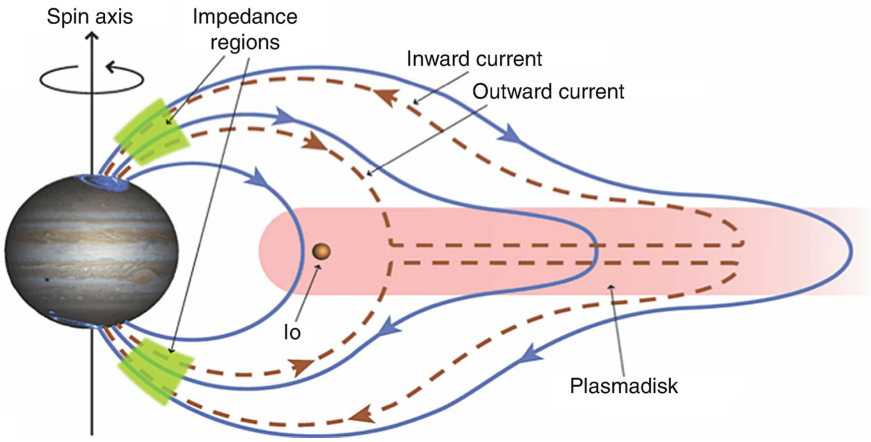

FIGURE 1.7: Schematic diagram of a cross section of Jupiter's magnetosphere showing the coupling current system through Jupiter's inner and middle magnetosphere (Bagenal, 2013). The blue solid lines represent the planetary magnetic field lines, stretching along the plasma sheet. The red dashed lines present a magnetosphere-ionosphere coupling current system where radial currents are in the plasmadisk and FAC presented by inward and outward currents.

order of a few GW (Bonfond et al., 2008; Bonfond et al., 2013b). The correlation in the evolution of UV footprints brightness with the satellite location in the magnetosphere is presented (Wannawichian, Clarke, and Nichols, 2010; Serio and Clarke, 2008). Tentative detection of the Callisto footprint has also been recently reported (Bhattacharyya et al., 2018). The positions of the satellites' footprints in Jupiter's ionosphere depend on the positions of the moon in the orbits. The orbital distances of these satellites are located inside Jupiter's magnetosphere. As a result, the satellites' magnetic footprints are useful constraints for mapping the internal magnetic field model (i.e., Vogt et al., 2011).

The third component is equatorward emission, which appears in the region between the main emissions and Io's footprint path. These equatorward diffuse emissions are unrelated to the satellite footprints (Radioti et al., 2009). In addition, more compact feature associated with plasma injections in the middle and inner magnetosphere (Dumont et al., 2014; Mauk et al., 2002) and a secondary oval (Gray et al., 2017) is also found in this region.

The last component is the polar emissions, which are the main topic of this study. Polar emissions are the entire emissions in the region poleward of the main emissions. The brightness of polar aurorae rapidly varies in various observed time scales, and they consist of several emission features. In addition, the polar aurorae are mapping to farther distances in the magnetosphere. Therefore, the polar aurorae are often suggested to link with the outer magnetosphere, leading to the possibility of the relation between polar aurorae and the current system related to the Dungey and/or Vasyliunas cycle (Cowley et al., 2003; Grodent et al., 2003a). However, details on the mechanisms are still debated. Based on the HST observations, polar emissions in the northern hemisphere are divided, based on the average brightness and the behavior variations, into three subregions which are the dark region, the swirl region, and the active region (Grodent et al., 2003b), as shown in Figure 1.8.

The dark region, indicated by the yellow contour in Figure 1.8, is characterized by a crescent shape located above the main emissions in the dawn sector (6:00 magnetic local time). The UV emission in the dark region is not bright in comparison to the other two subregions. Its upper limit of brightness is $\sim$ 10 kilo-raleigh (kR) (Grodent, 2015), where 1 kR = 10^9 photon cm^{-2} s^{-1} into 4π steradians (Clarke et al., 2002). The swirl region (red contour), located around the magnetic pole, consists of numerous features such as the patchy and transient features whose brightness highly varies, ranging from a few kR to a hundred kR. In addition, the swirl region appears to have a high color ratio (see the detail of color ratio in

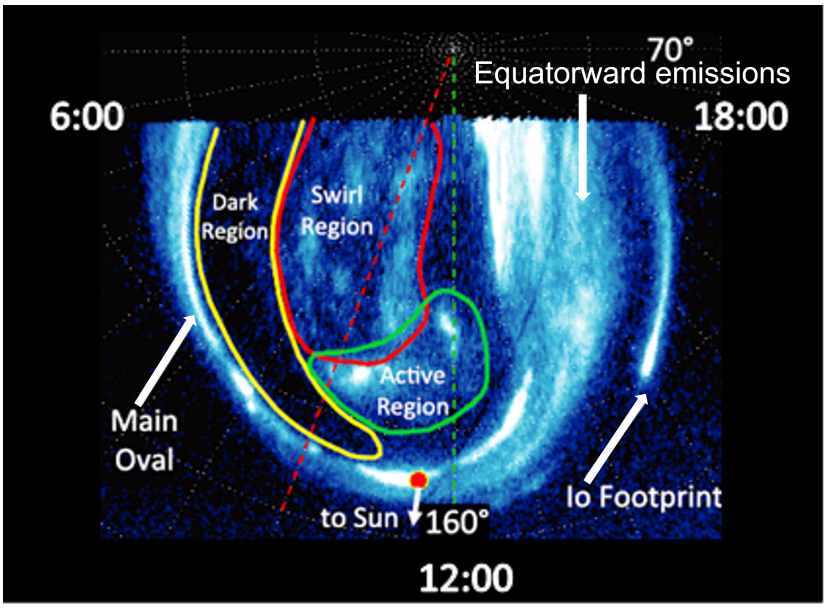

FIGURE 1.8: Polar projection of Jupiter's aurora in the northern hemisphere modified from Grodent et al., 2003b showing four components of Jupiter's aurora. Each color contour (red, green, and yellow) represents the subregion in the polar auroral region. The white arrow below the red point indicates the sun's direction which is related to noon magnetic local time (Vogt et al., 2011).

the next section) even though the brightness is not much compared to the main emissions (Bonfond et al., 2017). The high color ratio suggests that the high-energy particles penetrate deeper in the atmosphere and experience hydrocarbon absorption by methane. The active region usually lies above the main emission in the noon to post-noon sector (Pallier and Prangé, 2001). The clear observable features are the polar flares, the arc-like feature, and the auroral bright spots. The brightness of the polar flares sometimes increases from kR to MR in a short timescale (Waite et al., 2001). Bonfond et al., 2011 revealed that these flares were brightened with the emitted power up to $\sim 10 - 40$ GW. The flares also reappeared with a time scale of $2 - 3$ minutes. In comparison with a similar feature of Earth's aurora, Bonfond et al., 2011 suggested that this feature could be related to the pulse reconnection on the front of the magnetopause. However, Bonfond et al., 2016 further studied the dynamics of quasi-periodic (QP) flares for both northern and southern hemispheres with a longer series of observations. They found that these flares can brighten in phases between hemispheres. Therefore, even though they are mapped to several R_J in the dayside magnetosphere, the processes for causing QP flares are taking place on closed field lines and involve the ionosphere or the acceleration region.

Another auroral feature that is observable in the active region is the polar auroral bright spot, a feature that will be the focus of this study. The bright spot is very bright in UV emission and usually appears as a compact shape. Pallier and Prangé, 2001 studied high latitude aurorae and found that the positions of bright spots in Jupiter's ionosphere are not fixed in SIII longitude, position but continue to be located near noon magnetic local time as Jupiter rotates. Based on its location, Pallier and Prangé, 2001 suggested that the bright spot is probably a signature of Jupiter's polar cusp. However, a clear explanation for the cusp process is still debated. In addition, even though this feature could provide more information of Jupiter's polar cusp which will be helpful for understanding Jupiter's auroral processes, there is no research that particularly studies the characteristics of the bright spot in more detail. One reason for the lack of study for this feature might be due to the limited observation times and a limited view seen from Earth by the HST. Instead, the Juno spacecraft provides

an opportunity to explore this feature in very close proximity. The Juno observation times in each hemisphere are also longer than those observed by HST. Therefore, the study of polar auroral bright spot emission by Juno observation is chosen to be analyzed in this thesis.

1.4.2 The Color Ratio

The auroral brightness can be determined from the number of photon counts detected by the detectors. The raw counts are converted to the auroral brightness and also to the emitted power. Gustin et al., 2012 presented the conversion factors from instrument counts to the brightness in kR and the auroral power emission in mW/m^2, which directly varies with the color ratio. Jupiter's auroral emission in Far Ultraviolet (FUV) is typically dominated by H Lyman-alpha (H Ly-α), and the Lyman and Werner bands of H_2 (Gustin et al., 2012). For Jupiter, there is a hydrocarbon layer, dominated by methane (CH_4), that can interact and attenuate auroral emissions. Figure 1.9 shows an example of an extract spectrum obtained from the observations. The dashed plot represents the synthetic unabsorbed H_2 spectrum for comparison.

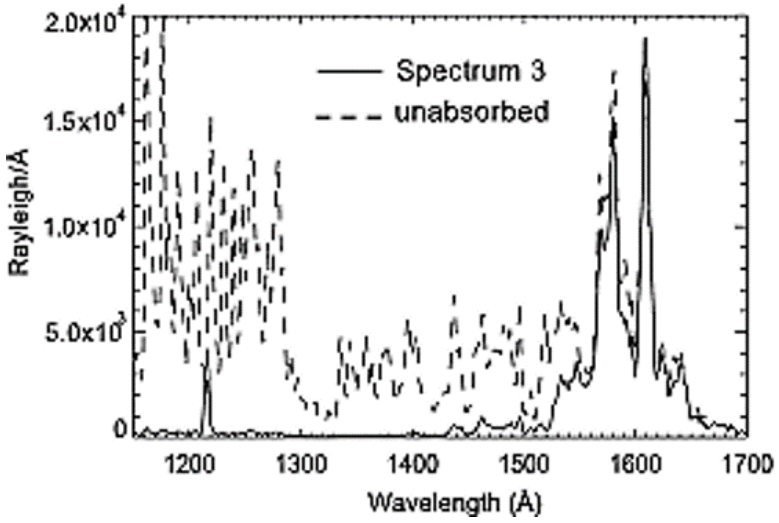

FIGURE 1.9: Extracted spectra obtained from the HST time-tag observation. For comparison, a synthetic unabsorbed H_2 spectrum is overplotted by a dashed line to see the effect of methane absorption (Gustin et al., 2006).

The absorption of auroral emission in wavelength shorter than 1350 Å due to the hydrocarbon layer is related to the precipitation depth of Jupiter's auroral particles. The absorption can be indicated by the color ratio which is defined by the ratio between emission intensity of H_2 at wavelengths with no absorption (1550-1620 Å) and the emission intensity at the wavelength in which the absorption takes place (1230-1300 Å);

$$CR = \frac{\int_{1550}^{1620} I(\lambda)\,\mathrm{d}\lambda}{\int_{1230}^{1300} I(\lambda)\,\mathrm{d}\lambda}. \tag{1.31}$$

The spectral intensity $I(\lambda)$ along the line of sight is determined by $I(\lambda) = \int P_\lambda(z) e^{-\tau_\lambda}\,\mathrm{d}s$, where $P_\lambda(z)$ is the production rate of Lyman and Werner band emission at wavelength λ and altitude z. The parameter τ_λ is an optical depth at altitude z due to photoabsorption of methane, defined by $\tau_\lambda(z) = \sigma_\lambda(CH_4) \int n_{CH_4}\,\mathrm{d}s$, where $\sigma_\lambda(CH_4)$ is the methane absorption cross section at wavelength λ, n_{CH_4} is local number density of methane, and ds is distance along the line of sight (Gérard et al., 2014).

Hence, the color ratio is based on the absorption cross section of methane, and it depends on the altitude of auroral emission relative to the hydrocarbon layer, which depends on the hydrocarbon homopause altitude. The eddy diffusion coefficient plays a role in controlling the hydrocarbon mixing in the homosphere, and affecting hydrocarbon absorption of auroral emission for a given energy of a particle. Therefore, the color ratio can be used to characterize energy of the precipitating particles since particles with higher energy can penetrate deeper into the atmosphere and be more affected by the methane absorption at shorter wavelengths. Based on Gustin et al., 2012's analysis, 10 kR of total unabsorbed FUV H_2 emissions in Lyman and Werner bands are produced by an precipitating electron energy flux of 1 mW/m^2. Note that this conversion factor is specific for a given range of 70-140 keV. The mean energy outside this range should be reconsidered (Gustin et al., 2016).

1.4.3 Previous Observations of Jupiter's Polar Aurorae

Jupiter's aurorae have been mainly studied by using Advanced Camera for Surveys (ACS) and Space Telescope Imaging Spectrograph (STIS) onboard the Hubble Space Telescope or HST. Different components are studied for different purposes. This section reviews some studies of Jupiter's polar aurorae devided into two categories; the study of bright spot emissions which is the core of this thesis, and the study of polar aurorae made by instruments onboard Juno.

Pallier and Prangé, 2001 presented the appearances of polar auroral bright spots as part of their high latitude aurora study. They presented that the bright spot position is not fixed at any System III longitude. The bright spot instead corresponded to near noon magnetic local time. This feature was therefore suggested to be a signature of the northern polar cusp and possibly driven by solar wind dynamics. However, the polar flares, another feature in the active region, are more studied (e.g., Waite et al., 2001; Grodent et al., 2003b; Cowley et al., 2003; Bunce, Cowley, and Yeoman, 2004). Waite et al., 2001 showed that the brightness of polar flares can increase from kR to MR in a short timescale. Bonfond et al., 2011 showed that the appearance of these flares could repeat regularly along the HST 45 minutes sequences with a time scale of $2-3$ minutes. The dynamics of QP flares for both northern and southern hemispheres with a longer series of observations studied by Bonfond et al., 2016 showed that the flares' variations of both hemispheres have a similar sinusoidal trend with a period of 140 seconds, suggesting some connection between both hemispheres. The QP flares are approximately mapped to the dayside outer magnetosphere. Bonfond et al., 2016 concluded that the QP flares rather favor processes related to the closed magnetic field lines that can cause the QP flare to occur in phases between hemispheres. In addition, they showed that the polar flares appeared in a large size, the area sizes of QP flares range from one-tenth to the whole active region. This size is large in contrast with the compact shape of the bright spot emission. This characteristic is the one category to distinguish the polar flares and bright spot emissions.

With the recent observations made by the instruments onboard Juno spacecraft, the longer observation time, the spatial resolution, and the spectral resolution observations will provide useful results which will help us to better understand Jupiter's aurorae. The complete view including the nightside of Jupiter's aurora taken by Juno-UVS (ultraviolet spectrograph) during its first perijove was presented in Bonfond et al., 2017. Many features are interesting. For example, the large intense outer emissions were clearly seen in both hemispheres. The results showed the development of the outer emissions from a specific region to spread around the pole, followed by the large nightside protrusion, suggesting large-scale radial plasma transport. For the active region, a bright arc parallel to the main emission was found in the noon-to-dusk sector. The auroral filaments, thin filament long-lived features that are usually observed to be aligned along noon-midnight meridian across active-swirl

region (Nichols et al., 2009a), and flares were also found. In addition, the swirl region was clearly identified by the region of high color ratio. Greathouse et al., 2021 recently studied the polar aurorae and defined two distinct regions; the swirl region, which is indicated by a high color ratio area, and the polar collar, whose color ratio is lower. They presented the interesting results that the brightness in the polar collar varies correlating with magnetospheric local time, while the swirl region is related to the ionospheric local time instead. In addition, Hue et al., 2021 presented the Juno-UVS study of the expanding auroral emissions found in the swirl region with the typical brightness of 140 kR. The emission can expand into a circular shape with a radius of $\sim 1,000$ km. Hue et al., 2021 concluded that this feature is possibly caused by either the dayside reconnection or the Kelvin-Helmholtz instabilities.

Not only the new knowledge related to aurorae are revealed by UVS, but also observed particles, waves, and magnetic field data from other instruments onboard Juno provide much more in-depth information about Jupiter's aurora. Jupiter's magnetosphere and aurorae observed by instruments on board Juno during the first polar orbit was presented by Connerney et al., 2017a. The comparison between auroral intensity observed by Juno-UVS and the particle measurements are studied. The results from Gérard et al., 2019 showed that the main emissions brightness and the brightness computed from the observed electron flux are correlated. The characteristics of energetic particles in the polar region were presented. The most common results are the dominating of upward particle flux in the polar region, i.e., Mauk et al., 2017a; Ebert et al., 2019; Mauk et al., 2020; Allegrini et al., 2017. Mauk et al., 2017a presented that not only the upward flux is dominated, but the downward flux is also insufficient to produce the UV aurorae. Paranicas et al., 2018 showed that intense upward electron beams at energy > 1 MeV are found to be connected with the swirl region. The relation between waves and particles related to Jupiter's main emissions and polar aurorae were revealed by Kurth et al., 2018, Elliott et al., 2018b, and Elliott et al., 2018a. Elliott et al., 2018b suggested that broadband whistler mode waves can accelerate upward electrons to high energies, while Elliott et al., 2020 presented the hypothesis of waves-particles interaction in the Jovian polar cap, in which the upward-propagating Whistler-mode waves are produced by the upward electron beams as well. These studies provided crucial information allowing the community to gain more understanding of the dynamics in the polar region, leading to the suggestion of possible processes related to Jupiter's auroral emissions. However, the polar auroral processes, including the mechanism related to the bright spot emissions are still under investigation. Even though more observations were required to confirm the processes responsible for these features. While Juno observations allow us to study the entire aurora, including the night-side, its unique suite of instruments will allow us to broaden our understanding of the Jovian aurorae.

Chapter 2

Data and Instruments

Five instruments onboard Juno spacecraft are the main tools, used to provide the data for this study. The prime mission of Juno covers 35 science orbits, labeled by perijove (PJ) and number of orbits, as PJ1-PJ35, from 5.07 years of the spacecraft's mission. Each perijove crosses Jupiter at a specific longitude, allowing the complete view of the entire planet for scientific investigation purposes. Originally, it was planned to reduce the orbital period from 53 day to 14 day by firing the spacecraft's main engine. This operation is called period reduction maneuver (PRM) and was scheduled on October 19, 2016, during PJ2. However, the propulsion system showed signs of problems and the PRM was canceled. It was decided that the orbital period would remain 53 days for the rest of the prime mission. Moreover, due to the spacecraft entering in safe mode before PJ2, no scientific data was acquired during PJ2.

Juno possesses three rigid solar panels with a separation angle of 120°. Juno is spin-stabilized and rotates $\sim$ twice per minute ($\sim$ 30 s period). The z-axis of the spacecraft coordinate system is along the rotation axis centered at the central body, where the x-axis is in the direction of the solar panel which includes the MAG boom at the end. The y-axis is therefore in a direction according to a right-hand orthogonal system. Juno carries nine scientific instruments which observe Jupiter in various ways, pursuing several specific objectives. The gravity field is observed by the gravity science instrument (GRAV) (Asmar et al., 2017) for providing new constraints on the interior structure model. The measurements of Jupiter's magnetic field are observed by the Juno Magnetometer (MAG) (Connerney et al., 2017b). MAG's observation allows us to study both internal magnetic field and external contributions in the more distant magnetosphere (current sheets and various current systems), as well as Alfvén waves. The atmospheric environment is explored by the MicroWave Radiometer (MWR) experiment (Janssen et al., 2017). Juno color, visible-light Camera (JunoCam) is used to take color (in visible) images of Jupiter's atmosphere (Hansen et al., 2017). Jupiter's aurorae are studied in two wavelength ranges by the UltraViolet Spectrometer (UVS) (Gladstone et al., 2017) and Jupiter InfraRed Auroral Mapping instrument (JIRAM) (Adriani et al., 2017). Magnetospheric particles are observed by the Jupiter Energetic particle Detector Instrument (JEDI) (Mauk et al., 2017b) and the Jovian Auroral Distributions Experiment (JADE) (McComas et al., 2017). The radio and plasma Wave instrument (Waves) is designed to measure radio and plasma waves associated with the auroral emissions. The illustration of Juno spacecraft and its payloads are shown in Figure 2.1.

The observations in high latitude, in the polar region, can reveal very important information for unresolved questions related to Jupiter's aurorae. This thesis studies the bright spot emissions, based on the data observed by the instruments onboard Juno. The primary study of the bright spot morphology discussed in Chapter 3, focuses on the auroral images taken by the UVS instrument. The auroral bright spot's intensity, positions, and temporal variations are determined. The UVS observations enable the study of this feature even during the night time, which cannot be observed by the HST. To understand the mechanisms and the

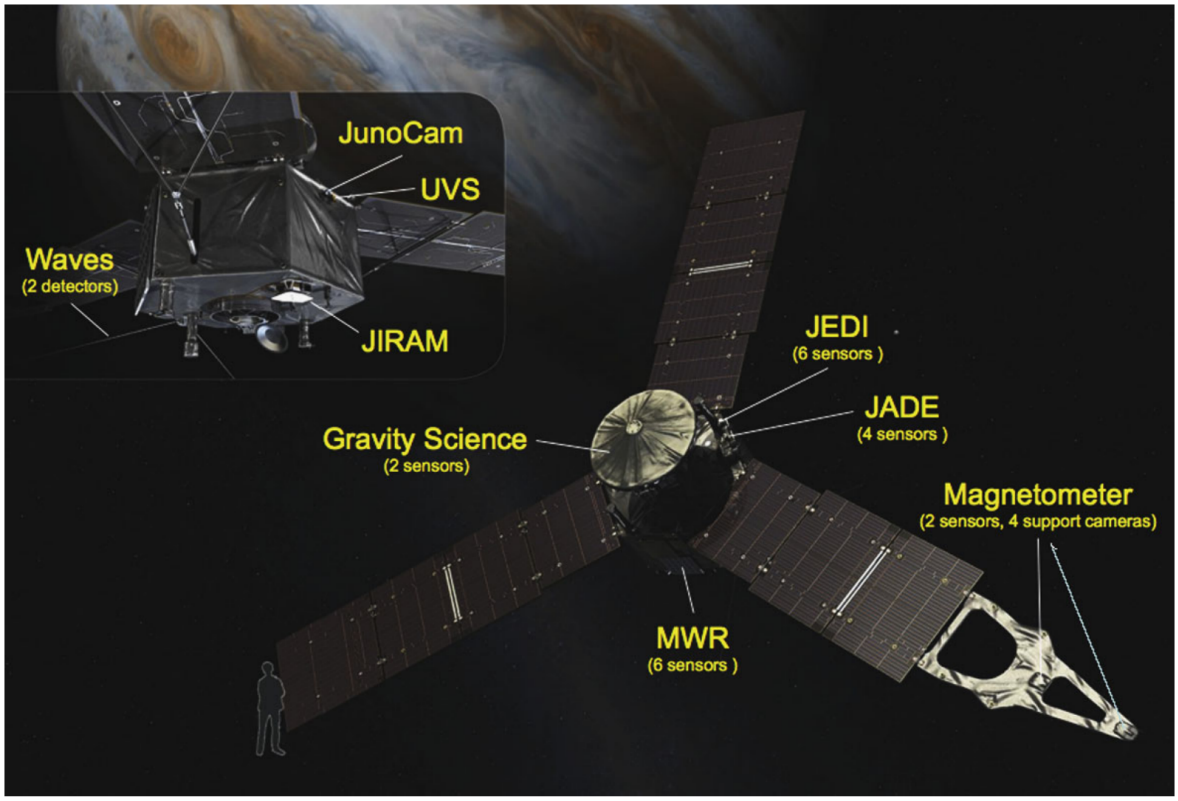

FIGURE 2.1: Juno spacecraft and its onboard instruments (Bolton et al., 2017). Three arrays containing 11 solar panels are 120° apart.

processes related to the bright spot emissions, the observed characteristics of particles, field-aligned currents, and plasma waves are needed. These data can be obtained by the in-situ measurements, i.e. JEDI, JADE, Waves, and MAG. The comparison between the observed data from these in-situ measurements and the bright spot characteristics is done when the spacecraft flew above the bright spot position, at which the spacecraft and the emission are linked by the same magnetic field line. Such events are only occasionally found, since the bright spot is not a stable feature contrary to the main emission or the satellite footprints. Three particular events are studied and presented in the study presented in Chapter 4. This chapter provides details on the data from five instruments used in this work, which are UVS, JEDI, JADE, Waves, and MAG instruments.

2.1 Juno Ultraviolet Spectrograph

Juno-UVS is an ultraviolet photon-counting imaging spectrograph. It operates in the UV wavelength range from 68 to 210 nm. At the entrance, a flat scan mirror targets an object with angle $\pm 30^\circ$ perpendicular to the Juno spin plane. The slit is formed by three contiguous segments with field of view (FOV) of $0.2^\circ \times 2.5^\circ$, $0.025^\circ \times 2^\circ$, and $0.2^\circ \times 2.5^\circ$. This shape is called a "dog-bone" shape. The output of UVS observation is a record of photon detections. The X position corresponds to the spectral dimension of the photon count and Y position corresponds to spatial dimension along the slit (Gladstone et al., 2017; Greathouse et al., 2013; Hue et al., 2018). Every $\sim$30 seconds (the Juno spin period), the UV image is taken at the position that the UVS' view points at the planet. During each swath, a point source is observed for $\sim$ 17 ms and $\sim$ 2 ms in the wide and narrow slits, respectively. During the slit scanning through the planet, each photon event is recorded as a time-tag list with a unique

location, wavelength, and time. Figure 2.2 shows the spectral image that was generated from the photon list from data. The pixel array is 2048×256 (spectral × spatial). The active pixels, which can see photon counts, cover the required 68-210 nm wavelength range. Two bright stripes correspond to photon counts coming from the wide slits. The background count rate due to electrons was subtracted from the raw image to clean the unrelated photon counts before the scientific interpretation. The cylindrical map covers 360° longitude and $-90°$ to $+90°$ latitude is created by applying photon count to a pixel corresponding to its latitude and longitude. The mask array containing the coordinates and times of masks applied to the detector during observations is applied to a cylindrical map to identify the region of interest. That is the intensity region of a wide slit. Finally, the polar UV image on the polar coordinates is created. Various regions of Jupiter's aurora can be observed, depending on the direction of the pointing mirror in each spin. The area covered by the instrument can vary depending on the altitude of the spacecraft.

In this study, the polar projections (i.e., Figure 2.3a) are constructed under the assumption that the aurorae take place at an altitude of 400 km above one bar level (Bonfond et al., 2015). The conversion from counts to kR depends on the effective area. The effective area was calibrated during the flight through the stellar calibration by dividing the integrated flux of O, A, and B stars observed by Juno-UVS with the calibrated spectra observed by the International Ultraviolet Explorer and the Hubble Space Telescope (Hue et al., 2018; Greathouse et al., 2013). The brightness in kR presented in this study corresponds to the total brightness in the unabsorbed H_2 Lyman emissions and Werner bands. This can be calculated by multiplying the intensity within the wavelength between 155-162 nm (a spectral domain with no hydrocarbon absorption) with a constant of 8.1, a conversion factor based on the H_2 synthetic spectrum calculated by Gustin et al., 2013. From figure 2.3a, the black color presents the polar regions seen in UVS view, but there is no photon detection. The data along the slit are sometimes blank due to the buffer saturation or high radiation levels leading to not nominal voltage, resulting in an unreliable calibration.

Since UVS takes images of Jupiter's aurora in a specific region in each spin, the images from several consecutive spins are combined (combined image from two spins is shown in Figure 2.3b) and then a completed view of the aurora can be built as shown in Figure 2.3c. Typically, the entire auroral regions are covered by $\sim$ 40 spins (20 minutes) observed at the distance of $\sim 1.6\,R_J$ (Hue et al., 2021). To give the most weight to the brightness from the last spin, the intensity count of the previous spin is taken only a half, accordingly, the second to previous spin is taken only a quarter of its intensity count, and so on. Thus, nth spin before the last spin is divided by 2^n. The uncertainty of brightness analysis due to the in-flight calibration of the instrument effective area is discussed in Hue et al., 2018.

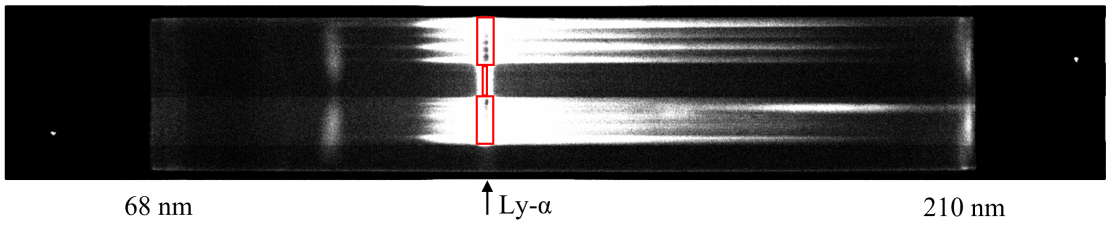

FIGURE 2.2: Spectral image of the photon count over the 2048 × 256 pixels size observed by Juno-UVS. The intensity covers the wavelength range of 68-210 nm in the $\sim$ 1500 active pixels in the x axis (and $\sim$ 230 active pixels in the y axis). The dog-bone shape appears (overplotted for clarity by red boxes, not to scale) at 121-nm Ly$-\alpha$ spectral line. Two bright pixels appearing at the lower left and upper right at the image edges correspond to two stimulation pixels (stims) for checking the effect of temperature on the wavelength scale.

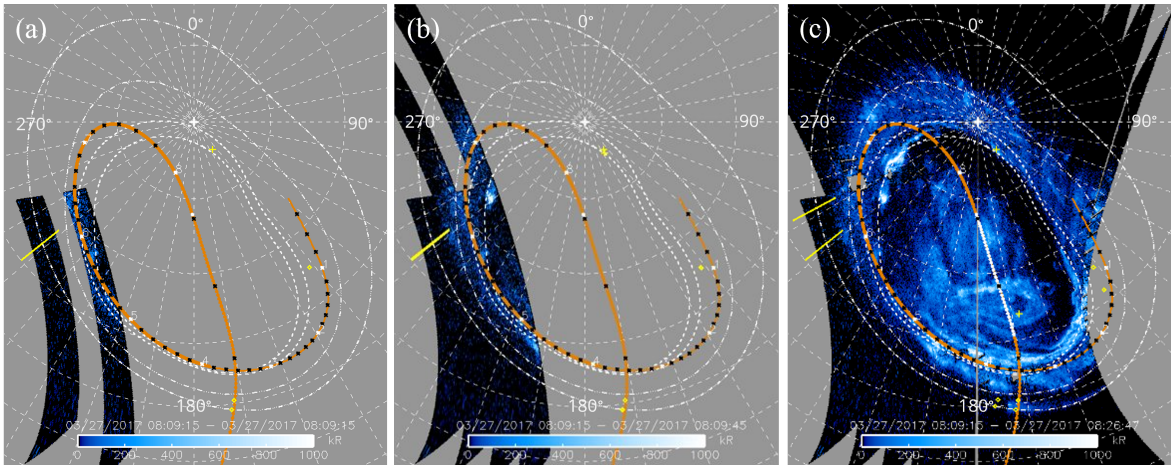

FIGURE 2.3: Polar projection of Jupiter's northern aurora. (a) Image from one spin taken on 27 March 2017, 08:09:15 UT, (b) Combined image from two spins taken on 27 March 2017, 08:09:15 UT and 08:09:15 UT, and (c) complete view of Jupiter's northern aurora made by integration of data acquired between 08:09:15 UT and 08:26:47 UT. The grid represents meridians and parallels in the SIII, spaced every ten degrees. Two short yellow lines indicate the subsolar longitudes of the start and stop timings of the combined data. The innermost dashed contours show the compress (inner) and expand (outer) cases of the statistical position of main emissions (Bonfond et al., 2012). All other polar projection images in this thesis will display the grid and main emission contours. The Ganymede footprint path and the Io footprint path (outermost contour) are the two outer contours, respectively.

2.2 Particle instruments

Jupiter Energetic-particle Detector Instrument or JEDI is a particle detector measuring energetic particles. The instrument can measure the energy and distributions of electrons in the energy range from $\sim$ 25 to $\sim$ 1,200 keV by using a solid-state detector (SSD). JEDI uses Time-of-Flight by Energy (TOF) and Time-of-Flight by Microchannel Pulse Height (TOF$\times$PH) techniques to measure energy, direction, and compositional distributions of ions in the range of $\sim$ 10 to $>$ 1.5 MeV for protons and $\sim$ 150 to $>$ 100 MeV for oxygen and sulfur. The instrument consists of three nearly-identical sensors (JEDI-90, JEDI-180, and JEDI-270), which cover different pitch angle ranges. The JEDI-90 and JEDI-270 are oriented to cover $\sim$ 360° within the plane perpendicular to the spacecraft spin axis, while JEDI-180 is oriented parallel to the Juno spin axis to cover a view along the spin axis. Figure 2.4 shows the viewing configuration of three JEDI sensors with respect to the spacecraft. More information about the instrument can be found in Mauk et al., 2017b and the specifications on caveats related to JEDI can be found in the supplementary materials of Mauk et al., 2018.

Another particle detector is the Jupiter Auroral Distributions Experiment or JADE. JADE is made up of two subsystems; three identical electron sensors (JADE-E, one of which is currently inactive) and an ion composition sensor (JADE-I). The placement of JADE sensors is illustrated in Figure 2.5. For electrons, JADE-E measures the pitch angle distribution in the energy range of $0.1 - 100$ keV with a 120° field of view for each sensor and all three sensors are placed to cover 360° (240° for functioning sensors) in the azimuthal direction perpendicular to the spin axis. For ions, JADE-I measures in the energy range from 10eV/q to 46 keV/q, where q is electric charge, with a field of view of 270° $\times$ 90° in a spin period (McComas et al., 2017).

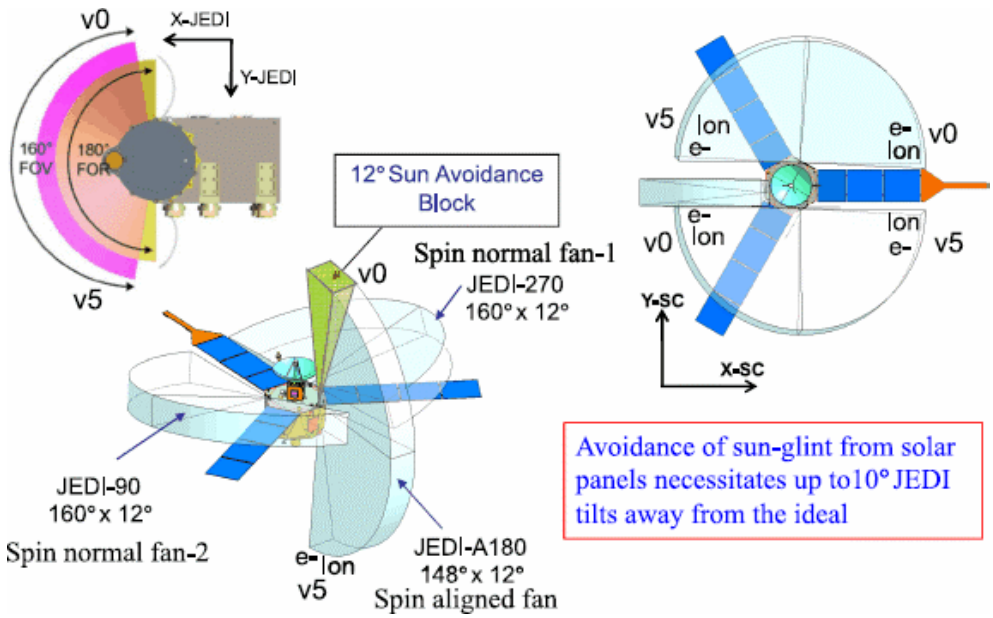

FIGURE 2.4: Configuration and viewing of JEDI sensors with respect to spacecraft(Mauk et al., 2017b). The upper left image shows the JEDI coordinate system (X-JEDI and Y-JEDI), while the spacecraft coordinate system (X-SC and Y-SC) is represented in the middle right.

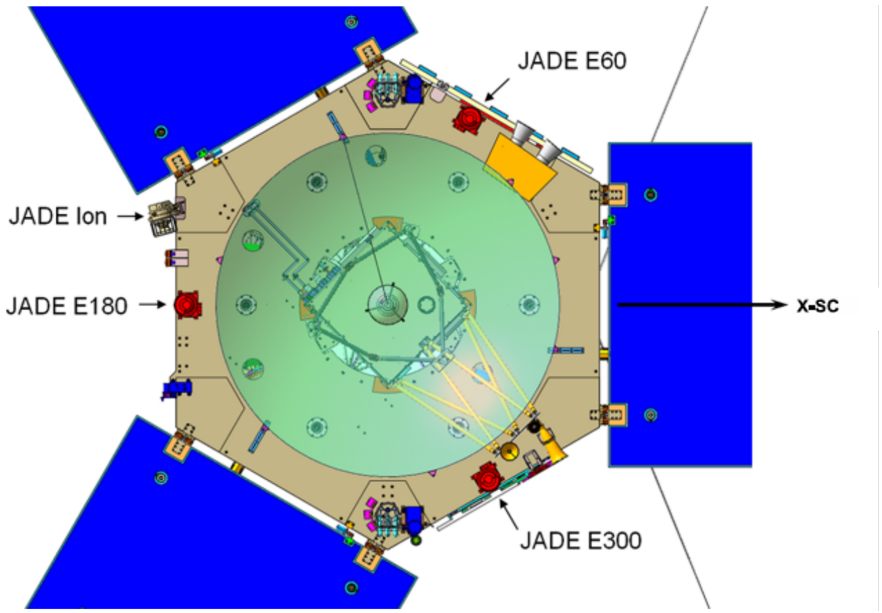

FIGURE 2.5: Configuration and field of view of JADE-I and three JADE-E sensors on the spacecraft (McComas et al., 2017). All JADE-Es sensors (JADE E60, JADE E180, and JADE E300) are placed at angles equally far apart to observe full angle coverage simultaneously.

2.3 Waves Instrument

The Juno's Waves instrument measures radio and plasma waves to study the interactions between Jupiter's magnetic field, Jupiter's magnetosphere, and the atmosphere. The instrument comprises a single dipole antenna for the electric field measurements in the 50 Hz to 41 MHz frequency range, and a magnetic search coil for the magnetic field component observations in the 50 Hz to 20 kHz frequency range. The electric antenna has a "V" configuration with a total effective tip-to-tip length of $\sim$4.8 meters and is oriented perpendicular to the spacecraft spin axis (z-axis) and the x-axis. The search coil is a short (15 cm) core, with a sensitive axis parallel to the spin axis of the spacecraft. More detailed explanations of the instrument can be found in Kurth et al., 2017. The data obtained here is a once-per-second sample rate. The data from the Waves instrument presented in this thesis are the frequency-time spectrograms of the electric and magnetic field spectra.

2.4 The Magnetic Field Investigation

The Juno magnetometer (MAG) is designed for magnetic field vector measurement. The instrument consists of two identical magnetometer sensor suites located at 10 m (inbound) and 12 m (outbound) from the center of the spacecraft (see in Figure 2.1). The Fluxgate Magnetometer (FGM) is used to detect magnetic field vectors, while Advanced Stellar Compass (ASC) CCD imagers are used to determine sensor's attitude. The vector field is sampled at 64, 32, or 16 measurements per second, depending on the distance between Jupiter and the spacecraft. The observations are made over the 6 available ranges, covering magnetic field strength from $\sim$ 1 nT to $\sim 16 \times 10^5$ nT: range 0 ($\pm$1,600 nT per axis), range 1 ($\pm$6,400 nT per axis), range 2 ($\pm$ 25,600 per axis), range 4 ($\pm$102,400 nT per axis),range 5 ($\pm$409,600 nT per axis), and range 6 ($\pm$1,638,400 nT per axis). More details about the instrument are given in Connerney et al., 2017b.

Chapter 3

The Study of Jupiter's Polar Auroral Bright Spot Emissions

In this work, the morphology of Jupiter's polar auroral bright spot is investigated. The data are obtained from the Juno-UVS on board Juno spacecraft. These observations give a complete view of Jupiter's auroras, including nightside, which is impossible to see from Earth. Furthermore, in comparison to Hubble Space Telescope observations, the Juno observations allow a longer observation period to study Jupiter's aurora. The UVS instrument and data structure are explained in full in the section 2.1. Section 3.1 describes the analysis in detail. The position of the bright spots, local times, and power variations are the key topics of discussion. The results will be reported in section 3.2 and the discussions in this chapter will conclude in section 3.3.

3.1 Data Set and Data Analysis

The data for this study were collected during the first 25 perijoves (data for PJ2 were not available) , from August 27, 2016 to May 29, 2019. Interactive Data Language (IDL), a commonly used software for astronomical data, is used for image processing and data analysis.

3.1.1 Brightness and Power Emission Analysis

The bright spot's peak emission was originally identified in order to investigate its brightness. The background emission was then removed before identifying the area of the bright spot that is brighter than twice the standard deviation of the surrounding area. The bright spot's edges were fitted as elliptical shapes (red contours in Figure 3.1) to analyze the power fluctuations, and the emitted power in the ellipse was computed. The semi-major axis, semi-minor axis, elliptical center position, and inclination angle are the four outputs of the elliptical fit. The emitted power for each pixel in the ellipse is computed as the product of the brightness, the mean photon energy of a UV photon, and the pixel's area on the planet. The bright spot selection area, computed from an elliptical reference whose size is 25% smaller and greater than the best fit ellipse, is a major source of uncertainty in this study. To compute the overall power in the area of interest for a given perijove, the union of the fitted ellipses from each identified bright spot is considered as a reference surface area. The overall power in the same location for all images in a data set can be used to investigate the power variation. Figure 3.1 illustrates three images with an observable bright spot that are used to generate the reference area for images in the PJ1 data set.

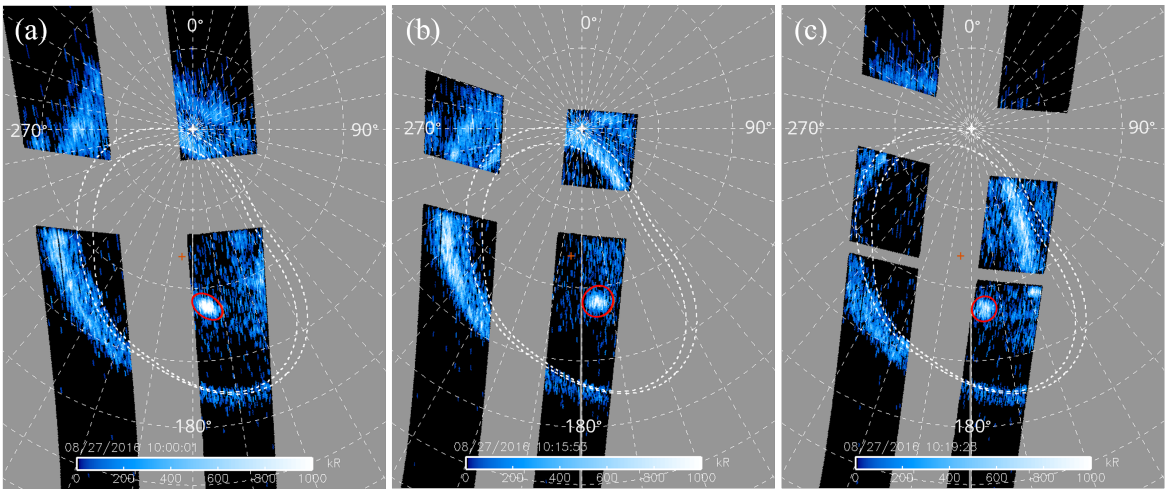

FIGURE 3.1: Three bright spots' emission appeared during PJ1 observation. The red plus sign represents the northern magnetic pole and the red ellipses show the ellipse fit that is defined by the procedure described in the content.

3.1.2 Location and Local Time Analysis

The peak position of a bright spot represents its ionospheric position in system III (SIII) coordinates. Ionospheric magnetic local times are determined using the magnetic pole location of each hemisphere as the center and the longitudinal position that points toward the sun as the noon magnetic local time. The magnetic pole for the southern hemisphere is located at $-86°$ latitude and 340° SIII longitude, at which the magnetic field direction based on the Juno Reference Model through Perijove 9 (JRM09) is vertical. For the northern hemisphere, the magnetic pole is the barycenter of the aurora as defined in Bonfond et al., 2017, at 74° latitude and 185° SIII longitude. Figure 3.2 shows a schematic depiction of how the ionospheric local time is determined.

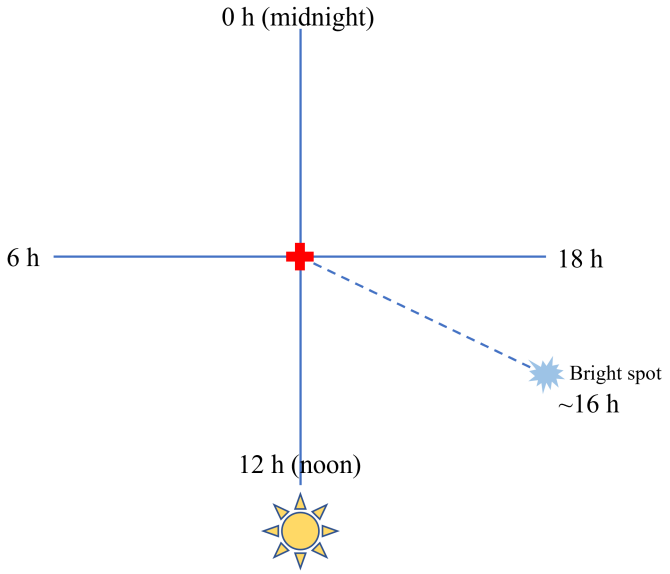

FIGURE 3.2: Schematic shows the calculation of ionospheric local time, seeing from the top view. The red plus sign represents the magnetic pole position. The local time is identified counterclockwise from the sun position from 12 h, 18 h, 0 h, and 6 h, respectively. From this figure, the example bright spot is located at around 16 h.

To suggest the possible responsible source, causing bright spot emission, the magnetosphere-ionosphere mapping flux equivalence method of Vogt et al., 2011; Vogt et al., 2015 coupled with the JRM09 internal magnetic field model (Connerney et al., 2018) were used to obtain the mapped location of magnetic field lines in the magnetosphere and magnetic local time (MLT) corresponding to the bright spot features. This magnetic mapping model is chosen since they account for the bendback of the magnetic field lines and the latest internal field model. The input parameters for mapping from ionosphere to magnetosphere are the subsolar longitude and position in Jupiter's ionosphere (the latitude and the SIII longitude of the bright spot). The outputs from the mapping are the radial distance and the corresponding local time. For a case where the mapping result is beyond 150 R_J or exceeds the dayside magnetopause, the positions are outside the model's limits. Extrapolation is used to determine the approximated local times in the magnetosphere from this mapping. This can be done by tracing a line on the polar projection from the magnetic pole toward the bright spot's location, continuing in an equatorward direction until getting the latitude and longitude that can be mapped to a position inside the model boundary.

3.1.3 Zenith Angle Analysis

The solar zenith angles at the bright spot positions are determined to explore whether the solar UV flux influences the brightness of the bright spot, as shown earlier in the swirl region (Greathouse et al., 2021). The following is used to compute the angle θ:

$$\theta = \arccos(\sin(\phi_g)\sin(\phi_s) + \cos(\phi_g)\cos(\phi_s)\cos(|\lambda - \lambda_s|), \tag{3.1}$$

where θ is the angle between bright spot position and Sun position on a sphere connected via a great circle arc. Anglesθ_g and λ are the graphic latitude and longitude of the spot, while angles θ_s and λ_s are the graphic latitude and longitude of the Sun.

3.1.4 Period Analysis

The Lomb-scargle periodogram is used to analyze the period of brightness variation of the bright spot emissions. This periodogram is an IDL software analysis tool for frequency/period analyses of data that is not acquired at a regular time interval or has missing data. Since the bright spot is observed for long sequences ($\sim$ 4 hours) and their power fluctuation pattern is likely to have pulsating behaviors, this tool is used to analyze the power variations from PJ4 and PJ16.

3.2 Results

The northern bright spots are discovered during 5 perijoves and the southern bright spots are found during 12 perijoves from the first 25 perijove data. PJ1, PJ3, PJ6, PJ8, and PJ13 detected northern spots, while PJ4, PJ8, PJ9, PJ12, PJ14, PJ15, PJ16, PJ20, PJ21, PJ22, PJ23, and PJ24 detected southern spots. It is worth noting that, during PJ3, PJ12, PJ21, and PJ23, two distinct bright spots are seen during the same sequence. Appendix A contains UV polar projection images of bright spots. Overall, bright spots are sometimes small (e.g., PJ8 northern spot), sometimes compact (e.g., PJ3 spot), and sometimes very large (e.g., PJ16 spot). The smallest surface area covered by the bright spot is around 3,500 km^2, while the biggest area is 2.07×10^7 km^2. These bright spots emit power in the tens of gigawatts to a hundred gigawatts range. Furthermore, the findings suggest that bright spot emission might return to the same position within a perijove. The summarized properties of bright spot emissions are shown in Figure 3.3. The surface area and emitted power are represented

in the top two panels, while the total magnetic flux is represented in the middle panel, which corresponds to the bright spot area. The ionospheric local time and the solar zenith angle shown in the last two panels will be discussed later.

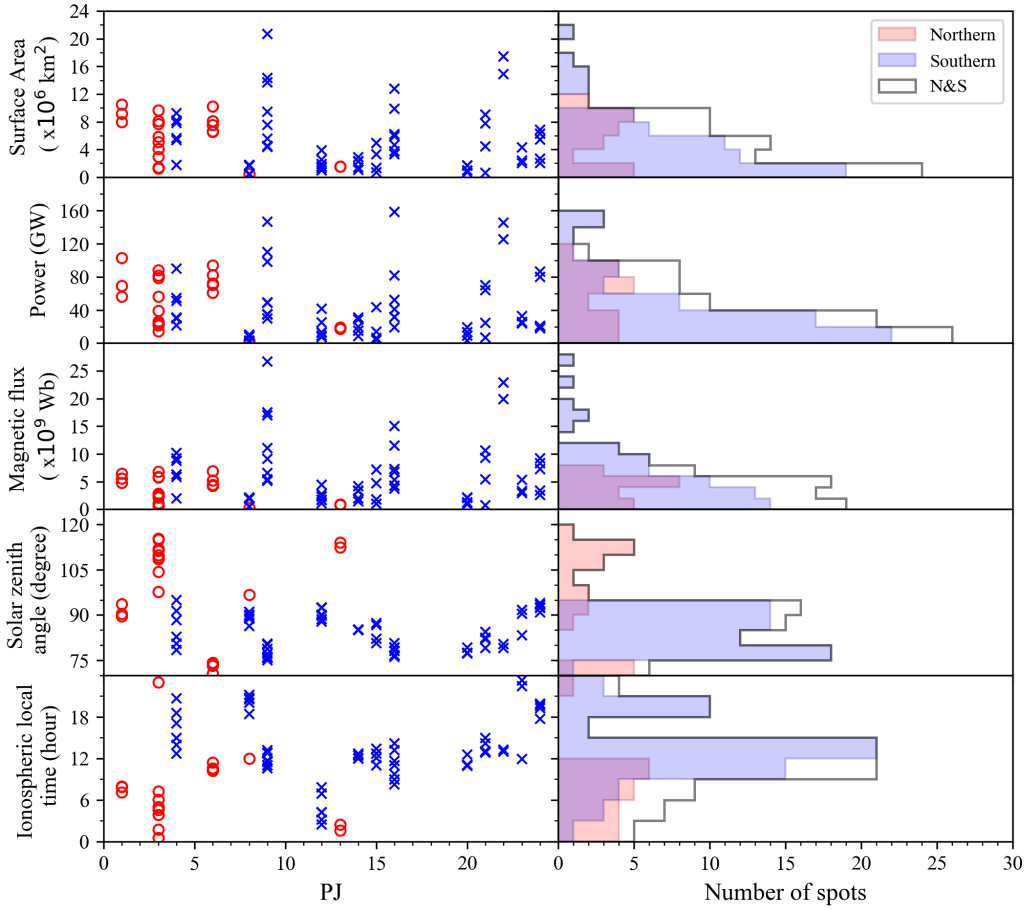

FIGURE 3.3: The distribution plots show bright spot properties modified from Haewsantati et al., 2021 representing the bright spot area, the power emissions, the total magnetic flux corresponding to surface area, the ionospheric local time, and the solar zenith angle at bright spot. The data from each perojove is displayed on the left plot, while the histograms, combining the data of the northern and southern spots are displayed on the right plot.

3.2.1 Bright Spot Positions in System III

The positions of bright spots are plotted as shown in Figure 3.4. It is obvious that the bright spots found in northern hemisphere are mostly concentrated in a specific region, roughly between $60 - 70^\circ$ N planetocentric latitude and $150 - 190^\circ$ W (SIII). Surprisingly, this is the same location that the X-ray auroral emission study called the "X-ray Hot Spot Region" (Dunn et al., 2016; Dunn et al., 2017; Dunn et al., 2020; Gladstone et al., 2002; Weigt et al., 2020). The bright spot from PJ8, at $\sim 82^\circ$ N and 216.5° W(SIII), is an exception to the northern spots data. The bright spots in the southern hemisphere, on the other hand, display

contrast results. The bright spots are scattered around the magnetic pole rather than appearing in a restricted location. The surface magnetic field strength according to the JRM09 model is also shown in Figure 3.4. The bright spot locations in both hemispheres indicate that these spots are most likely to appear where the magnetic field strength is greater than 8 Gauss (8×10^5 nT). An exception is once again a northern spot during PJ8.

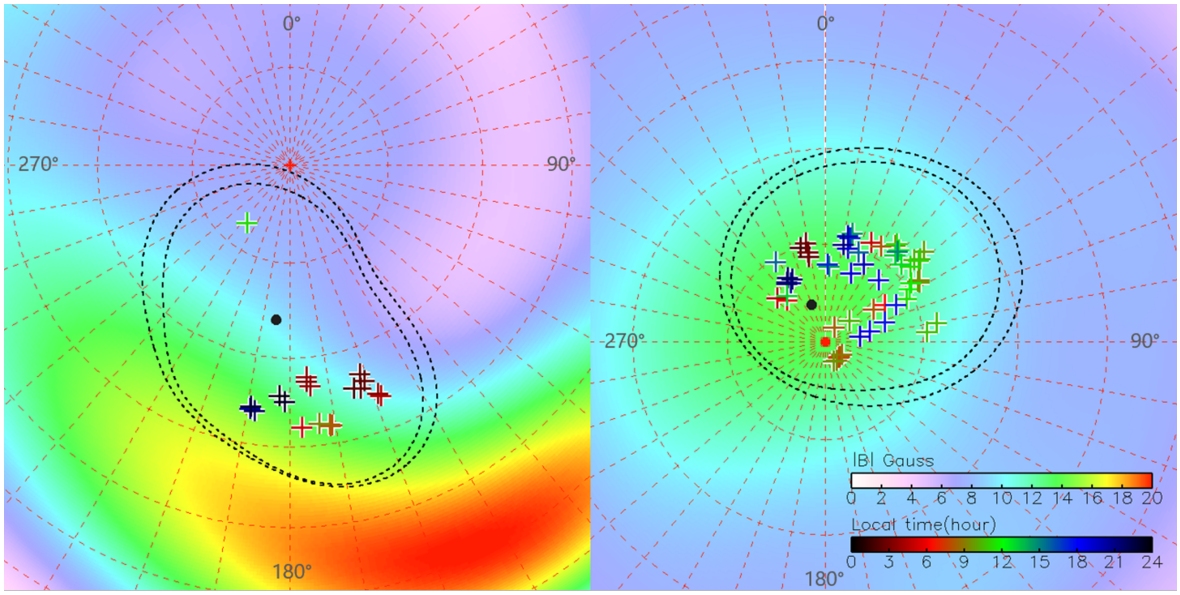

FIGURE 3.4: Polar projections (Left figure for Northern hemisphere and Right figure for southern hemisphere) show distribution of bright spot over the magnetic field strength based on JRM09 model. Black dots present the magnetic pole position in each hemisphere (Haewsantati et al., 2021).

For the investigation of sunlight's influence to the bright spot emission, the last panel in Figure 3.3 reveals that the solar zenith angles at the northern bright spots are between $70 - 95^\circ$ whereas the solar zenith angles at southern bright spots are between $70 - 120^\circ$. Zenith angles greater than 90° mean that the Sun is below the horizon, indicating nighttime, while the zenith angles less than 90° mean the Sun is above the horizon, indicating daytime. This result indicates that the Sun was close to the horizon and below the horizon when the bright spots appeared. This finding suggests that bright spot emission is unaffected by the Sun's visibility.

3.2.2 Bright Spot Positions with Respect to Swirl Region

The color ratio is used to represent the swirl region in Jupiter's polar aurora in this study. The color ratio is defined as the ratio of H_2 auroral intensity that is not affected by methane absorption to H_2 auroral intensity that is affected by methane absorption, i.e. $I(1550 - 1620\text{Å})/I(1250 - 1300\text{Å})$. More information on the color ratio is described in section 1.4.1. However, the denominator $I(1250 - 1300\text{Å})$ is shorter than discussed in section 1.4.1 in order to minimize the contamination of the bright instrumentally broadened Lyman-α line. Figure 3.5 shows examples of color ratio maps from the same perijove of the overplotted bright spots. The finding from all perijoves shows that the observed bright spots tend to be at the boundary of the swirl region (the high color ratio region). However, PJ1 shows a contrast result (Figure 3.5(c)), the appearances of the bright spot are inside the swirl region.

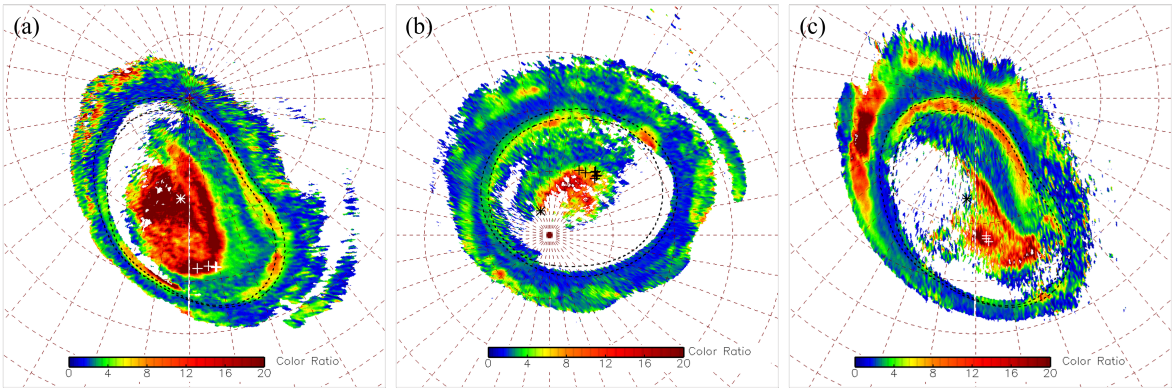

FIGURE 3.5: The color ratio map with the overplotted bright spot (plus sign) emissions observed during (a) PJ6, (b) PJ16, and (c) PJ1. The asterisk in each image is the position of magnetic pole in SIII (Haewsantati et al., 2021).

3.2.3 Positions in Magnetosphere and Magnetic Local Times

The bright spots are predominantly mapped to positions in the magnetosphere at distances beyond 150 R_J, according to Vogt's magnetic flux equivalent mapping combined with the JRM09 internal magnetic model. This result implies that the magnetic field lines connected to the bright spot extend beyond the dayside magnetopause or the model's limit. The extrapolation method is used to map these positions once again. Figure 3.6 position magnetosphere shows the estimated positions of the bright spots in SIII that can be mapped by model, as well as the magnetic local time represented by different colors in the plot. The northern spots have local times ranging from late evening to late morning, while the local time for southern spots scatter throughout the entire time range. These broad local time ranges correspond to wide ionospheric local time distributions as illustrated in Figure 3.3d. Despite the fact that the extrapolation approach is used and the local time may not be completely accurate, the results reveal that the bright spot does not correspond to any specific local time, contrary to previous ideas. For example, Pallier and Prangé, 2001; Pallier and Prangé, 2004 suggested that bright spot emissions may correspond to noon local time related to magnetospheric cusp. However, the previous studies have largely been understood from the perspective of the Earth. For example, the HST observations where images were taken primarily while Jupiter's magnetic pole faced the Earth, and image were only view by telescope on the dayside of Jupiter. As a result, the bright spots were only visible during when it was in daytime, leading to those previous conclusions.

3.2.4 The Reappearance of Bright Spot Emissions

In many perijoves, the bright spots were observed many times. In Figure 3.7, a cylindrical map shows how their locations change over time. This map shows bright spots from both hemispheres, where the perijove and hemisphere are labeled by different color (blue color for northern spots and red color for southern spots). The plot indicates that bright spot positions usually shift slightly in both latitude and longitude. Accordingly, the distances can vary by thousands of kilometers. The only group whose positions shift noticeably is the northern spot from PJ3 and the southern spots from PJ9, PJ16, and PJ24. For southern spots from PJ14 and PJ15, their distance shifts are actually quite small since they located in high latitude (beyond $\pm 85°$) close to the rotational pole. The northern bright spot in PJ3 (seen in deep blue in Figure 3.7) shifts from 164 ° W (SIII) to 158 °W (SIII) in longitude and 3 ° shifted in latitude. The southern spot from PJ9 appears to vary from low to high latitude (from $-76°$ to $-80°$) and 15° shifted in SIII longitude (47° W$-$62° W), whereas PJ24 spot

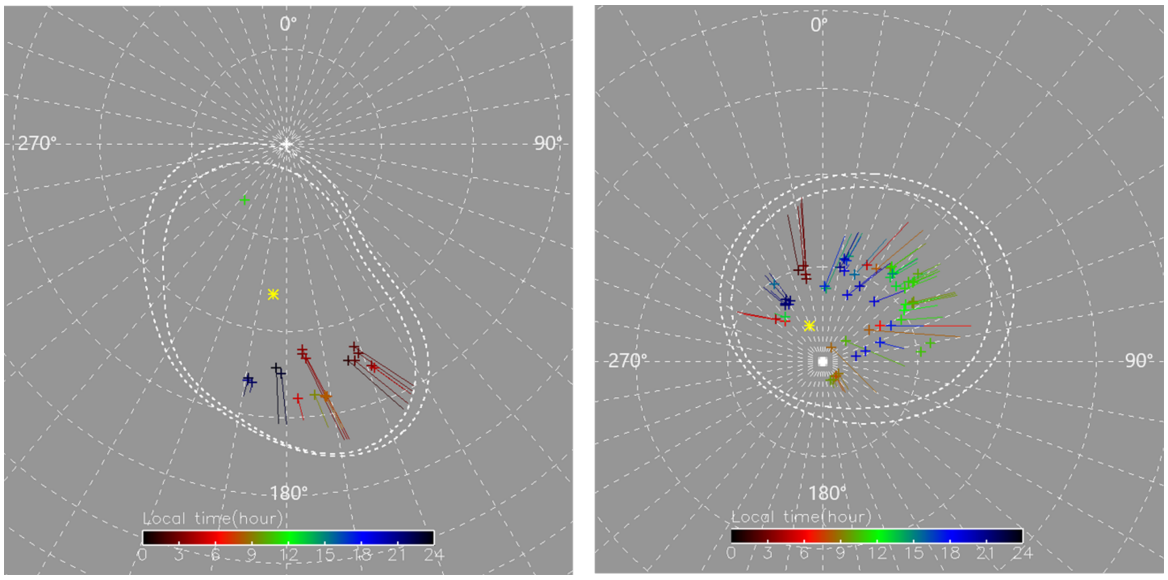

FIGURE 3.6: Polar projection images present bright spot position in SIII. Left figure is for northern spot and Right figure is for southern spot. Yellow asterisk indicates the magnetic pole in each hemisphere. The straight lines are the tracing paths drawing from the magnetic pole through the bright spot position in direction toward any latitude and SIII longitude along the line that can be mapped to the position in magnetosphere by using Vogt's mapping (Vogt et al., 2011; Vogt et al., 2015) coupled with JRM09 model (Connerney et al., 2018). The color of bright spot corresponds to the magnetic local time obtained from the mapping. (Haewsantati et al., 2021)

appears to shift mostly in longitude (from 20° W−70° W). In most cases, the shift of the bright spots is very small, suggesting that their positions are essentially fixed in system III as Jupiter rotates. However, the changing rates of bright spot positions are independent on Jupiter's rotation period. The changes can be either an increase or a decrease in SIII longitude, with no systematic pattern.

3.2.5 Power Variations

In the previous section, a bright spot from a specific perijove reappeared at a roughly similar location. The time interval between two consecutive brightenings from certain perijoves is approximately a few minutes, while some perojoves take more than ten minutes. The time interval for bright spots reappearing in an entire data set is between $3 - 47$ minutes. This result could connect bright spot emissions to QP emissions, as several polar features have been proposed to have QP behaviors with periods ranging from a few to many ten minutes. However, the study of pulsation emissions of bright spots is limited by the discontinuous sampling rate because the instrument's FOV varies significantly over time. In addition, as the mission continued, the observation period for northern hemisphere decrease from a few hours to a few ten of minutes. Fortunately, there are two particular cases that the observing time is long enough ($3 - 4$ hours) to study the power variations of bright spot emissions, which are observations from PJ4 and PJ16.

Figure 3.8 and Figure 3.9 show the power variation of the southern spot form PJ4 and PJ16, respectively. Since the instrument sometimes points at other part of the aurorae, the gray shaded areas indicate the times when the UVS' view did not cover more than 50 % of the union of fitted ellipses of the bright spot emissions in the perijove. From the plots, the power emissions of the identified bright spots (indicated by black arrows) which is a peak of the power variation plot are greater than 35 GW with the highest power of 170 GW. Furthermore, the plots exhibit a clear repetitive pattern, in which the bright spots reach a

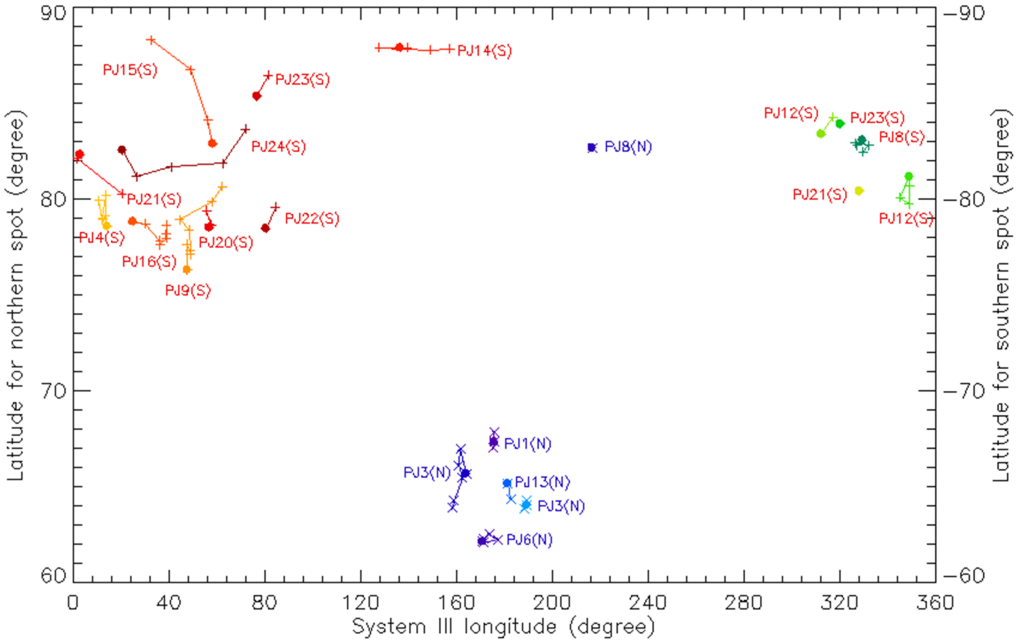

FIGURE 3.7: The cylindrical map displays the latitudes and SIII longitudes of bright spots in the northern (crossed signs) and southern (plus signs) hemispheres. The motion of the bright spot in the observing time sequence is represented by the lines connected to each data, with the large dot representing the first observed position of the bright spot in each perijove. (Haewsantati et al., 2021)

peak at a specific time interval. For PJ4, six bright spots appeared for every $\sim$ 30 minutes with an additional peak indicated by red arrow for which UVS detects no unambiguous bright spot. In addition, a peak appears to be missing between the last two identified spots. This could be because the bright spot was in a shadowed area or because there was no bright spot at this time. Additional peaks (red arrows) are more common in PJ16 than in PJ4. These peaks correspond to diffuse features that aren't recognized as bright spot emission. However, in both PJ4 and PJ16 the peaks are close to a shaded area when bright spots might have been present out of the instrument's field of view.

For more details, from applying the Lomb-scargle analysis, the results show that power variations for PJ4 shows a periodic pattern with period $\sim$ 28 minutes, as shown in Figure 3.10. As well as period analysis for PJ16, the bright spots tend to repeat their appearances with the period of 23 minutes. These periods are much longer than the QP flares in polar region reported by Bonfond et al., 2011, whose analyzed periods are only $2-3$ minutes. Indeed, the period of bright spot emissions are more similar to the other QP phenomena in Jupiter's aurorae (Dunn et al., 2016; Jackman et al., 2018; MacDowall et al., 1993; McKibben, Simpson, and Zhang, 1993; Wibisono et al., 2020), as will be described in the next section.

3.3 Conclusions

The result of this study is quite surprising, as it contradicts earlier investigations. Bright spot emissions were suggested to appear near noon magnetic local time and relate to the magnetospheric cusp process. However, this study shows that the bright spot can be found in various ionospheric local times and mapped to wide ranges of magnetic local times in magnetosphere. The additional information obtained from this study is that the bright spots

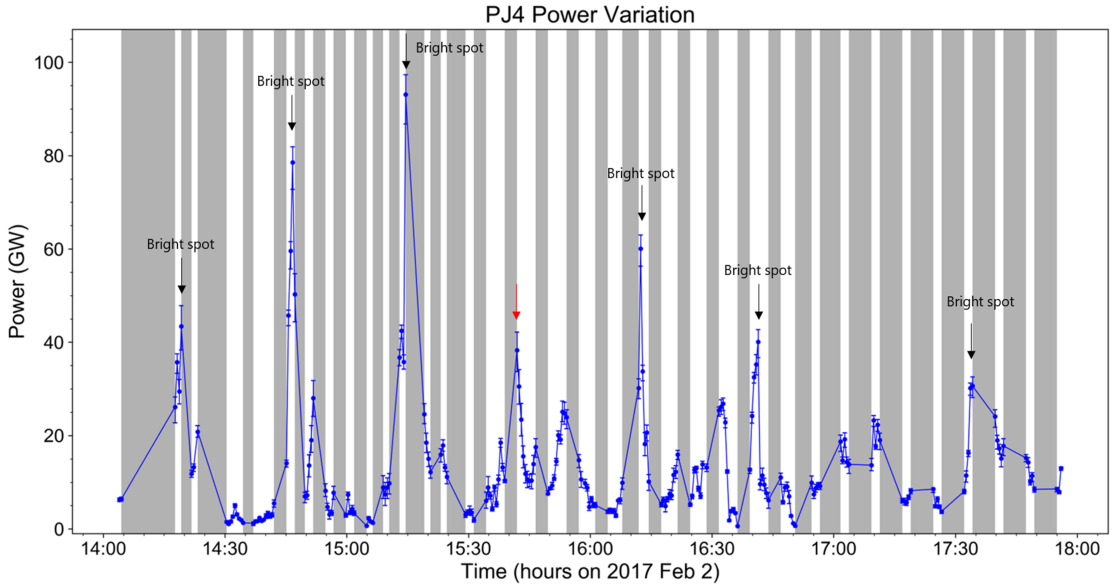

FIGURE 3.8: Time variation of PJ4 spot's emission power observed on 2 February 2017 during 14:00 UT - 18:00 UT. The shaded gray areas represent times when the bright spot areas are <50% in the UVS' view. The error bars correspond to the intensity uncertainty of the power in the 25% range of ellipse area. (Haewsantati et al., 2021)

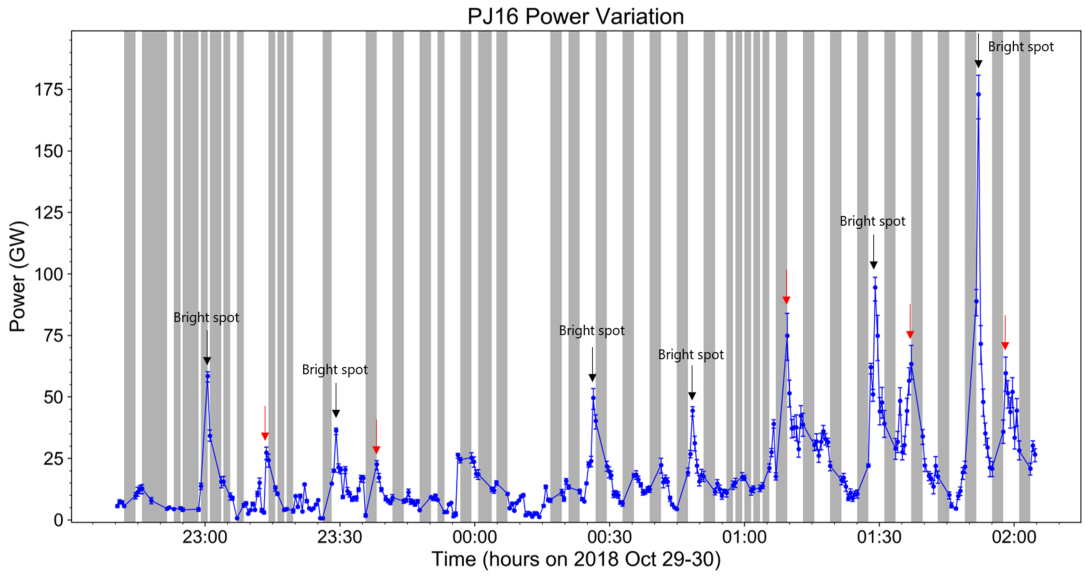

FIGURE 3.9: Time variation of PJ16 spot's emission power observed on 29-30 October 2018 during 22:30 UT - 02:30 UT. The shaded gray areas and error bars are similar with Figure 3.8. (Haewsantati et al., 2021)

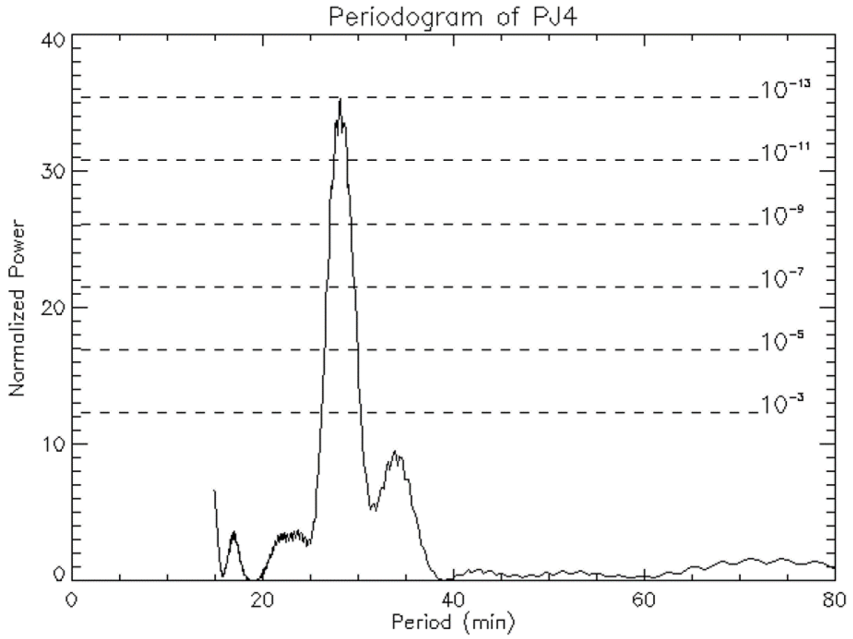

FIGURE 3.10: Fitted result from Lomb-Scargle analysis for bright spots during PJ4. The horizontal dash-lines are the significant level of fitting, lower significant implies high probability of the fitted period. The highest peak of normalized power for PJ4 is at a period of 28.18 minutes. (Haewsantati et al., 2021)

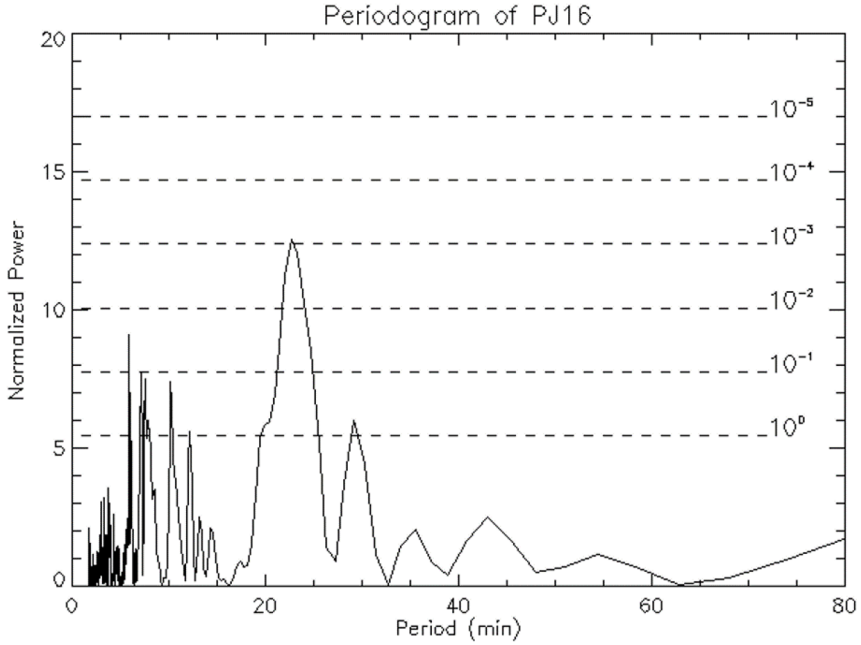

FIGURE 3.11: Fitted result from Lomb-Scargle analysis for bright spots during PJ16. The clearest peak of normalized power for PJ16 is at a period of 22.68 minutes. (Haewsantati et al., 2021)

mostly lie near the edge of the swirl region. Furthermore, the bright spot from a particular perijove can reoccur at approximately the same SIII position, implying that the source region should corotate with Jupiter rather than originating from a fixed position in the magnetosphere. Even though the local times and positions appear to rule out a direct link between bright spot emissions and a noon-facing magnetospheric cusp, this process is based on a simple magnetospheric topology, such as that found on Earth. However, Zhang et al., 2021 proposed that the polar-most field lines for Jupiter could be extremely complicated, resulting in an anomalous characterization of Jupiter's magnetospheric cusp and a lack of clarity in magnetic field line mapping. If this idea is taken into account, the bright spot might still be linked to the magnetospheric cusp with one more step complicated than Earth case.

Another intriguing result from this research is that the formation of bright spots is not a sporadic random event, but rather recurs many times around the same location, implying that they are quasiperiodic emissions. The bright spot exhibits quasiperiodic characteristics with the 22-28 minute period, according to the study in PJ4 and PJ16 spots with the long observation times. Despite the fact that the HST can detect Jupiter's aurorae and can be used to study the auroral characteristic, the period analysis cannot be done, because the HST observations are limited to $\sim$45 minutes. The 22-28 minute period variation of the bright spot emissions found in this study is in the longer time scale when compared to the flares in Jupiter's aurorae, which are very bright and have been suggested to have a QP behavior(2-3 minutes period, Bonfond et al., 2011; Bonfond et al., 2016; Nichols et al., 2017a). Furthermore, these two features appear at different positions in polar regions. Bright spots normally appear at the swirl region's edge, while flares usually occur in the active region's noon and dusk side (Bonfond et al., 2016; Nichols et al., 2017a). Instead, the 3-47 minutes time interval between two consecutive bright spot emissions rather close to the period range of other quasiperiodic pulsations. Those QA pulsations are, for example, QP emissions in radio emissions studied by MacDowall et al., 1993, relativistic electrons reported by McKibben, Simpson, and Zhang, 1993, Alfvén waves process (Manners, Masters, and Yates, 2018) and X-ray pulsations (e.g., Jackman et al., 2018; Wibisono et al., 2020). Therefore, further study for connections between these phenomena might provide information to understand and suggest a responsible process for the bright spot emissions.

Chapter 4

The In-situ Observations and Remote Sensing of Jupiter's Polar Bright Spot Emission

This chapter presents the noteworthy occasions where Juno's position, as calculated by the JRM09 model, crosses that of the bright spot, implying that Juno flew across magnetic field lines connecting to bright spot emissions. These events occurred during PJ3, PJ15, and PJ33. Therefore, in situ observations provide an opportunity to simultaneously investigate how waves and particles behave that might be associated with the bright spot emissions. The data are obtained from JADE, JEDI, and Waves instruments. This work also looks for any signatures of magnetospheric processes that might be related to the bright spot emissions by studying the magnetic disturbances from magnetic field observations by the MAG instrument. The scientific instrumentation is discussed in Chapter 2, while section 4.1 gives details on data used in this study. Results for all three PJs are presented from section 4.2 to section 4.4 and concluded in section 4.5.

4.1 Data Analysis

This study focuses on three events: a) Northern spot during PJ3, which was captured by Juno-UVS at 15:36:26 UT on 11 December 2016, b) Southern spot during PJ15, which was captured by Juno-UVS at 02:28:55 UT on 7 September 2018, and c) Southern spot during PJ33, which was captured by Juno-UVS at 01:38:30 UT on 16 April 2021. The selected spin is based on the time which Juno footprint according to the JRM09 model is closest to the bright spot position. A method similar to that given in section 3.1 is used to analyze the bright spot characteristics (brightness, surface area, power emissions, and SIII positions).

Particle data related to auroral emissions are provided by JADE and JEDI. However, JADE only detected signatures of penetrating radiations during the study period. Therefore, low-energy particles could not be analyzed. Thus, this study can focus only on high energy charged particles observed by JEDI instruments. The JEDI's observations of particle energy and particle pitch angle distributions in the $30 - 1,200$ keV energy range derived using the magnetic vector provided by MAG observations will be presented in this study. The energy distributions for upward particles (pitch angle $0^\circ - 30^\circ$ compared to magnetic field vector for northern hemisphere and pitch angle $150^\circ - 180^\circ$ for southern hemisphere) and downward particles (pitch angle $150^\circ - 180^\circ$ for northern hemisphere and pitch angle $0^\circ - 30^\circ$ for southern hemisphere) are also shown. The numerical intensity of upward and downward particles is presented by the energy flux in order to see the dominant particles.

The wave features, such as wave modes and propagation direction, are studied to investigate the influence of waves on auroral emissions. The ratio of electric to magnetic field or E/cB ratio (where c is speed of light) and the detected characteristic frequencies of plasma

measured by the in-situ measurements from MAG. are used to identify wave mode propagation, i.e. electromagnetic or quasi-electrostatic waves. Examples of those characteristic frequencies are an electron cyclotron frequency (f_{ce}), calculated by $f_{ce} = 28|B|$, where $|B|$ measured in nT, an electron plasma frequency (f_{pe}), $f_{pe} = 8980\sqrt{n_e}$ where n_e is electron number density measured in cm^{-3} (Gurnett and Bhattacharjee, 2005a), and an ion cyclotron frequency (f_{ci})), presented in Figure 4.1. Whistler-mode waves, which were found in this study, is identified by a quasi-electrostatic wave by the $E/cB > 1$ and propagates at frequency below the minimum of f_{ce} or f_{pe}. Another analysis, for waves propagation direction, considers the Poynting vector along the x-axis by the comparison between the electric and magnetic phases, under the assumption that the direction of Poynting vector is close to the direction of Jovian background magnetic field and some certain circumstances (Kolmašová et al., 2018).

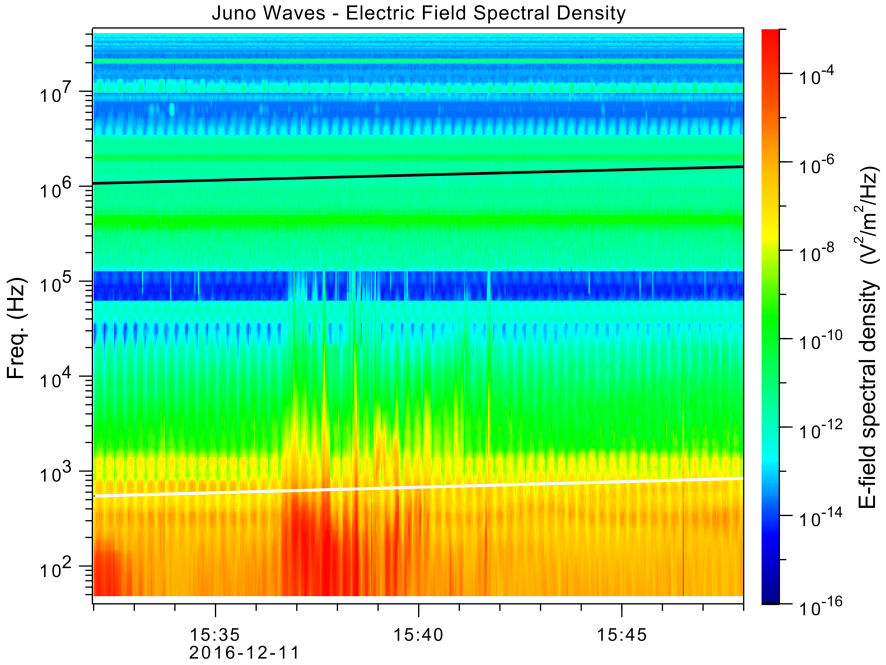

FIGURE 4.1: Example of Frequency-time spectrogram of electric field spectral density with the overplot of (black line) electron cyclotron frequencies and (white line) proton cyclotron frequencies observed by the Waves instruments during PJ3. (Haewsantati et al., 2022 (submitted))

To investigate magnetospheric signatures connected to the bright spot emissions, this work focuses on the 1-s resolution magnetic field perturbations in each component throughout the focus time. The magnetic perturbation is the remaining magnetic field strength after the observed magnetic field has been removed by the planetary magnetic field calculated by the JRM09 and the magnetodisc model (Connerney et al., 2020).

It is worth noting that the JRM09 mapping might have some inaccuracies. For example, Allegrini et al., 2020 reported a 90s delay between the projected UV brightness crossing time, where position is based on the JRM09 model, and the electron flux peak observed by JADE. Therefore, the timing uncertainty should be taken into consideration when comparing UVS with other instrument's results.

4.2 PJ3 Results

Bright spot emission during PJ3 is shown in Figure 4.2, where Juno position is very close to the bright spot position (in red circle). The bright spot detected at the last spin was located

at latitude 64.3°N and longitude 159.6°W (SIII) and emits a power of $\sim$ 20 GW. Since the UVS' view pointed at other auroral regions and there was no definite bright spot emission detection due to the UVS data stream, there was a data gap from 15:33 UT to 15:38 UT, while the bright spot was in the area covered by a narrow slit at a time after 15:38 UT to 15:42 UT. Therefore, this emission is considered as part of bright spot sequence, where the identified bright spot were found at 15:21 UT and 15:42 UT with the powers of $\sim$ 24 and $\sim$ 81 GW, respectively, as discussed in Chapter 3 (and a table list in Appendix B). However, this bright spot is chosen to study since its mapped position is close to the path of Juno's magnetic footprint.

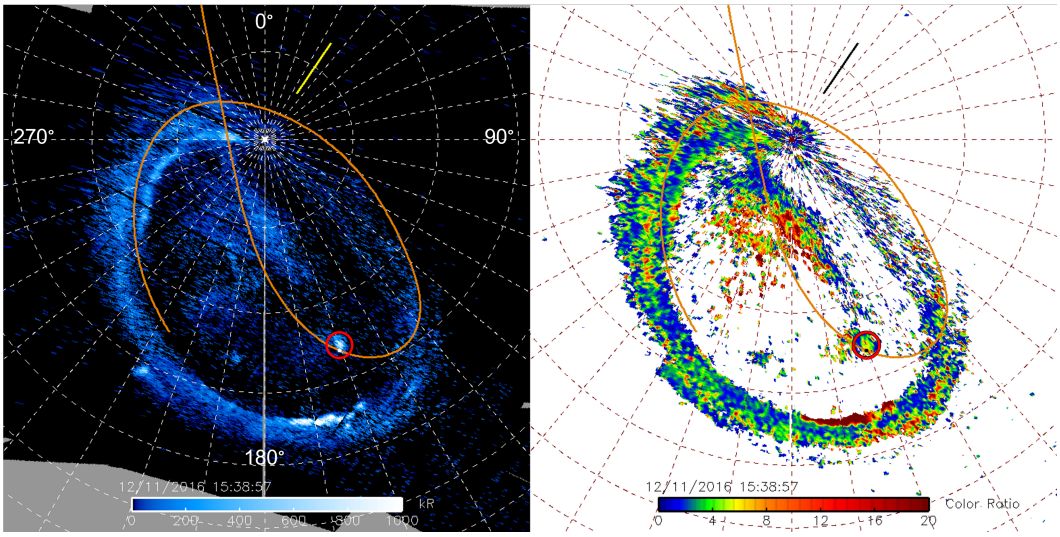

FIGURE 4.2: Polar projections show a bright spot in (left) UVS UV emission and (right) the color ratio. The image is created by combining 100 UVS spin images where the bright spot appearing in last spin at 15:38:26 UT on 12 December 2016 during PJ3. The yellow line represents the Sun's direction at time of the last spin. Red circle indicates the bright spot position during which Juno position (white dot) along Juno footprint path (orange line) according to the JRM09 model is close to the bright spot (Haewsantati et al., 2022 (submitted)).

As shown in figure 4.3, the intensifications of electric field and magnetic field spectral densities are clearly seen from 15:36:30 UT to 15:40:00 UT, which cover the time of the bright spot detection. The E/cB analysis (top panel in Figure 4.4) shows a ratio of $1.0 - 2.0$, suggesting the presence of electromagnetic waves. In addition, the intensification is seen at frequency higher than proton cyclotron frequencies (black line in Figure 4.3), where the electron cyclotron frequencies are higher than 10^6 Hz (as showed by black line in Figure 4.1), implying that waves are in whistler-mode. Furthermore, the Poynting flux direction is parallel to the planetary magnetic field direction, indicating the upgoing direction of the waves for the northern hemisphere. As a result, during the time of UV bright spot detection, Waves instruments observed the intensifications of the whistler-mode hiss waves that were traveling upward, away from Jupiter.

The JEDI results show that during the time of interest, electrons are more dominant than ions species. Hence, only electron's energy and pitch angle distributions are shown in Figure 4.5. The quantitative measurement of energy flux for upward and downward electrons are presented in the last panel. For comparison, the frequency-time spectrogram of electric field density is shown in panel (a). The results show that electron intensities started to enhance from $\sim$15:37 UT to 15:42 UT (when the intensifications of whistler-mode waves began a few seconds earlier). This time interval also covers the time when Juno's magnetic footprint was closest to the bright spot. Despite the fact that magnetic mapping is subjected to have some uncertainties, it is difficult to determine the actual position of Juno's footprints in relation

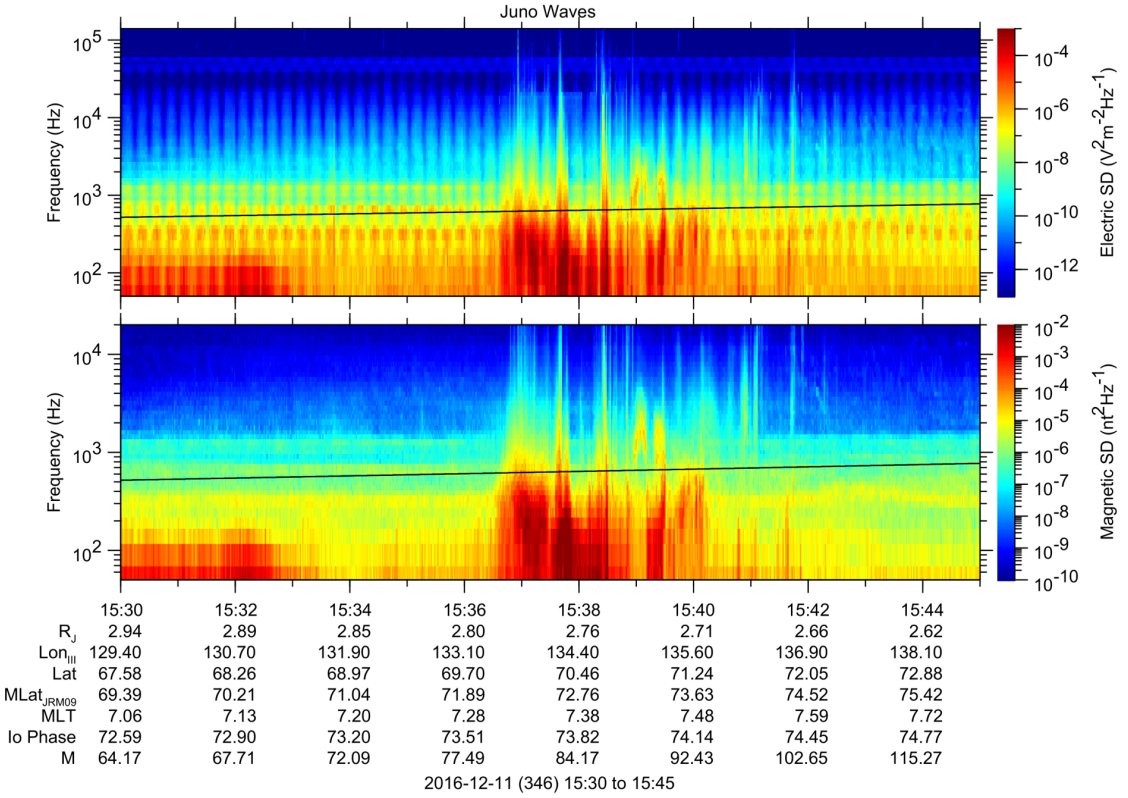

FIGURE 4.3: Frequency-time spectrogram of (top) electric field spectral density and (bottom) magnetic field spectral density were observed by the Waves instruments during PJ3. Black lines represent the proton cyclotron frequencies (William Kurth, 2021, private communication).

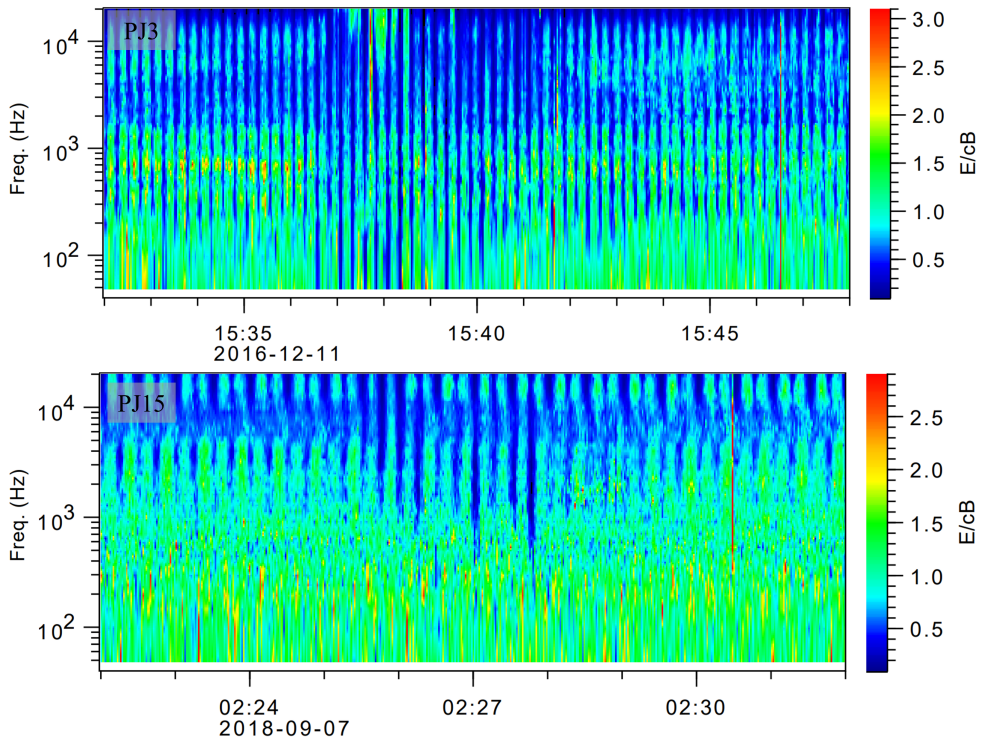

FIGURE 4.4: Frequency-time spectrogram shows E/cB results for (Top) PJ3 and (Bottom) PJ15, adapted from Haewsantati et al. 2022 (submitted).

to the bright spot. However, we believe that Juno was close enough to the bright spot to assess the connection between bright spot emission observed by UVS and the particle flux detected by JEDI. Furthermore, as seen in Figure 4.13(d), the enhancement is dominated by the upward electrons. Figure 4.13(f) clearly indicates upward electron dominance, where the upward electron energy flux (blue plot) are larger than downward electron energy flux (red plot) throughout time interval. The upward electron energy flux reached $\sim$ 900 mW/m^2 when Juno came close to the bright emission (during 15:38 UT - 15:39 UT), while the downward electron energy flux was below 70 mW/m^2.

Lastly, measurements from MAG instruments (Figure 4.6) show that the magnetic deflections at approximately 15:40 UT were seen in all three components. The maximum fluctuation amplitude is in the order of 100 nT, which is significant suggesting the presence of strong field-aligned currents.

4.3 PJ15 Results

For the second case, the UVS image showing the southern bright spot found during PJ15 is presented in Figure 4.7. The bright spot is located at the latitude 82.4°S and longitude 58.2°W (SIII) with the power emissions of $\sim$ 6 GW. This is a bright spot that was identified in the previous chapter and Appendix B. Even though the emitted power is low in comparison to the bright spot detected in PJ3, the color ratio is high (around 15), indicating that the penetrating particles are highly energetic.

Figure 4.8 and Figure 4.4 (bottom panel) show observation data from Waves instruments with the similar results as found in PJ3; the intensifications of electromagnetic Whistler-mode waves during time interval covering the bright spot detection time as well as the direction of Poynting flux antiparallel to the planetary magnetic field, indicating the upgoing waves. The most noticeable result which differs from PJ3 is that the waves were intensified at time before 02:28 UT and then damped during the time of the bright spot detection, during 02:28 UT - 02:30 UT.

The results from JEDI observations during PJ15 are shown in Figure 4.9, which has similar plot structures to Figure 4.5. The pitch angle distributions show the same pattern as PJ3, with upward electrons dominating over the time interval of interest. Furthermore, the electron energy flux reveals that the upward energy flux with pitch angle 150-180 deg in the southern hemisphere (red plot) is greater than the downward energy flux with pitch angle 0-30 deg (blue plot). However, the energy distributions show no significant enhancements, while small fluctuations can be seen in the plot at a time before and after UVS detected bright spot emission. The small fluctuations are an upward electron intensification before 02:25 UT (which is a time before Whistler-mode waves intensification) and twice upward electron intensifications at around 02:30 UT). The 02:30 UT intensifications are represented in panel (f) by two peaks with upward electron energy flux of 30-40 mW/m^2. In contrast, the energy flux for downward electrons at that time is less than 5 mW/m^2. While the upward electron energy fluxes are lower than those in PJ3 (30-40 mW/m^2 in comparison to 900 mW/m^2 in PJ3), the lower fluxes correspond to the lower emission power of the bright spot in PJ15.

The signatures of magnetospheric processes related to the PJ15 spot are also investigated. However, as shown in Figure 4.10, all three components show magnetic deflections but the maximum amplitude is only 20 nT, which is quite small. Since the field-aligned currents mapping to the distant magnetosphere are not significant, they do not seem to be responsible for the generation of the bright spot in this case.

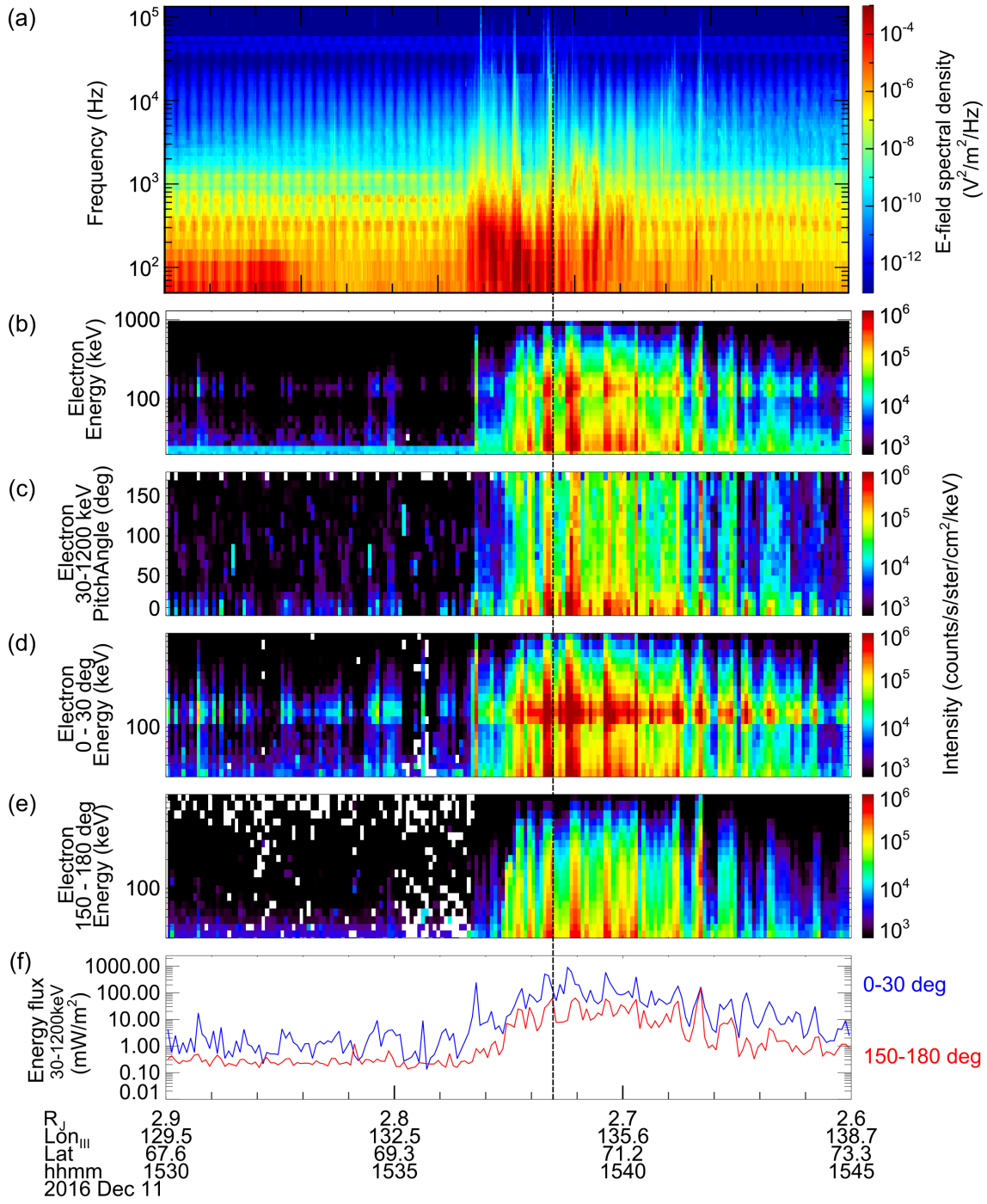

FIGURE 4.5: (a) Frequency-time spectrogram of electric field spectral density observed by Waves instruments. (b) Observation electron energy distributions with 5-s bin resolution. (c) Observation of electron's pitch angle distributions in energy range $30 - 1,200$ keV with 5-s bin resolution. (d) and (e) Observations of 5-s bin energy distributions of upward and downward electrons, respectively. (f) Energy flux for upward electrons with the pitch angles 0-30 deg (blue plot) and downward electrons with the pitch angle 150-180 deg (red plot), in the energy range of $30 - 1,200$ keV. Black vertical dashed line indicates the time of bright spot crossing observed by UVS (Haewsantati et al. 2022 (submitted)).

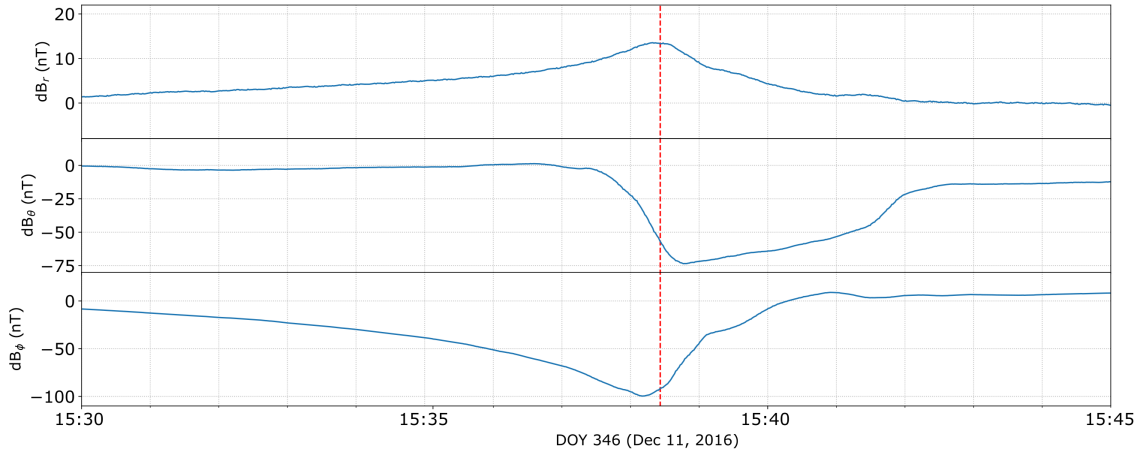

FIGURE 4.6: Magnetic field perturbation in each component during PJ3 observed by Juno MAG. Red vertical dashed line indicated time of bright spot detected by UVS (Haewsantati et al., 2022 (submitted)).

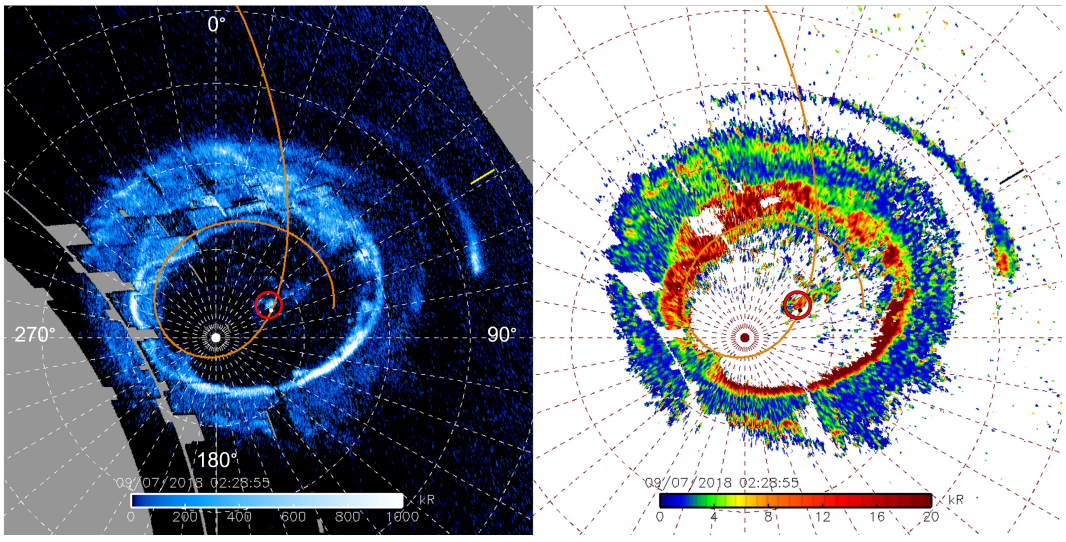

FIGURE 4.7: Polar projection shows a bright spot in (left) UVS brightness image and (right) color ratio image during PJ15. The image is created by combining 100 UVS spin images where the bright spot appeared in the last spin with the same coordinates as described in Figure 4.2 (Haewsantati et al., 2022 (submitted)).

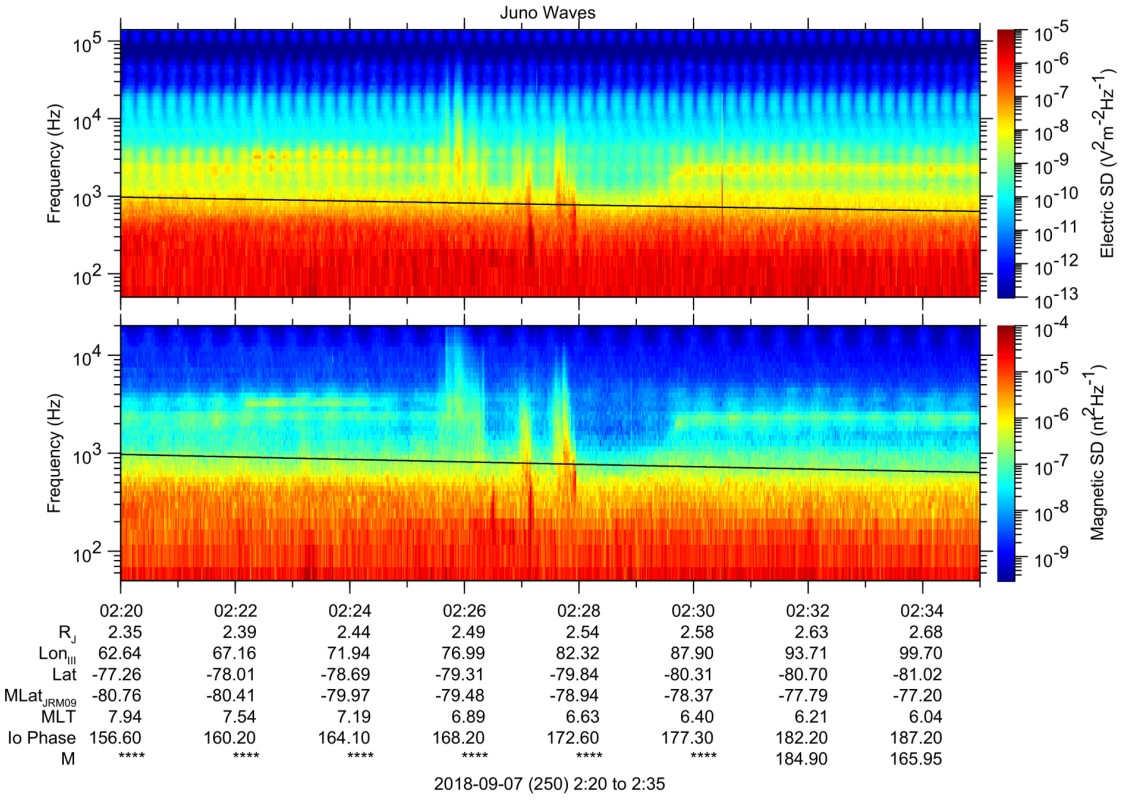

FIGURE 4.8: Frequency-time spectrogram of (top) electric field spectral density and (bottom) magnetic field spectral density observed by the Waves instruments during PJ15. Black lines represent the proton cyclotron frequencies (William Kurth, 2021, private communication).

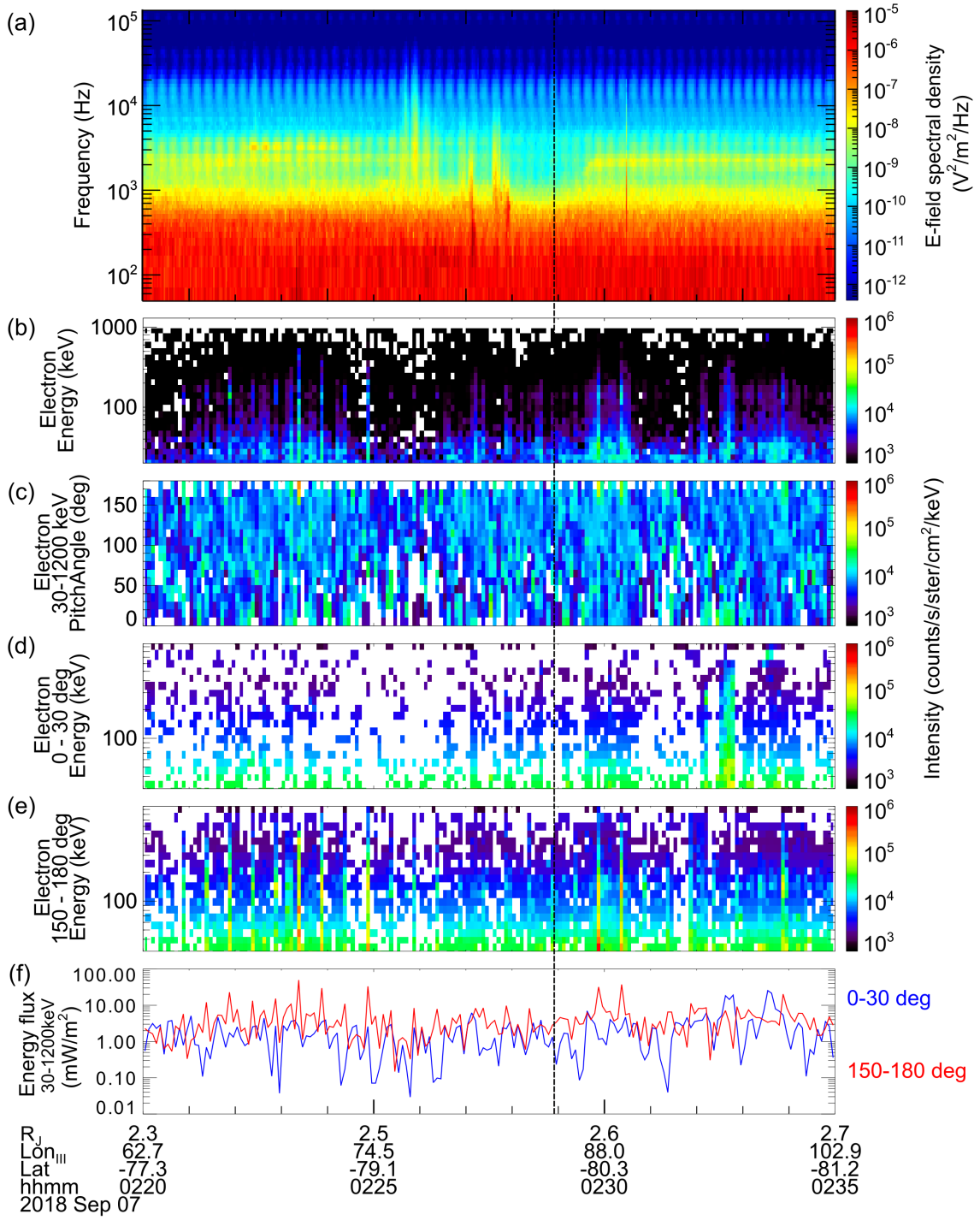

FIGURE 4.9: Observations of Electric field spectral density observed by Waves and particle distributions observed by JEDI during PJ15. Panel (a) to (f) and black vertical line are similar as described in Figure 4.5. Note that for the southern hemisphere, pitch angles for upward and downward electrons are 150-180 deg and0-30 deg, respectively (Haewsantati et al., 2022 (submitted)).

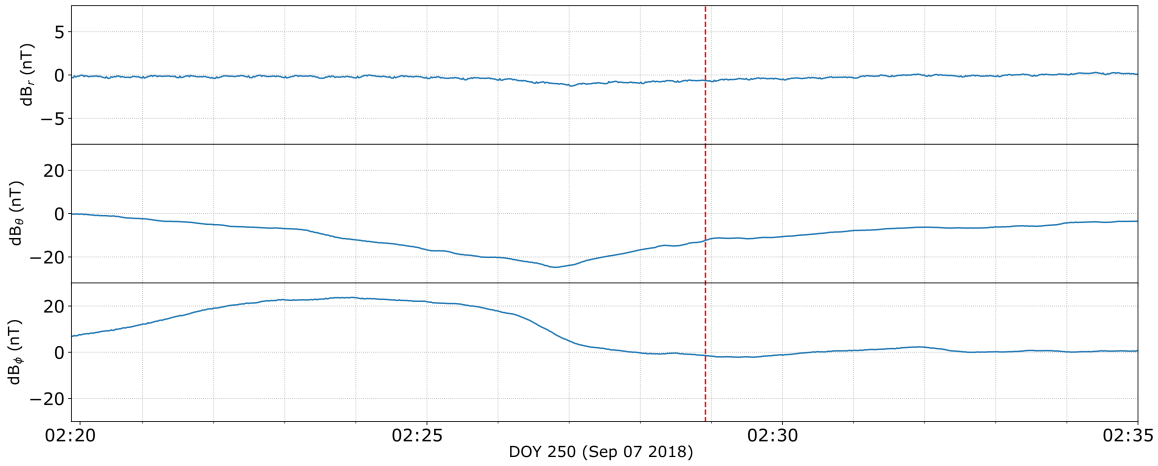

FIGURE 4.10: Magnetic field perturbation in each component during PJ15 observed by Juno MAG. Red vertical dashed line indicates the time that bright spot was detected by the UVS (Haewsantati et al., 2022 (submitted)).

4.4 PJ33 Results

For the last case, a southern spot was found during PJ33. A polar projection showing bright spot positions and the color ratio are shown in Figure 4.11. The bright spot was located at latitude 83.5°S and longitude 59.5°W (SIII) with the power of $\sim$ 10 GW. As seen in Figure 4.12, Waves observation data show intensifications of Whistler-mode waves above the proton cyclotron frequency (black lines). These intensifications occur at time before the bright spot detection, i.e., at around 01:33-01:37 UT. Unfortunately, due to the lack of burst waveforms during this observation period, the Poynting flux direction cannot be studied. As a result, the direction of wave propagation in this event cannot be identified.

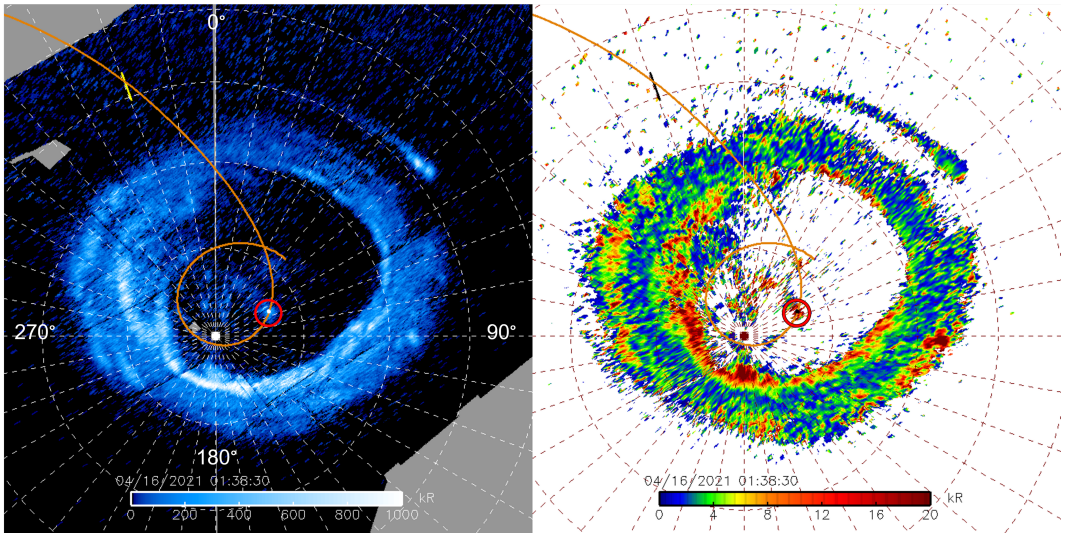

FIGURE 4.11: Polar projection shows a bright spot in (left) UV observation by UVS and (right) color ratio during PJ33. The image with the same coordinates as described in Figure 4.2 is combined from 100-spin UVS images where the bright spot appears in the last spin (Haewsantati et al., 2022 (submitted)).

Regarding JEDI observations, the particle enhancements were observed between 01:33

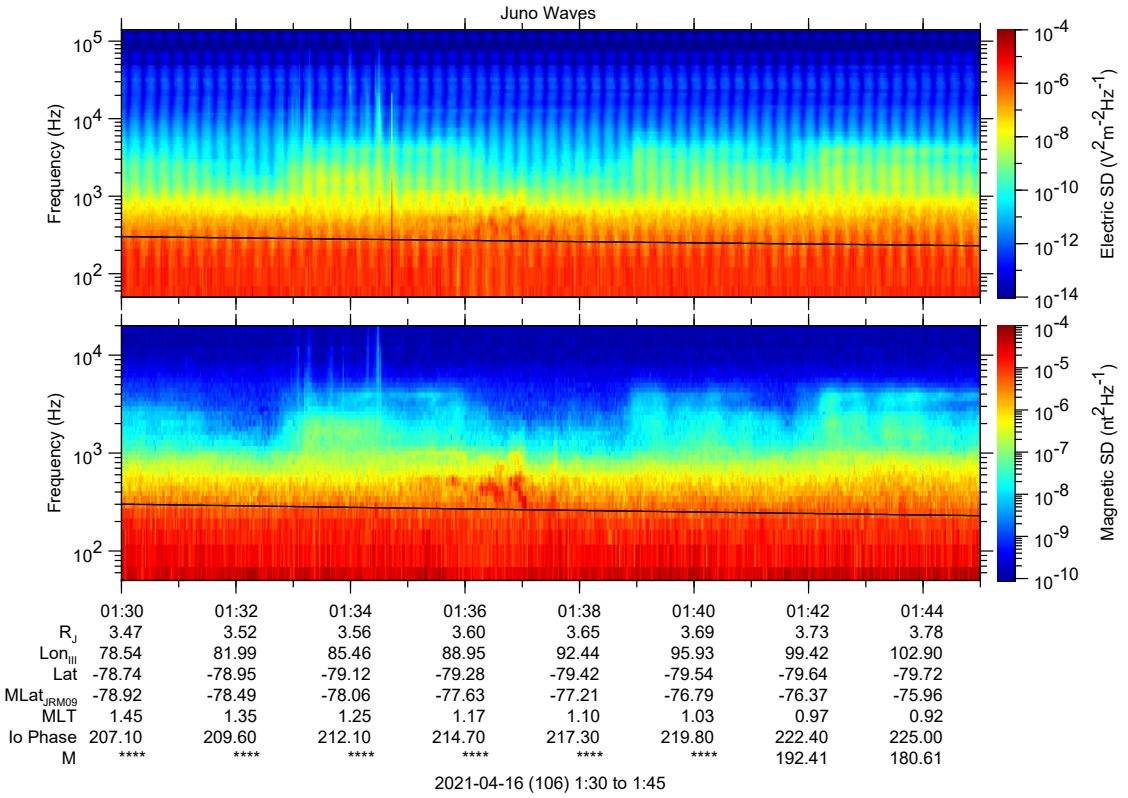

FIGURE 4.12: Frequency-time spectrogram of (top) electric field spectral density and (bottom) magnetic field spectral density observed by the Waves instruments during PJ33. Black lines represent the proton cyclotron frequencies (William Kurth, 2021, private communication).

UT to 01:35 UT, which coincided with wave intensifications. These enhancements are dominated by an upward electron beam whose energy is higher than 500 keV, as demonstrated by high intensity in panel (e) in comparison with that in panel (d). The energy flux also shows the upward electron dominance (red line above blue line in panel (f)) throughout the interval of interest. In addition, as illustrated in panels (g) and (h), JEDI detected proton enhancement at ∼01:35 UT. These high-energy protons propagate downward (with small pitch angle) before becoming low-energy protons, which then propagate in a perpendicular direction. However, after 01:35 UT, the electron energy flux decreases and remains low until after the bright spot detection time. For MAG observations, Figure 4.14, there is no significant magnetic deflection observed during waves intensification and particle enhancements and at the bright spot detection time.

4.5 Conclusions

This work presents the remote sensing and in-situ observations during three PJs at which Juno spacecraft flew close to the bright spot emissions. Table 4.1 summarizes data obtained by UVS, JEDI, Waves, and MAG instruments. The UVS data shows that the emission power of bright spots detected during PJ3 is 2-3 times higher than those observed during PJ15 and PJ33. This high emitted power in PJ3 corresponds well with the high energy electron flux observed by JEDI. However, the wave intensifications and the intense particle flux do not appear to coincide with bright spot emissions. One possible explanation for this time shift is that Juno might have not crossed the magnetic field line connecting to the bright spot when the UV power is at its peak. It is also worth noting that Juno takes some time to pass through the bright spot emissions. The crossing times for PJ3 and PJ15 is approximately 3-4 minutes, while Juno took ∼12 minutes to cross PJ33 spot. This time interval is comparable to temporal variations of bright spots discussed in the previous chapter. Therefore, the particular time of UVS bright spot detection used in this study may not be the time at the most intense bright spot emissions. Thus, this timing should be carefully considered during the interpretation of the results.

Regarding JEDI observations, all three events showed the enhancements of upward electron flux. This type of particles had been seen over the polar region previously reported by Mauk et al., 2020, although at much lower intensities. However, the auroral emission is a signature of the intense down-going particle flux. The presence of upward electron dominant and intense auroral emissions suggest that the particle acceleration process takes place at altitude between planet and spacecraft, causing particles to travel downward to the planet and upward to the magnetosphere.

In addition, the Whislter-mode wave intensifications were found during the same time with electron enhancements. For PJ3 and PJ33, wave intensifications occurred nearly the same time with the upward electron enhancements. The hypothesis of waves-particle interactions between upgoing Whistler-mode waves and upward energetic electron beam in the Jovian polar cap, as presented by Elliott et al., 2020, supports this concurrent intensification. Elliott et al., 2018b also suggested that the broadband Whistler-mode waves can accelerate the upward electrons stochastically. In case of PJ15, wave intensifications were initially observed, followed by a $\sim$ 2 minutes damping, while Juno was crossing the bright spot, and the electron enhancement was observed. This behavior is consistent with the waves-particle energy transfer process as presented by Elliott et al., 2018b. Waves were first generated near a planet or at low altitude, then propagated upward along magnetic field lines before getting damped and transferring energy to particles, before being accelerated. Since the bright spot was observed during this energy transferring time, we suggest that these waves contribute to the acceleration of particles that cause the UV emissions.

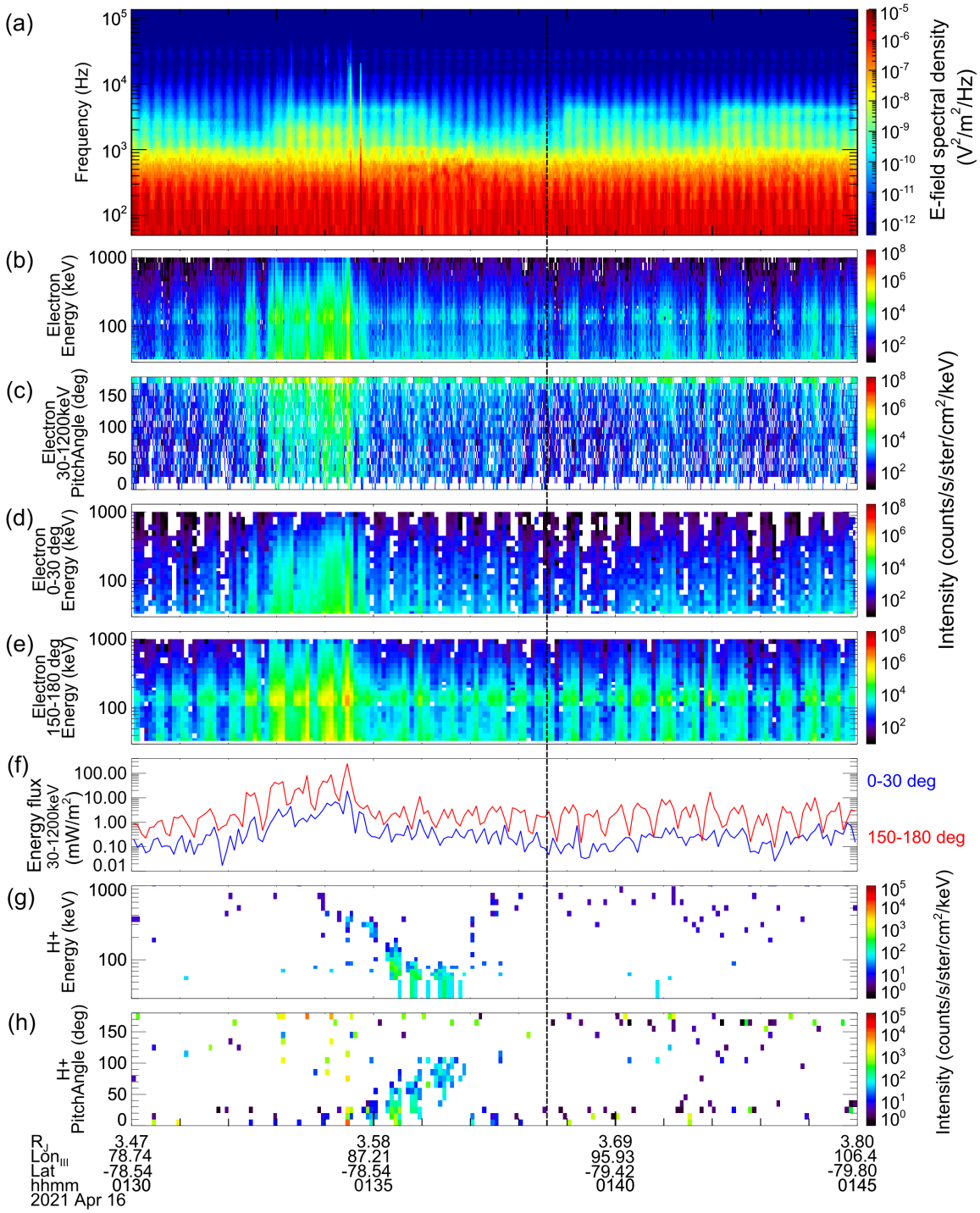

FIGURE 4.13: Electric field spectral density observed by Waves and particle distributions observed by JEDI during PJ33. Panel (a) to (f) and black vertical line are the same data types as described in Figure 4.5, while pitch angle for upward and downward electrons are described in Figure 4.9. Panel (g) and (h) represent the proton energy distributions and pitch angle distributions, respectively (Haewsantati et al., 2022 (submitted)).

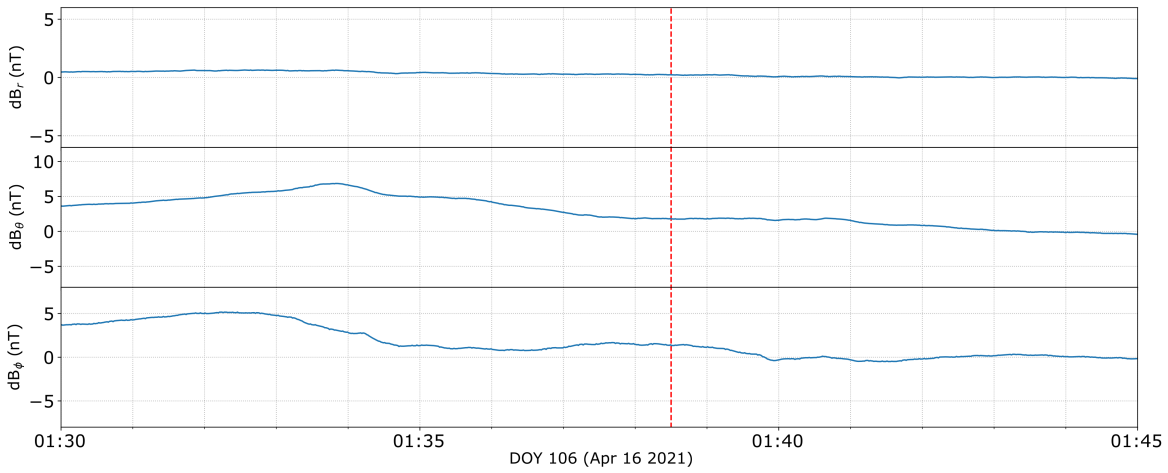

FIGURE 4.14: Magnetic field perturbation in each component during PJ33 observed by Juno MAG. Red vertical dashed line indicated the time of bright spot detection by UVS (Haewsantati et al., 2022 (submitted)).

TABLE 4.1: Summary of bright spot, waves, particles, and magnetic perturbation characteristics during bright spots, in-situ observations (Haewsantati et al., 2022 (submitted)).

		PJ3	PJ15	PJ33
Date		11-Dec-16	7-Sep-18	16-Apr-21
Juno footprint position (Lat, SIII Lon)		(63.65°, 160.20°)	(-83.04°,63.93°)	(-83.37°,65.50°)
Juno altitude (R_J)		1.8-1.7	1.5-1.6	2.58-2.69
Bright spot crossing time (UT)		15:38:26	02:28:55	01:38:30
Bright spot position (Lat, SIII Lon)		(64.38°, 159.61°)	(-82.88°, 58.19°)	(-83.51°, 59.50°)
Bright spot power (GW)		15.30	5.58	10.81
JEDI	**electron direction and enhancement time**	Upward during 15:36 UT - 15:42 UT	Upward, 2 peaks (31.9 and 37.4 at time ∼ 02:30 UT)	Upward during 01:33 UT - 01:35 UT
	maximum electron energy flux (mW/m^2)	899.82 at 15:38:47 UT	49.62 at 02:23:22 UT	860.52 at 01:34:29 UT
	electron direction[a]	Upward	Upward	Upward
	average electron energy flux[b] **(mW/m^2)**	267.24	3.1	0.22
	proton direction	upward	upward	upward then perpendicular
Waves	**Whistler-mode intensification**	15:37 UT - 15:40 UT	02:26 UT - 02:28 UT	01:33 UT - 01:37 UT
	waves direction	upgoing	upgoing	no analysis
MAG		A perturbation with small amplitude during 15:38 UT - 15:42 UT	A small deflection but less obvious	no significant deflection

[a]at bright spot crossing time
[b]during bright spot crossing (±10 s)

For the cause of the bright spot emissions in relation with the magnetospheric process, which is implied by the magnetic perturbation, the strong signatures were only detected in PJ3. These results suggest that the magnetospheric currents are not a significant contributor to bright spot emissions. Indeed, the strong magnetic deflection recorded in PJ3 is most probably due to the field-aligned currents on (or very close to) the flux tubes, which Juno passes through.

The upgoing particles were observed not only by JEDI, but also by UVS measurement. Figure 4.15 shows the noise count rates caused by the penetrating of >7 MeV electrons through the instrument's shielding (Zhu et al., 2021) during Juno flyby over a bright spot. Blue vertical lines indicate times when UVS' view was aligned with the magnetic field, which pointed away from Jupiter for PJ3 and toward Jupiter for PJ15 and PJ33. The count rates for PJ15 peaked at the blue lines or when UVS pointed toward Jupiter, Bonfond et al., 2018 named this pattern as the barcode events. The count rate pattern for PJ15 is similar to those of PJ33, but the signals are much weaker. For PJ3, count rates are highest between two blue lines. However, there are several data gaps in this event, including at blue lines that lead to ambiguous penetrating electron directions. In general, the times when count rate peaks for all three events correspond to the times of JEDI electron enhancements. A possible explanation is that this count rate is the high energy tail of the particles related to the upward electron and upgoing whistler-mode waves interaction, as discussed by Elliott et al., 2018a.

According to the results, there might be a time delay between the UVS remote sensing observations and in-situ observations, resulting in the time differences between wave-particle enhancements and bright spot detection time. The following are some of the possibilities that have been proposed. Firstly, considering that Juno was crossing the magnetic field line connected to bright spot emissions, the waves and particles should have been detected before they took time to travel from the spacecraft to the bright spot position beneath the spacecraft. Assuming that 100 keV electron and 100 keV proton are at distance 1.5 R_J (distance from the spacecraft to bright spot position), the travel times are 0.6 s and 25 s, respectively. The time travel for waves is even shorter. For comparison, the 30 s spacecraft spin period is even longer than proton travel time. In addition, the particle traveling time should be less than the calculation above if the precipitating particles that create bright spot emissions come from the acceleration region at position between the planet and spacecraft. Therefore, time differences should not be caused by the travel times of waves and particles. Secondly, the bright spot's emission power varies with time, and the UVS image might record the emission at different intensity or to different extent. As a result, this uncertainty should affect the mismatch intensity rather than a time difference. Finally, the mapping uncertainty is due to the JRM09 magnetic field model's accuracy (i.e., a time shift presented by Allegrini et al., 2020). This should be the most appropriate cause for the time delay.

In conclusion, bright spot emissions appear to be independent of field-aligned currents, as no strong magnetic perturbations were seen in PJ15 and PJ33. According to previous analysis, the bright spot is fixed in SIII, suggesting that the responsible process occurs closer to the planet. As a result, the waves-particle interaction, as evidenced by intensifications of Whistler-mode waves and upward electron enhancements, appears to be the most potential explanation for particle acceleration which leads to the UV bright spot emissions. However, there are two additional possibilities for particle accelerations that should be considered. The first scenario is the acceleration of high-energy electron beams by magnetic reconnection near Jupiter's polar magnetosphere (Masters et al., 2021), and the second scenario is the broadband acceleration due to the presence of an ionospheric Alfvén resonator or IAR Lysak et al., 2021. Furthermore, more research in magnetohydrodynamic simulations of the Jovian magnetosphere and the tangling of the magnetic flux tubes above the poles (e.g., Zhang et al., 2021) might help us understand the underlying cause of these bright spot emissions.

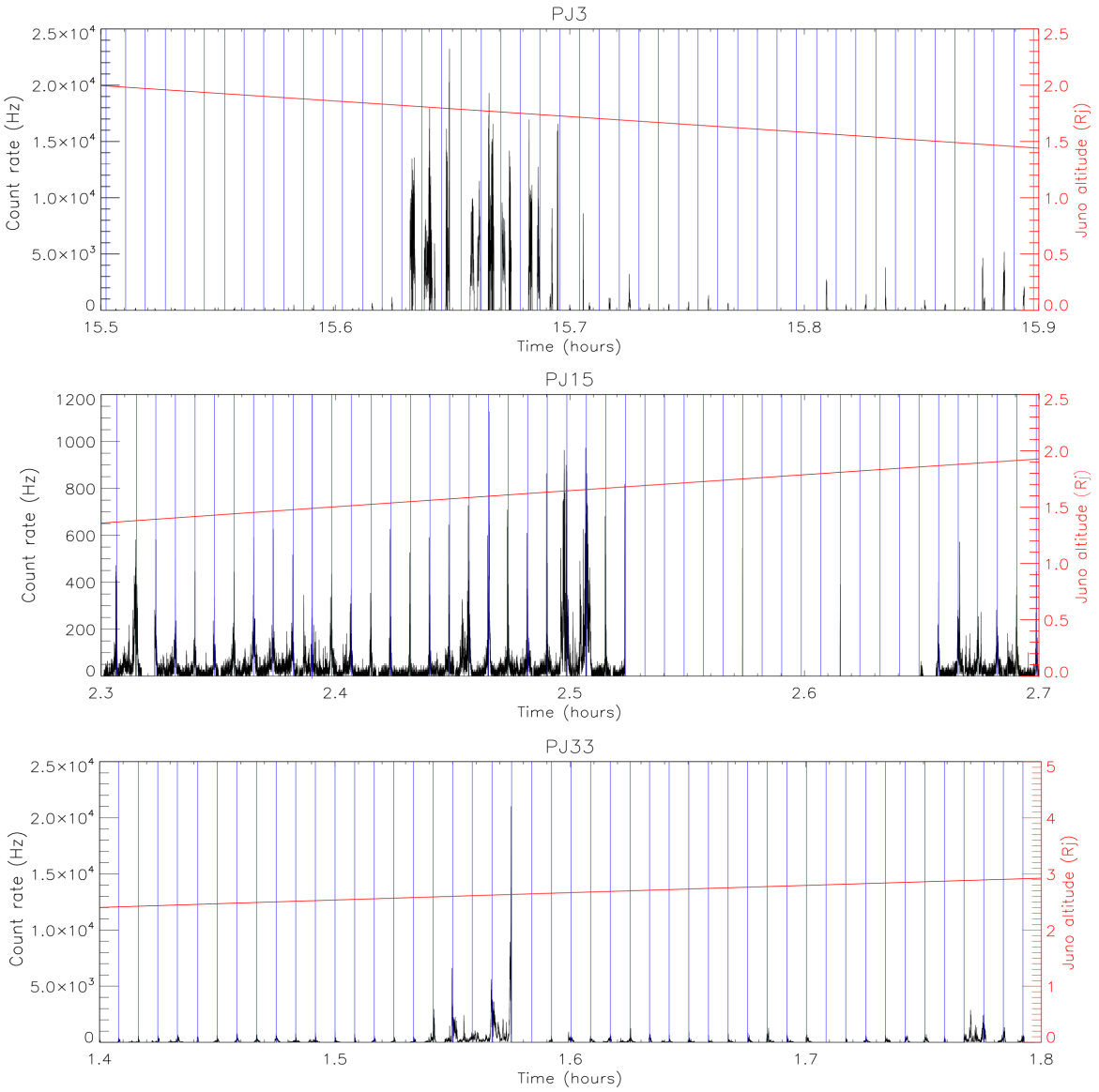

FIGURE 4.15: Measurement of Juno-UVS for penetrating particle count rates during (top) PJ3, (middle) PJ15, and (bottom) PJ33. The data gap is referred to as the zero-count rate. Vertical blue lines show the times when Juno-UVS aligned with the magnetic field lines at the smallest angle. The red line represents the progression of Juno's altitude (Haewsantati et al., 2022 (submitted)).

Additional flyby events above the bright spot through or below the acceleration region, as well as sampling of downward particles, might provide a better understanding of the bright spot emission dynamics.

Chapter 5

Summary and Future Work

Jupiter's polar auroral bright spot is one of the interesting features which occasionally appear in Jupiter's polar aurorae (e.g., Pallier and Prangé, 2001; Bunce, Cowley, and Yeoman, 2004). In these previous studies based on HST images, the bright spots were found at high latitude equatorward of the northern polar cap boundary which remains close to magnetic noon, which suggested a possible link to the magnetospheric cusp and thus to open field lines connecting to the solar wind. However, Earth-based observations are both incomplete (only the dayside can be seen) and biased (the dipole tilt favors some CML sectors compared to others). With the new era of Jupiter observations made by instruments onboard Juno spacecraft, the bright spot observations reveal many surprising results which are very useful for better understanding of Jupiter's polar aurorae. The characteristics of the bright spot emissions (positions and their variabilities) observed by UVS, which are a complete and unbiased view offered by Juno, are provided in the first study (Chapter 3). The second study (Chapter 4) relies on three unprecedented events (PJ3, PJ15, and PJ33) during which Juno flew through the field line connected to (or close to) the auroral bright spot. This study we used the complete instrumental package of Juno to study the magnetic field, waves, and particle signatures related to these auroral features.

5.1 Summary

The characteristics of bright spot emissions studied from UV spectral images taken by Juno-UVS reveal that the bright spot emissions are regularly found in both the northern and the southern hemispheres. One significant result is that the bright spot seems to be located at the edge of the swirl region, where a high color ratio is usually found (Bonfond et al., 2017; Greathouse et al., 2021)). This high color ratio implies highly energetic particles penetrating planetary atmosphere (Gustin et al., 2004). In addition, at the greater depths, the H_2 emissions can be absorbed by the methane layer in Jupiter's atmosphere leading to the increasing in high color ratio as well (Yung et al., 1982). Moreover, we found that bright spot at all magnetic local time ranges. Previous study based on Earth-based observations showed that the bright spot was usually detected near the noon magnetic local time (Pallier and Prangé, 2001). The bright spot was therefore suggested to be associated with noon magnetospheric cusp according to the interpretation of the Earth-like cusp process. However, this work even found bright spots during the night time. The recurrences of bright spots are also fixed in SIII as Jupiter rotates, which is incompatible with the fixed magnetic local time for the Earth-like cusp process. On one hand, the ionospheric positions and local times results suggested that this feature might not be a signature of the noon magnetospheric cusp process since the bright spot can be found in various local time ranges; late evening through midnight to late morning for northern spots and all local time ranged for southern spots. On the other hand, the bright spot's connection with the noon magnetospheric cusp process is still possible if Jupiter's magnetospheric cusp is unusual according to simulations from

Zhang et al., 2021. The simulations indicate that the cusp at Jupiter is not like the cusp at Earth. The fast rotation of the planet relative to its size makes the polar-most field lines twisted and entangled, with regions of open and closed field lines mixed with each other. Hence, it is no longer clear what the cusp topology really is and what the possibly related auroral emissions would look like. This is the reason why we cannot formally exclude the idea that the bright spots could somehow be related to cusp-like processes, even if the fixity in SIII of the recurring bright spots. The most crucial result is that the bright spot can reappear nearly at the same position. In comparison, aurorae in both hemispheres were observed by Juno for 4-5 hours, which is half of Jupiter's rotation period. The reoccurring of this feature within a given perijove implies that the plasma source related to the bright spot emissions is corotating with Jupiter rather than fixed in a position in the magnetosphere.

Moreover, this emission is not a sporadic but periodic emission. The 22-28 minutes periods can be analyzed from PJ4 and PJ16 data during their 3-4 hours observing times. It is impossible to demonstrate such a periodicity with HST data, since the observation times are only $\sim$45-minute long. In addition, the 3-47 minutes time interval between two consecutive brightenings is quite similar to other quasi-periodic pulsations. For example, the 15- and 40-minute QP radio bursts (MacDowall et al., 1993), the 40-minute periodicity in relativistic electron bursts observed by Ulysses (McKibben, Simpson, and Zhang, 1993), Alfvén waves process (Manners, Masters, and Yates, 2018) and X-ray pulsations (e.g., Gladstone et al., 2002; Elsner et al., 2005; Jackman et al., 2018; Wibisono et al., 2020). Even though UV and radio emissions are associated with electrons, while the X-ray emissions are dominated by the emissions from energetic heavy ions, a similar period range between these QP emissions were reported. For example, the 45-minute period of emissions from X-ray hot spot region (Gladstone et al., 2002) corresponded to the high latitude radio and energetic electron bursts (MacDowall et al., 1993). Bunce, Cowley, and Yeoman, 2004 also suggested that the pulsed reconnection on the dayside magnetopause could be the source of both X-ray and UV pulsations. As shown in Chapter 4 result, the positions of northern bright spots are at the same region of X-ray hot spot and their periods are in the same range, the QP in X-ray and UV bright spots might be caused or triggered by the same process. For example, the standing Alfvén waves which was suggested to be the responsible process for the 10-60 minutes QP ultralow frequency pulsations (Manners, Masters, and Yates, 2018).

The possible process related to the bright spot emission can be investigated from the behavior of particles, currents, and waves, observed by JEDI, Waves, and MAG during the spacecraft crossing of the magnetic field line connected to bright spot emission. We investigated the flyby events from all orbits up to PJ34. Three events are identified and presented in the work. From all three events, the upward electrons are dominating during the times of the bright spot detection. These particles are not responsible for the auroral emissions, but their detections suggested that the spacecraft was above the particle acceleration region, where the downgoing particles travel toward the atmosphere and cause the auroral emissions. The upgoing Whistler-mode waves are also found, while the signatures of magnetic field-aligned currents interpreted from the magnetic deflection are very weak. The wave intensifications and electron enhancements can be seen at the same time of the bright spot detection (PJ3 spot), before the bright spot detection (PJ33 spot), or prior and after the bright spot detection (PJ15 spot). The time mismatch between the times of bright spot detection and the wave-particle intensification might partly be due to the uncertainty of the JRM09 magnetic mapping model. We suggested here two caveats of the magnetic field mapping which might result in the time shift between UV emissions and the particle enhancements. Firstly, the actual spot crossing might not have happened at the time when we consider that Juno was crossing the magnetic field line connecting to bright spot emission, but we consider the flyby happens since we consider bright spot ang Juno positions from the JRM09 mapping. Secondly, the spacecraft crossing did not take place in the middle of the spot.

This time shift was presented before by Allegrini et al., 2020 for the ∼90 s shift between UV brightness of Europa's tail and electron energy flux. The usage of JRM33 might reduce the uncertainty resulting in the time delay.

According to the results, the intensifications of upgoing Whistler-mode waves and upward electron enhancements occurred during the same time (PJ3 and PJ33). This concurrence suggests the wave-particle interactions take place as suggested by Elliott et al., 2020. The sequence of wave intensification followed by the particle enhancement found in PJ15 is consistent with the wave-particle energy transfer process as presented by Elliott et al., 2018b. The detections of bright spot emissions during these interactions suggest that waves-particle interactions contribute to the particle acceleration that causes the bright spot emissions. However, we have to note that the signatures of field-aligned currents are found only in PJ3 and the wave damping only found in PJ15. The exact mechanism for describing all three bright spot emissions is still puzzling. In addition, the particles causing the emissions might be accelerated by other mechanisms in Jupiter's upper atmosphere as well. Two tentative mechanisms proposed here are the magnetic reconnection near Jupiter's polar magnetosphere due to large-scale Alfvénic disturbances (Masters et al., 2021) and the broadband acceleration due to the presence of an ionospheric Alfvén resonator or IAR (Lysak et al., 2021).

5.2 Future work

From the results, the characteristics of the bright spot emissions sufficiently provide the understanding of the bright spot dynamics and morphology. However, the explanations of responsible causes are still remaining. Potential future studies to solve the remaining puzzles are listed as follows.

1. Until now, the bright spot's characteristics are analyzed from the first 25 perijoves, the remaining Juno observations could provide more information which will definitely be helpful for understanding the bright spot emissions, for example, the bright spot emissions found during PJ33. In addition, even though the HST observations are biased due to the Earth-based view which allows us to see the bright spot only at the dayside, the time-tag observation mode of HST might be able to reveal the bright spot variation in detail, with a shorter time scale.

2. The role of the magnetospheric cusp on the bright spot emissions might be solved by the magnetohydrodynamic simulations of the Jovian magnetosphere with the understanding of tangling magnetic flux tubes above the poles, i.e. the model presented by Zhang et al., 2021.

3. In-depth theoretical study on the following three candidate processes, i.e. waves-particles interaction (Elliott et al., 2020), magnetic reconnection near pole (Masters et al., 2021), and the Alfvénic resonance (Lysak et al., 2021), could reveal the actual particle acceleration process that causes the auroral bright spot. The study should collaborate with the flyby observations. Therefore, additional flyby events are very important to provide more evidence to support one of those proposals. In particular, the sampling of downward particles during the observations above the bright spot emissions, through or below the acceleration region, should be done in later orbits during the extended mission after the prime Juno mission. An additional Juno flyby above bright spot emission was recently found during PJ42 in the southern hemisphere observed on May 22nd, 2022. Further results from this event could reveal more information to better conclude the cause of bright spot emissions.

Appendix A

Identified Bright Spots

This section shows the polar projection of the identified bright spots found in each perijove. The image for each bright spot represents the time of bright spot emission whose brightness is brightest in comparison with other images in the same bright spot set.

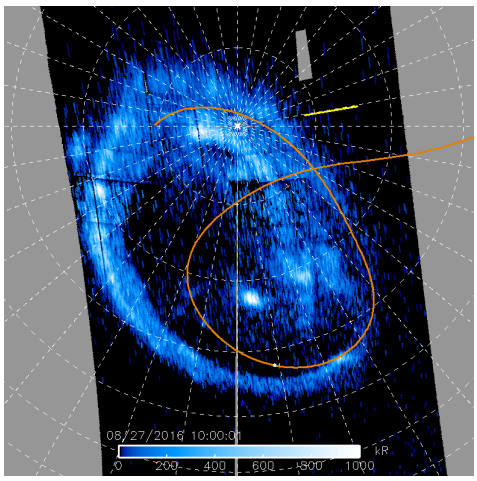

(A) Bright spot during PJ1

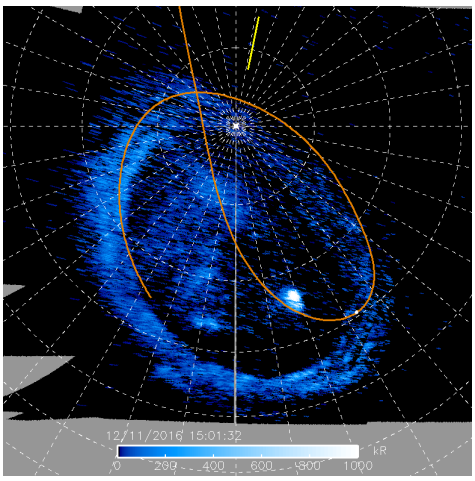

(B) Bright spot during PJ3, spot 1

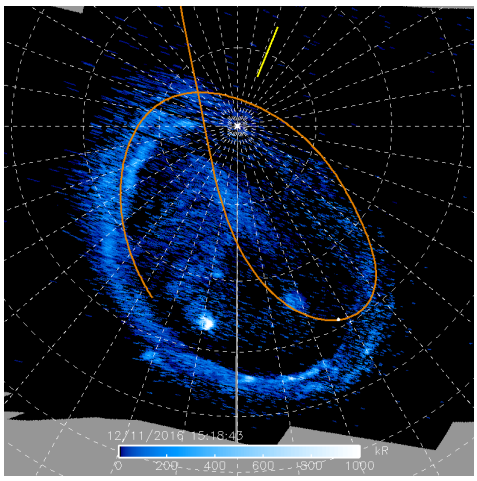

(C) Bright spot during PJ3, spot 2

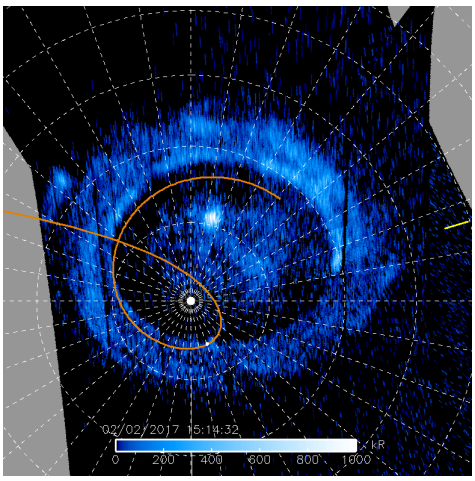

(D) Bright spot during PJ4

FIGURE A.1: Bright spots found in each perijove

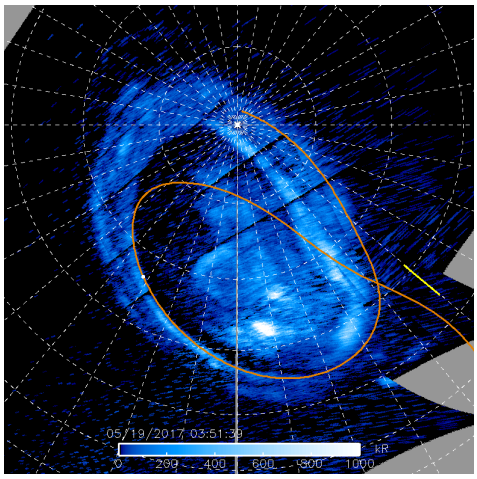

(E) Bright spot during PJ6

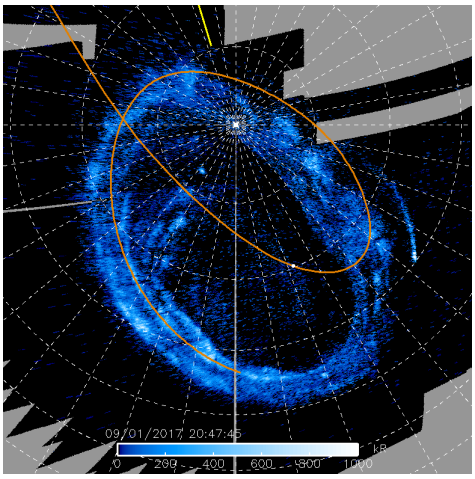

(F) Bright spot during PJ8, north

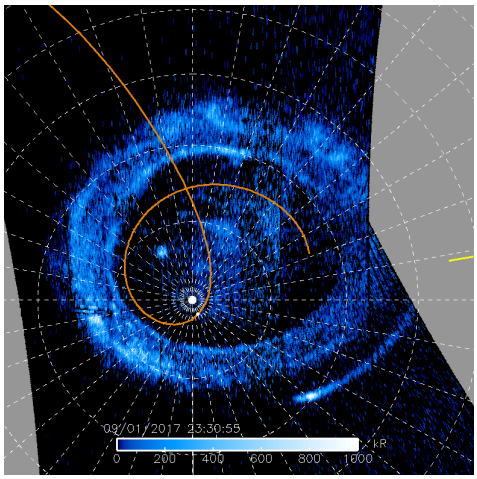

(G) Bright spot during PJ8, south

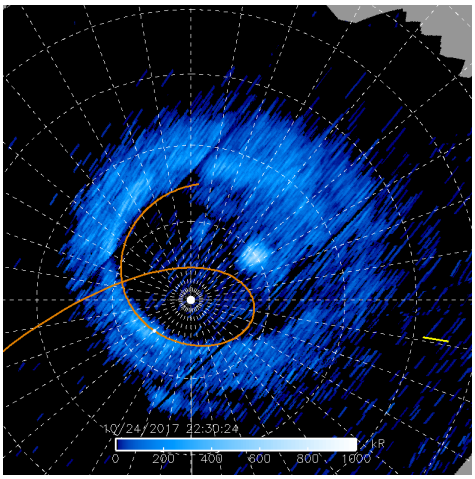

(H) Bright spot during PJ9

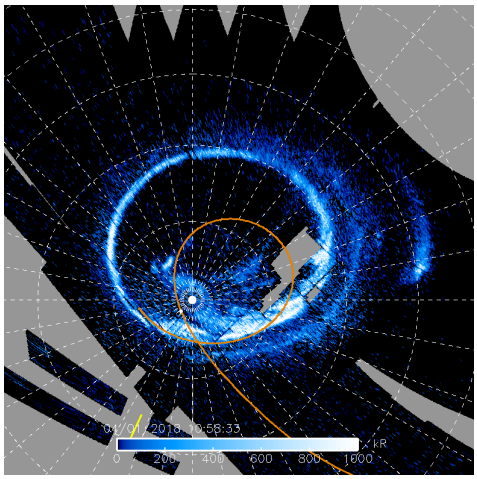

(I) Bright spot during PJ12, spot 1

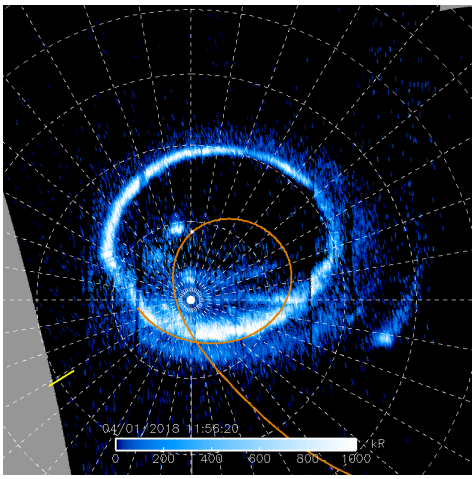

(J) Bright spot during PJ12, spot 2

FIGURE A.1: Bright spots found in each perijove (continued)

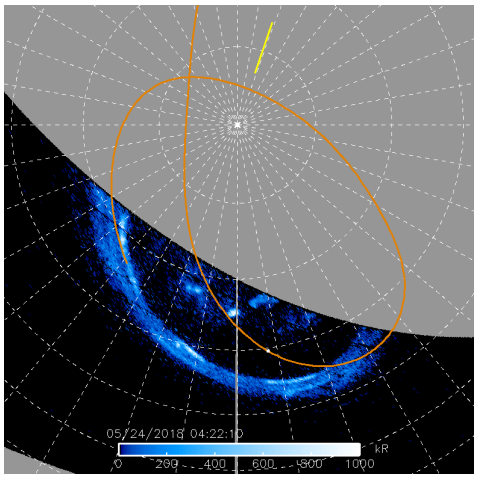

(K) Bright spot during PJ13

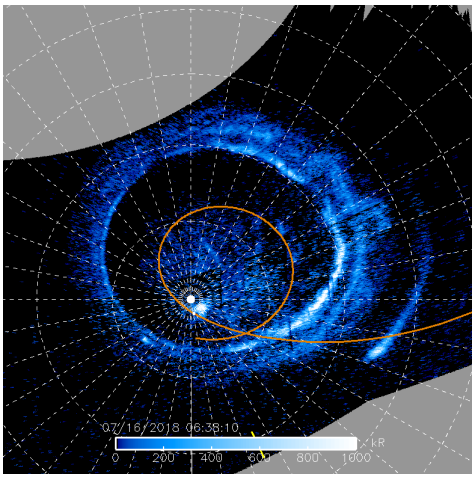

(L) Bright spot during PJ14

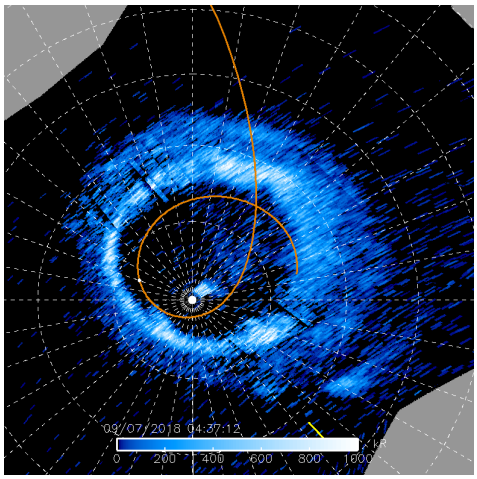

(M) Bright spot during PJ15

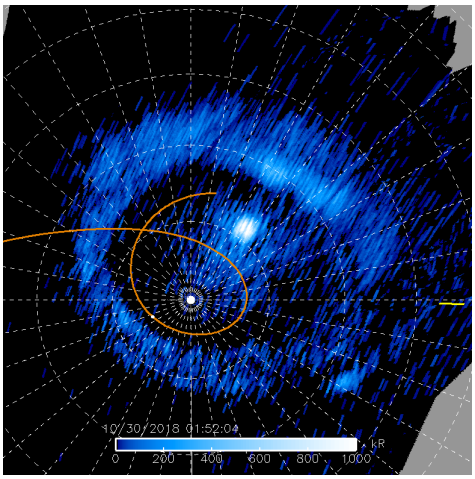

(N) Bright spot during PJ16

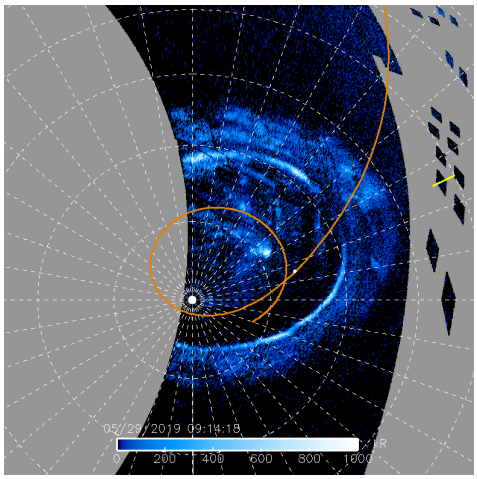

(O) Bright spot during PJ20

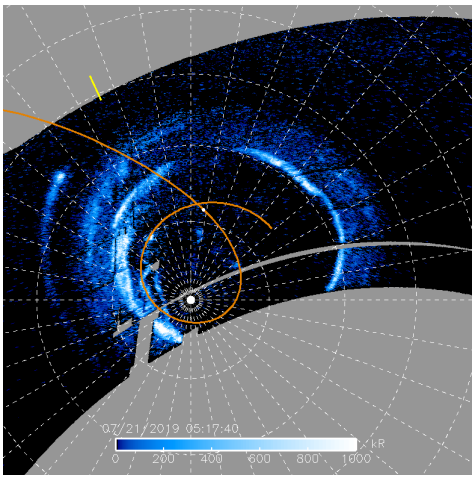

(P) Bright spot during PJ21, spot 1

FIGURE A.1: Bright spots found in each perijove (continued)

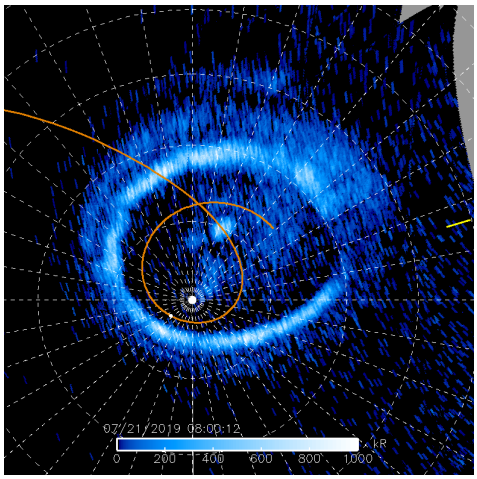

(Q) Bright spot during PJ21, spot 2

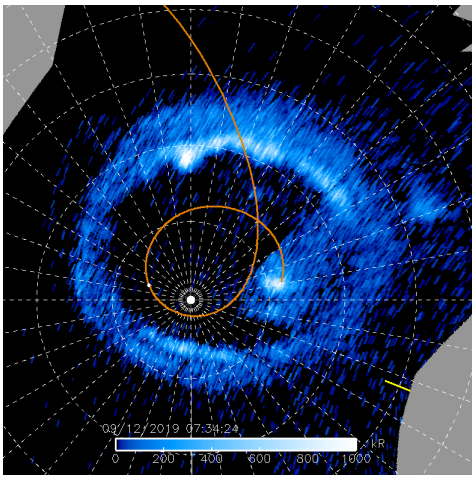

(R) Bright spot during PJ22

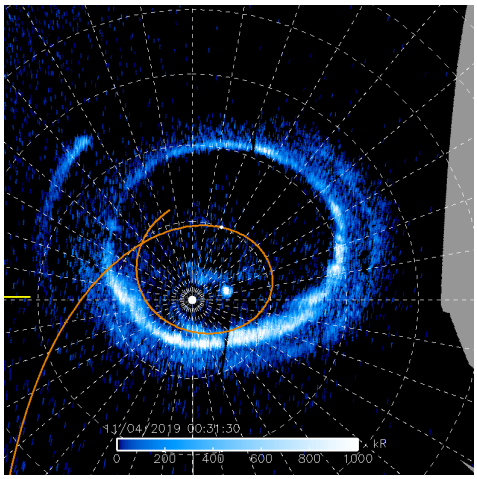

(S) Bright spot during PJ23, spot 1

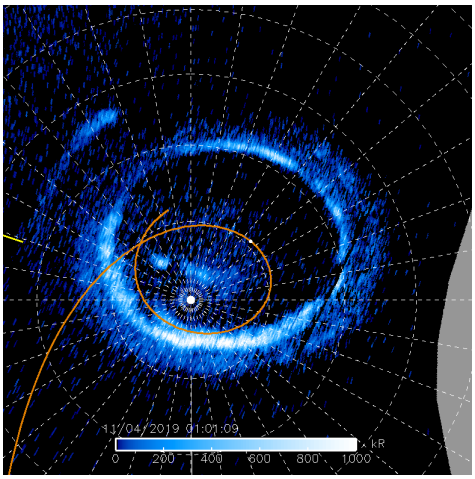

(T) Bright spot during PJ23, spot 2

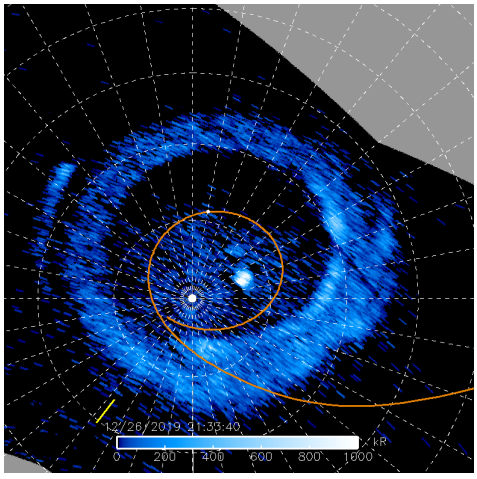

(U) Bright spot during PJ24

FIGURE A.1: Bright spots found in each perijove (continued)

Appendix B

Table of bright spot list

The bright spot characteristics observed during PJ1 to PJ25 according to Chapter 3 study are presented in Table B.1. The UT time corresponds to the UVS observing time. The bright spot position in latitude and SIII longitude ('Lat.' and 'SIII Lon.' in table) is presented by the position of the peak pixel. The minus sign in latitude column represents the position of bright spot in southern hemisphere. The power is the total brightness in bright spot's surface area. Noted that this power is calculated from a bright spot area, while the power variation plot shown in Figure 3.8 and Figure 3.9) are the union ellipse fit according to all bright spots detected during PJ4 and PJ16, respectively. Two values in bracket are the minimum and maximum power according to the 25% smaller and greater uncertainties. The magnetic flux are computed the total magnetic flux in the surface area. The ionospheric local time is calculate by using the peak position, given in hour. The last two columns present the position (in R_J) and local time (in hour) in magnetosphere of the bright spot peak's position according to Vogt's magnetic flux equivalent by using JRM09 as the internal model.

TABLE B.1: Bright spot characteristics according to Chapter 3 study (Haewsantati et al., 2021).

PJ	Date	Time	Peak's position		Power	Surface area	Magnetic flux	ionospheric	Vogt's mapping result	
		(UT)	Lat.	SIII Lon.	(GW)	($\times 10^6$ km^2)	($\times 10^9$ Wb)	local time	Position	Local time
PJ1	8/27/2016	10:00:01	67.3	175.6	103 (98, 107)	9.16	5580	7.12	143.4	2.84
PJ1	8/27/2016	10:15:53	67.8	175.5	69 (66, 71)	10.48	6429	7.87	141.8	3.42
PJ1	8/27/2016	10:19:28	66.8	174.8	56 (51, 59)	8	4824	7.97	141.5	3.70
PJ3	12/11/2016	14:56:59	65.7	164	39 (37, 41)	4.1	2882	3.84	149.3	1.22
PJ3	12/11/2016	15:01:32	67	161.5	88 (85, 90)	9.64	6840	4.59	146.3	2.29
PJ3	12/11/2016	15:13:10	66.1	161	79 (73, 82)	8.13	5817	4.94	149.5	2.42
PJ3	12/11/2016	15:21:15	65.5	162.4	24 (22, 25)	2.97	2113	4.98	148	2.27
PJ3	12/11/2016	15:42:27	64.3	159	82 (76, 85)	7.68	5722	6.04	143.5	3.34
PJ3	12/11/2016	16:12:17	63.9	158.5	14 (13, 15)	1.36	1055	7.24	135.9	4.46
PJ3	12/11/2016	14:45:21	64	189.3	26 (24, 28)	5.84	2799	23.03	131.5	20.70
PJ3	12/11/2016	15:18:43	63.9	188.2	56 (52, 59)	5.05	2409	0.58	144.1	21.87
PJ3	12/11/2016	15:52:34	64.3	189.2	22 (19, 23)	1.22	580	1.75	147	22.85
PJ4	2/2/2017	14:18:13	-78.6	14	22 (19, 23)	1.75	1927	12.7	92.1	14.42
PJ4	2/2/2017	14:46:10	-78.9	12	54 (51, 56)	5.38	5852	13.96	99.9	15.92
PJ4	2/2/2017	15:14:32	-79.1	13.4	90 (83, 94)	9.21	10245	14.95	107.7	16.97
PJ4	2/2/2017	16:12:25	-80.2	13.6	51 (46, 54)	5.62	6280	17.1	148.9	19.07
PJ4	2/2/2017	16:40:22	-79	12.1	31 (29, 32)	7.85	8759	18.54	149.4	19.85
PJ4	2/2/2017	17:33:40	-79.9	10.5	30 (28, 31)	8.18	9180	20.7	147.4	20.90
PJ6	5/19/2017	3:51:39	62.1	170.8	94 (83, 102)	6.63	4229	10.53	102.8	8.04
PJ6	5/19/2017	3:52:40	62.3	171.3	72 (65, 78)	6.52	4253	10.52	101.1	8.13
PJ6	5/19/2017	3:54:11	62.1	171.2	82 (74, 88)	10.25	6869	10.58	99.3	8.23
PJ6	5/19/2017	4:08:49	62.2	177.4	70 (60, 77)	7.53	4405	10.26	148.6	5.13
PJ6	5/19/2017	4:22:26	62.5	173.5	61 (57, 64)	8.08	5242	11.41	89.5	9.26
PJ8	9/1/2017	20:47:45	82.7	216.5	3 (2, 3)	0.45	321	11.97	73.6	11.27
PJ8	9/1/2017	22:42:39	-83.1	329.5	3 (3, 3)	0.35	423	18.41	150	20.38
PJ8	9/1/2017	23:17:50	-82.8	327.2	2 (2, 2)	0.46	561	20.07	149.5	21.12
PJ8	9/1/2017	23:30:55	-82.9	326.5	10 (9, 11)	1.58	1904	20.73	148.3	21.56

Continue on the next page

Table B.1 – Continuation of Table B.1

PJ	Date	Time (UT)	Peak's position		Power (GW)	Surface area ($\times 10^6$ km^2)	Mafnetic flux ($\times 10^9$ Wb)	ionospheric local time	Vogt's mapping result	
			Lat.	SIII Lon.					Position	Local time
PJ8	9/1/2017	23:46:30	-82.8	332.1	10 (9, 11)	1.72	2077	20.54	149.8	21.53
PJ8	9/1/2017	23:56:04	-82.4	329.5	8 (7, 9)	1.78	2152	21.21	148.1	21.66
PJ9	10/24/2017	20:58:31	-76.3	47.5	35 (30, 38)	4.38	5103	10.6	91	10.02
PJ9	10/24/2017	21:11:08	-77.6	47.3	49 (44, 52)	9.47	11144	11	92.4	10.45
PJ9	10/24/2017	21:13:09	-77.1	48.9	30 (26, 33)	5.56	6565	11.02	91.7	10.56
PJ9	10/24/2017	21:25:47	-77.3	48.9	110 (102, 116)	14.3	16969	11.51	92.3	11.05
PJ9	10/24/2017	21:32:21	-78.4	48.5	35 (30, 37)	4.49	5383	11.68	89.6	11.21
PJ9	10/24/2017	21:53:33	-78.9	44.4	49 (43, 53)	7.52	9097	12.75	89.8	12.85
PJ9	10/24/2017	22:29:23	-79.9	58	98 (91, 102)	13.74	17469	13.18	88.6	12.09
PJ9	10/24/2017	22:30:54	-80.6	62.2	146 (136, 154)	20.7	26726	12.87	86.5	11.34
PJ12	4/1/2018	10:59:35	-83.4	312.2	25 (22, 26)	1.88	2292	6.9	137.4	4.35
PJ12	4/1/2018	11:20:34	-84.3	317.2	13 (11, 14)	1.33	1703	7.8	122.9	5.83
PJ12	4/1/2018	11:13:24	-81.2	349	7 (7, 8)	0.99	1120	2.44	79.5	2.49
PJ12	4/1/2018	11:18:31	-80.1	345.2	9 (8, 10)	1.57	1736	3.15	147.4	1.71
PJ12	4/1/2018	11:54:48	-79.7	348.8	14 (12, 14)	2.56	2768	4.24	132.9	2.80
PJ12	4/1/2018	11:56:20	-80.7	349.1	41 (39, 43)	3.89	4400	4.2	123.6	2.87
PJ13	5/24/2018	4:22:10	65.2	181.3	19 (18, 21)	1.51	846	1.63	136.4	23.02
PJ13	5/24/2018	4:47:31	65.8	182.6	17 (15, 19)	1.55	868	2.42	136.2	23.63
PJ14	7/16/2018	6:31:39	-87.9	136.5	20 (18, 21)	2.22	3252	11.97	97.5	8.23
PJ14	7/16/2018	6:33:39	-87.9	139.4	31 (26, 34)	2.88	4194	11.98	99.6	7.97
PJ14	7/16/2018	6:38:10	-87.9	127.7	29 (25, 31)	2.29	3338	12.43	93.2	8.77
PJ14	7/16/2018	6:55:12	-87.8	149	9 (7, 10)	1.03	1473	12.64	92.1	9.16
PJ14	7/16/2018	7:01:43	-87.8	157.1	15 (13, 16)	1.37	1958	12.71	86.6	9.60
PJ15	9/7/2018	2:28:55	-82.9	58.2	6 (6, 7)	0.72	990	12.71	115.9	6.33
PJ15	9/7/2018	3:02:29	-84.1	56.1	4 (4, 4)	1.29	1764	11	94.5	8.19
PJ15	9/7/2018	4:33:42	-86.7	48.8	14 (12, 15)	3.33	4670	13.43	90.6	10.33
PJ15	9/7/2018	4:37:12	-88.3	32.3	44 (40, 45)	4.96	7212	12.09	93	8.40
PJ16	10/29/2018	23:00:33	-78.8	24.8	52 (49, 54)	3.71	4241	8.24	149	4.95

Continue on the next page

Table B.1 – Continuation of Table B.1

PJ	Date	Time (UT)	Peak's position		Power (GW)	Surface area ($\times 10^6$ km^2)	Mafnetic flux ($\times 10^9$ Wb)	ionospheric local time	Vogt's mapping result	
			Lat.	SIII Lon.					Position	Local time
PJ16	10/29/2018	23:29:09	-78.7	30.2	32 (30, 32)	4.65	5312	8.98	97.1	8.13
PJ16	10/29/2018	23:56:15	-77.8	36	19 (16, 20)	3.27	3759	9.75	94.5	9.40
PJ16	10/30/2018	0:26:21	-77.6	36.2	41 (37, 44)	5.93	6750	10.98	87	11.29
PJ16	10/30/2018	0:48:26	-78	38.8	32 (29, 34)	6.18	7216	11.64	90.5	12.01
PJ16	10/30/2018	1:29:05	-78.6	39	82 (76, 86)	9.85	11463	13.18	91.2	13.26
PJ16	10/30/2018	1:52:04	-78.2	38.7	158 (144, 166)	12.77	15025	14.19	94.1	14.99
PJ20	5/29/2019	9:08:12	-78.5	56.7	13 (12, 14)	1.65	2089	10.93	94.2	9.5
PJ20	5/29/2019	9:11:46	-78.7	57	9 (8, 10)	0.71	899	11.03	92.2	9.62
PJ20	5/29/2019	9:14:18	-78.6	57.7	19 (16, 21)	1.71	2147	11.1	90.1	9.67
PJ20	5/29/2019	9:49:22	-79.4	55.6	3 (3, 4)	0.98	1221	12.55	88.5	11.60
PJ21	7/21/2019	5:17:40	-80.4	328.1	7 (6, 8)	0.64	719	13.06	96.7	15.62
PJ21	7/21/2019	6:59:00	-82.3	2.9	24 (23, 25)	4.43	5439	12.85	92.3	14.36
PJ21	7/21/2019	7:46:09	-82.1	1.7	64 (61, 66)	7.73	9279	14.95	107.4	17.09
PJ21	7/21/2019	8:00:12	-80.3	20.3	69 (65, 72)	9.04	10554	14.16	97.7	15.67
PJ22	9/12/2019	7:34:24	-78.5	80.4	145 (132, 154)	17.42	22926	12.95	89.8	10.55
PJ22	9/12/2019	7:50:56	-79.6	84.5	125 (113, 134)	14.87	19932	13.28	89.6	10.64
PJ23	11/4/2019	0:31:30	-85.4	76.7	33 (31, 34)	2.36	3321	22.44	132.3	18.70
PJ23	11/4/2019	1:06:41	-86.4	81.3	26 (23, 27)	2.01	2925	23.27	136.2	19.30
PJ23	11/4/2019	1:01:09	-83.9	320.1	24 (23, 25)	4.26	5294	11.93	91.2	13.13
PJ24	12/26/2019	19:20:32	-82.6	20.5	20 (18, 21)	2.04	2560	17.73	148.1	19.02
PJ24	12/26/2019	20:00:32	-81.2	26.3	80 (78, 80)	6.8	8311	19.29	149.4	19.77
PJ24	12/26/2019	20:44:34	-81.7	40.9	18 (15, 19)	2.7	3415	19.88	149.6	19.05
PJ24	12/26/2019	20:49:38	-81.9	62.5	21 (20, 22)	5.39	7294	19.88	115.4	17.42
PJ24	12/26/2019	21:33:40	-83.6	71.8	86 (82, 89)	6.29	9186	19.61	114	17.47

Bibliography

Adriani, Alberto et al. (Nov. 2017). "JIRAM, the Jovian Infrared Auroral Mapper". In: *Space Science Reviews* 213.1, pp. 393–446. ISSN: 1572-9672. DOI: 10.1007/s11214-014-0094-y.

Allegrini, F. et al. (2017). "Electron Beams and Loss Cones in the Auroral Regions of Jupiter". In: *Geophysical Research Letters* 44.14, pp. 7131–7139. ISSN: 1944-8007. DOI: 10.1002/2017GL073180.

Allegrini, F. et al. (2020). "First Report of Electron Measurements During a Europa Footprint Tail Crossing by Juno". In: *Geophysical Research Letters* 47.18, e2020GL089732. ISSN: 1944-8007. DOI: 10.1029/2020GL089732.

Asmar, Sami W. et al. (Nov. 2017). "The Juno Gravity Science Instrument". In: *Space Science Reviews* 213.1, pp. 205–218. ISSN: 1572-9672. DOI: 10.1007/s11214-017-0428-7.

Bagenal, F. et al. (Nov. 2017). "Magnetospheric Science Objectives of the Juno Mission". In: *Space Science Reviews* 213.1, pp. 219–287. ISSN: 1572-9672. DOI: 10.1007/s11214-014-0036-8.

Bagenal, Fran (2013). "Planetary Magnetospheres". In: *Planets, Stars and Stellar Systems: Volume 3: Solar and Stellar Planetary Systems*. Dordrecht: Springer Netherlands, pp. 251–307. ISBN: 978-94-007-5606-9. DOI: 10.1007/978-94-007-5606-9_6. URL: https://doi.org/10.1007/978-94-007-5606-9_6.

Bagenal, Fran and Steve Bartlett (2013). *Jupiter's Magnetosphere*. URL: https://lasp.colorado.edu/home/mop/resources/graphics/.

Bhattacharyya, Dolon et al. (Jan. 2018). "Evidence for Auroral Emissions From Callisto's Footprint in HST UV Images". In: *Journal of Geophysical Research: Space Physics* 123.1, pp. 364–373. ISSN: 21699380. DOI: 10.1002/2017JA024791.

Bolton, S. J. et al. (Nov. 2017). "The Juno Mission". In: *Space Science Reviews* 213.1, pp. 5–37. ISSN: 1572-9672. DOI: 10.1007/s11214-017-0429-6.

Bonfond, B. et al. (Mar. 2008). "UV Io Footprint Leading Spot: A Key Feature for Understanding the UV Io Footprint Multiplicity?" In: *Geophysical Research Letters* 35.5. ISSN: 1944-8007. DOI: 10.1029/2007GL032418.

Bonfond, B. et al. (2011). "Quasi-Periodic Polar Flares at Jupiter: A Signature of Pulsed Dayside Reconnections?" In: *Geophysical Research Letters* 38.2. ISSN: 1944-8007. DOI: 10.1029/2010GL045981.

Bonfond, B. et al. (2012). "Auroral Evidence of Io's Control over the Magnetosphere of Jupiter". In: *Geophysical Research Letters* 39.1. ISSN: 1944-8007. DOI: 10.1029/2011GL050253.

Bonfond, B. et al. (Nov. 2013a). "Evolution of the Io Footprint Brightness I: Far-UV Observations". In: *Planetary and Space Science*. Atmospheres, Magnetospheres and Surfaces of the Outer Planets, Their Satellites and Ring Systems: Part IX 88, pp. 64–75. ISSN: 0032-0633. DOI: 10.1016/j.pss.2013.05.023.

Bonfond, B. et al. (Oct. 2013b). "The Multiple Spots of the Ganymede Auroral Footprint". In: *Geophysical Research Letters* 40.19, pp. 4977–4981. ISSN: 1944-8007. DOI: 10.1002/grl.50989.

Bonfond, B. et al. (Oct. 2015). "The Far-Ultraviolet Main Auroral Emission at Jupiter – Part 2: Vertical Emission Profile". In: *Annales Geophysicae* 33.10, pp. 1211–1219. ISSN: 0992-7689. DOI: 10.5194/angeo-33-1211-2015.

Bonfond, B. et al. (2016). "Dynamics of the Flares in the Active Polar Region of Jupiter". In: *Geophysical Research Letters* 43.23, pp. 11,963–11,970. ISSN: 1944-8007. DOI: 10.1002/2016GL071757.

Bonfond, B. et al. (2017). "Morphology of the UV Aurorae Jupiter during Juno's First Perijove Observations". In: *Geophysical Research Letters* 44.10, pp. 4463–4471. ISSN: 1944-8007. DOI: 10.1002/2017GL073114.

Bonfond, B. et al. (2018). "Bar Code Events in the Juno-UVS Data: Signature ∼10 MeV Electron Microbursts at Jupiter". In: *Geophysical Research Letters* 45.22, pp. 12,108–12,115. ISSN: 1944-8007. DOI: 10.1029/2018GL080490.

Bonfond, Bertrand, Zhonghua Yao, and Denis Grodent (2020). "Six Pieces of Evidence Against the Corotation Enforcement Theory to Explain the Main Aurora at Jupiter". In: *Journal of Geophysical Research: Space Physics* 125.11, e2020JA028152. ISSN: 2169-9402. DOI: 10.1029/2020JA028152.

Bunce, E. J., S. W. H. Cowley, and T. K. Yeoman (2004). "Jovian Cusp Processes: Implications for the Polar Aurora". In: *Journal of Geophysical Research: Space Physics* 109.A9. ISSN: 2156-2202. DOI: 10.1029/2003JA010280.

Chen, Francis F. (2016). "Introduction". In: *Introduction to Plasma Physics and Controlled Fusion*. Ed. by Francis F. Chen. Cham: Springer International Publishing, pp. 1–18. ISBN: 978-3-319-22309-4. DOI: 10.1007/978-3-319-22309-4_1.

Clarke, J. T. et al. (Feb. 2002). "Ultraviolet Emissions from the Magnetic Footprints of Io, Ganymede and Europa on Jupiter". In: *Nature* 415.6875, pp. 997–1000. ISSN: 1476-4687. DOI: 10.1038/415997a.

Clarke, J. T. et al. (2009). "Response of Jupiter's and Saturn's Auroral Activity to the Solar Wind". In: *Journal of Geophysical Research: Space Physics* 114.A5. ISSN: 2156-2202. DOI: 10.1029/2008JA013694.

Clarke, John T. et al. (2004). "Jupiter's Aurora". In: *Jupiter. The Planet, Satellites and Magnetosphere*. Ed. by F. Bagenal, T. E. Dowling, and W. B. McKinnon. Cambridge University Press, pp. 639–670. ISBN: 978-0-521-81808-7.

Connerney, J. E. P. (1981). "The Magnetic Field of Jupiter: A Generalized Inverse Approach". In: *Journal of Geophysical Research: Space Physics* 86.A9, pp. 7679–7693. ISSN: 2156-2202. DOI: 10.1029/JA086iA09p07679.

Connerney, J. E. P. et al. (1998). "New Models of Jupiter's Magnetic Field Constrained by the Io Flux Tube Footprint". In: *Journal of Geophysical Research: Space Physics* 103.A6, pp. 11929–11939. ISSN: 2156-2202. DOI: 10.1029/97JA03726.

Connerney, J. E. P. et al. (May 2017a). "Jupiter's Magnetosphere and Aurorae Observed by the Juno Spacecraft during Its First Polar Orbits". In: *Science* 356.6340, pp. 826–832. ISSN: 0036-8075, 1095-9203. DOI: 10.1126/science.aam5928.

Connerney, J. E. P. et al. (Nov. 2017b). "The Juno Magnetic Field Investigation". In: *Space Science Reviews* 213.1, pp. 39–138. ISSN: 1572-9672. DOI: 10.1007/s11214-017-0334-z.

Connerney, J. E. P. et al. (2018). "A New Model of Jupiter's Magnetic Field From Juno's First Nine Orbits". In: *Geophysical Research Letters* 45.6, pp. 2590–2596. ISSN: 1944-8007. DOI: 10.1002/2018GL077312.

Connerney, J. E. P. et al. (2020). "A Jovian Magnetodisc Model for the Juno Era". In: *Journal of Geophysical Research: Space Physics* 125.10, e2020JA028138. ISSN: 2169-9402. DOI: 10.1029/2020JA028138.

Connerney, J. E. P. et al. (2022). "A New Model of Jupiter's Magnetic Field at the Completion of Juno's Prime Mission". In: *Journal of Geophysical Research: Planets* 127.2, e2021JE007055. ISSN: 2169-9100. DOI: 10.1029/2021JE007055.

Cowley, S. W. H. and E. J. Bunce (Aug. 2001). "Origin of the Main Auroral Oval in Jupiter's Coupled Magnetosphere–Ionosphere System". In: *Planetary and Space Science*. Magnetosphere of the Outer Planets Part II 49.10, pp. 1067–1088. ISSN: 0032-0633. DOI: 10.1016/S0032-0633(00)00167-7.

Cowley, S. W. H. et al. (2003). "Jupiter's Polar Ionospheric Flows: Theoretical Interpretation". In: *Geophysical Research Letters* 30.5. ISSN: 1944-8007. DOI: 10.1029/2002GL016030.

Delamere, P. A. and F. Bagenal (2010). "Solar Wind Interaction with Jupiter's Magnetosphere". In: *Journal of Geophysical Research: Space Physics* 115.A10. ISSN: 2156-2202. DOI: 10.1029/2010JA015347.

— (2013). "Magnetotail Structure of the Giant Magnetospheres: Implications of the Viscous Interaction with the Solar Wind". In: *Journal of Geophysical Research: Space Physics* 118.11, pp. 7045–7053. ISSN: 2169-9402. DOI: 10.1002/2013JA019179.

Desroche, M. et al. (2012). "Conditions at the Expanded Jovian Magnetopause and Implications for the Solar Wind Interaction". In: *Journal of Geophysical Research: Space Physics* 117.A7. ISSN: 2156-2202. DOI: 10.1029/2012JA017621.

Dumont, M. et al. (2014). "Jupiter's Equatorward Auroral Features: Possible Signatures of Magnetospheric Injections". In: *Journal of Geophysical Research: Space Physics* 119.12, pp. 10,068–10,077. ISSN: 2169-9402. DOI: 10.1002/2014JA020527.

Dungey, J. W. (Jan. 1961). "Interplanetary Magnetic Field and the Auroral Zones". In: *Physical Review Letters* 6.2, pp. 47–48. DOI: 10.1103/PhysRevLett.6.47.

Dunn, W. R. et al. (Nov. 2017). "The Independent Pulsations of Jupiter's Northern and Southern X-ray Auroras". In: *Nature Astronomy* 1.11, pp. 758–764. ISSN: 2397-3366. DOI: 10.1038/s41550-017-0262-6.

Dunn, W. R. et al. (2020). "Comparisons Between Jupiter's X-ray, UV and Radio Emissions and In-Situ Solar Wind Measurements During 2007". In: *Journal of Geophysical Research: Space Physics* 125.6, e2019JA027222. ISSN: 2169-9402. DOI: 10.1029/2019JA027222.

Dunn, William R. et al. (2016). "The Impact of an ICME on the Jovian X-ray Aurora". In: *Journal of Geophysical Research: Space Physics* 121.3, pp. 2274–2307. ISSN: 2169-9402. DOI: 10.1002/2015JA021888.

Ebert, R. W. et al. (2019). "Comparing Electron Energetics and UV Brightness in Jupiter's Northern Polar Region During Juno Perijove 5". In: *Geophysical Research Letters* 46.1, pp. 19–27. ISSN: 1944-8007. DOI: 10.1029/2018GL081129.

Elliott, S. S. et al. (2018a). "Pitch Angle Scattering of Upgoing Electron Beams in Jupiter's Polar Regions by Whistler Mode Waves". In: *Geophysical Research Letters* 45.3, pp. 1246–1252. ISSN: 1944-8007. DOI: 10.1002/2017GL076878.

Elliott, S. S. et al. (2018b). "The Acceleration of Electrons to High Energies Over the Jovian Polar Cap via Whistler Mode Wave-Particle Interactions". In: *Journal of Geophysical Research: Space Physics* 123.9, pp. 7523–7533. ISSN: 2169-9402. DOI: 10.1029/2018JA025797.

Elliott, S. S. et al. (2020). "The Generation of Upward-Propagating Whistler Mode Waves by Electron Beams in the Jovian Polar Regions". In: *Journal of Geophysical Research: Space Physics* 125.6, e2020JA027868. ISSN: 2169-9402. DOI: 10.1029/2020JA027868.

Elsner, R. F. et al. (2005). "Simultaneous Chandra X Ray, Hubble Space Telescope Ultraviolet, and Ulysses Radio Observations of Jupiter's Aurora". In: *Journal of Geophysical Research: Space Physics* 110.A1. ISSN: 2156-2202. DOI: 10.1029/2004JA010717.

Gérard, J.-C. et al. (2014). "Mapping the Electron Energy in Jupiter's Aurora: Hubble Spectral Observations". In: *Journal of Geophysical Research: Space Physics* 119.11, pp. 9072–9088. ISSN: 2169-9402. DOI: 10.1002/2014JA020514.

Gérard, J.-C. et al. (2019). "Contemporaneous Observations of Jovian Energetic Auroral Electrons and Ultraviolet Emissions by the Juno Spacecraft". In: *Journal of Geophysical Research: Space Physics* 124.11, pp. 8298–8317. ISSN: 2169-9402. DOI: 10.1029/2019JA026862.

Gladstone, G. R. et al. (Feb. 2002). "A Pulsating Auroral X-ray Hot Spot on Jupiter". In: *Nature* 415.6875, pp. 1000–1003. ISSN: 1476-4687. DOI: 10.1038/4151000a.

Gladstone, G. Randall et al. (Nov. 2017). "The Ultraviolet Spectrograph on NASA's Juno Mission". In: *Space Science Reviews* 213.1-4, pp. 447–473. ISSN: 0038-6308, 1572-9672. DOI: 10.1007/s11214-014-0040-z.

Gray, R. L. et al. (2017). "Characterization of Jupiter's Secondary Auroral Oval and Its Response to Hot Plasma Injections". In: *Journal of Geophysical Research: Space Physics* 122.6, pp. 6415–6429. ISSN: 2169-9402. DOI: 10.1002/2017JA024214.

Greathouse, T. K. et al. (Sept. 2013). "Performance Results from In-Flight Commissioning of the Juno Ultraviolet Spectrograph (Juno-UVS)". In: *UV, X-Ray, and Gamma-Ray Space Instrumentation for Astronomy XVIII*. Vol. 8859. International Society for Optics and Photonics, 88590T. DOI: 10.1117/12.2024537.

Greathouse, Thomas et al. (2021). "Local Time Dependence of Jupiter's Polar Auroral Emissions Observed by Juno UVS". In: *Journal of Geophysical Research: Planets* 126.12, e2021JE006954. ISSN: 2169-9100. DOI: 10.1029/2021JE006954.

Grodent, D. et al. (Nov. 2003a). "Jupiter's Main Auroral Oval Observed with HST-STIS". In: *Journal of Geophysical Research: Space Physics* 108.A11. ISSN: 2156-2202. DOI: 10.1029/2003JA009921.

Grodent, D. et al. (2003b). "Jupiter's Polar Auroral Emissions". In: *Journal of Geophysical Research: Space Physics* 108.A10. ISSN: 2156-2202. DOI: 10.1029/2003JA010017.

Grodent, Denis (Apr. 2015). "A Brief Review of Ultraviolet Auroral Emissions on Giant Planets". In: *Space Science Reviews* 187.1, pp. 23–50. ISSN: 1572-9672. DOI: 10.1007/s11214-014-0052-8.

Grodent, Denis et al. (2008). "Jupiter's Changing Auroral Location". In: *Journal of Geophysical Research: Space Physics* 113.A1. ISSN: 2156-2202. DOI: 10.1029/2007JA012601.

Gurnett, D. A. and A. Bhattacharjee (2005a). "Characteristic parameters of a plasma". In: *Introduction to Plasma Physics: With Space and Laboratory Applications*. Cambridge University Press, 5–22. DOI: 10.1017/CBO9780511809125.003.

— (2005b). "Single-Particle Motions". In: *Introduction to Plasma Physics: With Space and Laboratory Applications*. Cambridge University Press, 23–74. DOI: 10.1017/CBO9780511809125.004.

Gustin, J. et al. (2004). "Energy-Flux Relationship in the FUV Jovian Aurora Deduced from HST-STIS Spectral Observations". In: *Journal of Geophysical Research: Space Physics* 109.A10. ISSN: 2156-2202. DOI: 10.1029/2003JA010365.

Gustin, J. et al. (2006). "Characteristics of Jovian Morning Bright FUV Aurora from Hubble Space Telescope/Space Telescope Imaging Spectrograph Imaging and Spectral Observations". In: *Journal of Geophysical Research: Space Physics* 111.A9. ISSN: 2156-2202. DOI: 10.1029/2006JA011730.

Gustin, J. et al. (2012). "Conversion from HST ACS and STIS Auroral Counts into Brightness, Precipitated Power, and Radiated Power for H2 Giant Planets". In: *Journal of Geophysical Research: Space Physics* 117.A7. ISSN: 2156-2202. DOI: 10.1029/2012JA017607.

Gustin, J. et al. (Sept. 2013). "Effects of Methane on Giant Planet's UV Emissions and Implications for the Auroral Characteristics". In: *Journal of Molecular Spectroscopy*. Methane Spectroscopy and Its Applications to Planetary Atmospheres, Including the Earth's 291, pp. 108–117. ISSN: 0022-2852. DOI: 10.1016/j.jms.2013.03.010.

Gustin, J. et al. (Apr. 2016). "Characteristics of North Jovian Aurora from STIS FUV Spectral Images". In: *Icarus* 268, pp. 215–241. ISSN: 0019-1035. DOI: 10.1016/j.icarus.2015.12.048.

Haewsantati, K. et al. (2021). "Morphology of Jupiter's Polar Auroral Bright Spot Emissions via Juno-UVS Observations". In: *Journal of Geophysical Research: Space Physics* 126.2, e2020JA028586. ISSN: 2169-9402. DOI: 10.1029/2020JA028586.

Hansen, C. J. et al. (Nov. 2017). "Junocam: Juno's Outreach Camera". In: *Space Science Reviews* 213.1, pp. 475–506. ISSN: 1572-9672. DOI: 10.1007/s11214-014-0079-x.

Hess, S. L. G. et al. (2011). "Model of the Jovian Magnetic Field Topology Constrained by the Io Auroral Emissions". In: *J. Geophys. Res.* 116.A15, A05217. DOI: 10.1029/2010JA016262.

Hill, T. W. (2001). "The Jovian Auroral Oval". In: *J. Geophys. Res.* 106, pp. 8101–8108. DOI: 10.1029/2000JA000302.

Hue, V. et al. (June 2018). "In-Flight Characterization and Calibration of the Juno-Ultraviolet Spectrograph (Juno-UVS)". In: *Proceedings of SPIE: The International Society for Optical Engineering*. ISSN: 0277-786X. DOI: 10.1117/12.2311563.

Hue, V. et al. (2021). "Detection and Characterization of Circular Expanding UV-Emissions Observed in Jupiter's Polar Auroral Regions". In: *Journal of Geophysical Research: Space Physics* 126.3, e2020JA028971. ISSN: 2169-9402. DOI: 10.1029/2020JA028971.

Jackman, C. M. et al. (2018). "Assessing Quasi-Periodicities in Jovian X-Ray Emissions: Techniques and Heritage Survey". In: *Journal of Geophysical Research: Space Physics* 123.11, pp. 9204–9221. ISSN: 2169-9402. DOI: 10.1029/2018JA025490.

Janssen, M. A. et al. (Nov. 2017). "MWR: Microwave Radiometer for the Juno Mission to Jupiter". In: *Space Science Reviews* 213.1, pp. 139–185. ISSN: 1572-9672. DOI: 10.1007/s11214-017-0349-5.

Joy, S. P. et al. (2002). "Probabilistic Models of the Jovian Magnetopause and Bow Shock Locations". In: *Journal of Geophysical Research: Space Physics* 107.A10, SMP 17–1–SMP 17–17. ISSN: 2156-2202. DOI: 10.1029/2001JA009146.

Khurana, K. K. et al. (2004). "The Configuration of Jupiter's Magnetosphere". In: *Jupiter. The Planet, Satellites and Magnetosphere*. Ed. by F. Bagenal, T. E. Dowling, and W. B. McKinnon. Cambridge University Press, pp. 593–616. ISBN: 978-0-521-81808-7.

Khurana, Krishan K. (1997). "Euler Potential Models of Jupiter's Magnetospheric Field". In: *Journal of Geophysical Research: Space Physics* 102.A6, pp. 11295–11306. ISSN: 2156-2202. DOI: 10.1029/97JA00563.

Kita, H. et al. (Dec. 2019). "Jovian UV Aurora's Response to the Solar Wind: Hisaki EXCEED and Juno Observations". In: *Journal of Geophysical Research: Space Physics* 124.12, pp. 10209–10218. ISSN: 2169-9380, 2169-9402. DOI: 10.1029/2019JA026997.

Kivelson, M. G. et al. (2004). "Magnetospheric Interactions with Satellites". In: *Jupiter. The Planet, Satellites and Magnetosphere*. Ed. by F. Bagenal, T. E. Dowling, and W. B. McKinnon. Cambridge University Press, pp. 513–536. ISBN: 978-0-521-81808-7.

Kivelson, Margaret G. and David J. Southwood (Nov. 2003). "First Evidence of IMF Control of Jovian Magnetospheric Boundary Locations: Cassini and Galileo Magnetic Field Measurements Compared". In: *Planetary and Space Science* 51.13, pp. 891–898. ISSN: 0032-0633. DOI: 10.1016/S0032-0633(03)00075-8.

Kolmašová, Ivana et al. (July 2018). "Discovery of Rapid Whistlers Close to Jupiter Implying Lightning Rates Similar to Those on Earth". In: *Nature Astronomy* 2.7, pp. 544–548. ISSN: 2397-3366. DOI: 10.1038/s41550-018-0442-z.

Kotsiaros, Stavros et al. (Oct. 2019). "Birkeland Currents in Jupiter's Magnetosphere Observed by the Polar-Orbiting Juno Spacecraft". In: *Nature Astronomy* 3.10, pp. 904–909. ISSN: 2397-3366. DOI: 10.1038/s41550-019-0819-7.

Kurth, W. S. et al. (Nov. 2017). "The Juno Waves Investigation". In: *Space Science Reviews* 213.1, pp. 347–392. ISSN: 1572-9672. DOI: 10.1007/s11214-017-0396-y.

Kurth, W. S. et al. (2018). "Whistler Mode Waves Associated With Broadband Auroral Electron Precipitation at Jupiter". In: *Geophysical Research Letters* 45.18, pp. 9372–9379. ISSN: 1944-8007. DOI: 10.1029/2018GL078566.

Lysak, R. L. et al. (2021). "The Jovian Ionospheric Alfvén Resonator and Auroral Particle Acceleration". In: *Journal of Geophysical Research: Space Physics* 126.12. e2021JA029886 2021JA029886, e2021JA029886. DOI: https://doi.org/10.1029/2021JA029886. eprint:

https://agupubs.onlinelibrary.wiley.com/doi/pdf/10.1029/2021JA029886. URL: https://agupubs.onlinelibrary.wiley.com/doi/abs/10.1029/2021JA029886.

MacDowall, R. J. et al. (Nov. 1993). "Quasiperiodic Jovian Radio Bursts: Observations from the Ulysses Radio and Plasma Wave Experiment". In: *Planetary and Space Science*. Special Issue: Ulysses Flyby of Jupiter 41.11, pp. 1059–1072. ISSN: 0032-0633. DOI: 10.1016/0032-0633(93)90109-F.

Manners, H., A. Masters, and J. N. Yates (2018). "Standing Alfvén Waves in Jupiter's Magnetosphere as a Source of ∼10- to 60-Min Quasiperiodic Pulsations". In: *Geophysical Research Letters* 45.17, pp. 8746–8754. ISSN: 1944-8007. DOI: 10.1029/2018GL078891.

Masters, A. et al. (2021). "Magnetic Reconnection Near the Planet as a Possible Driver of Jupiter's Mysterious Polar Auroras". In: *Journal of Geophysical Research: Space Physics* 126.8, e2021JA029544. ISSN: 2169-9402. DOI: 10.1029/2021JA029544.

Mauk, B. H. et al. (Feb. 2002). "Transient Aurora on Jupiter from Injections of Magnetospheric Electrons". In: *Nature* 415.6875, pp. 1003–1005. ISSN: 1476-4687. DOI: 10.1038/4151003a.

Mauk, B. H. et al. (Sept. 2017a). "Discrete and Broadband Electron Acceleration in Jupiter's Powerful Aurora". In: *Nature* 549.7670, pp. 66–69. ISSN: 1476-4687. DOI: 10.1038/nature23648.

Mauk, B. H. et al. (Nov. 2017b). "The Jupiter Energetic Particle Detector Instrument (JEDI) Investigation for the Juno Mission". In: *Space Science Reviews* 213.1, pp. 289–346. ISSN: 1572-9672. DOI: 10.1007/s11214-013-0025-3.

Mauk, B. H. et al. (2018). "Diverse Electron and Ion Acceleration Characteristics Observed Over Jupiter's Main Aurora". In: *Geophysical Research Letters* 45.3, pp. 1277–1285. ISSN: 1944-8007. DOI: 10.1002/2017GL076901.

Mauk, B. H. et al. (2020). "Energetic Particles and Acceleration Regions Over Jupiter's Polar Cap and Main Aurora: A Broad Overview". In: *Journal of Geophysical Research: Space Physics* 125.3, e2019JA027699. ISSN: 2169-9402. DOI: 10.1029/2019JA027699.

McComas, D. J. et al. (Nov. 2017). "The Jovian Auroral Distributions Experiment (JADE) on the Juno Mission to Jupiter". In: *Space Science Reviews* 213.1, pp. 547–643. ISSN: 1572-9672. DOI: 10.1007/s11214-013-9990-9.

McKibben, R. B., J. A. Simpson, and M. Zhang (Nov. 1993). "Impulsive Bursts of Relativistic Electrons Discovered during Ulysses' Traversal of Jupiter's Dusk-Side Magnetosphere". In: *Planetary and Space Science*. Special Issue: Ulysses Flyby of Jupiter 41.11, pp. 1041–1058. ISSN: 0032-0633. DOI: 10.1016/0032-0633(93)90108-E.

Nichols, J. D. et al. (2009a). "Observations of Jovian Polar Auroral Filaments". In: *Geophys. Res. Lett.* 36, p. 8101. DOI: 10.1029/2009GL037578.

Nichols, J. D. et al. (2009b). "Variation of Different Components of Jupiter's Auroral Emission". In: *Journal of Geophysical Research: Space Physics* 114.A6. ISSN: 2156-2202. DOI: 10.1029/2009JA014051.

Nichols, J. D. et al. (2017a). "Periodic Emission Within Jupiter's Main Auroral Oval". In: *Geophysical Research Letters* 44.18, pp. 9192–9198. ISSN: 1944-8007. DOI: 10.1002/2017GL074824.

Nichols, J. D. et al. (2017b). "Response of Jupiter's Auroras to Conditions in the Interplanetary Medium as Measured by the Hubble Space Telescope and Juno". In: *Geophysical Research Letters* 44.15, pp. 7643–7652. ISSN: 1944-8007. DOI: 10.1002/2017GL073029.

Pallier, Laurent and Renée Prangé (Aug. 2001). "More about the Structure of the High Latitude Jovian Aurorae". In: *Planetary and Space Science*. Magnetosphere of the Outer Planets Part II 49.10, pp. 1159–1173. ISSN: 0032-0633. DOI: 10.1016/S0032-0633(01)00023-X.

— (Mar. 2004). "Detection of the Southern Counterpart of the Jovian Northern Polar Cusp: Shared Properties". In: *Geophysical Research Letters* 31, p. L06701. DOI: 10.1029/2003GL018041.

Paranicas, C. et al. (2018). "Intervals of Intense Energetic Electron Beams Over Jupiter's Poles". In: *Journal of Geophysical Research: Space Physics* 123.3, pp. 1989–1999. ISSN: 2169-9402. DOI: 10.1002/2017JA025106.

Radioti, A. et al. (2009). "Equatorward Diffuse Auroral Emissions at Jupiter: Simultaneous HST and Galileo Observations". In: *Geophysical Research Letters* 36.7. ISSN: 1944-8007. DOI: 10.1029/2009GL037857.

Schneider, Nicholas M. and John T. Trauger (Sept. 1995). "The Structure of the Io Torus". In: *textbackslashapj* 450, p. 450. DOI: 10.1086/176155.

Schunk, Robert and Andrew Nagy (2009). "Wave phenomena". In: *Ionospheres: Physics, Plasma Physics, and Chemistry*. 2nd ed. Cambridge Atmospheric and Space Science Series. Cambridge University Press, 159–205. DOI: 10.1017/CBO9780511635342.006.

Serio, A. W. and J. T. Clarke (Sept. 2008). "The Variation of Io's Auroral Footprint Brightness with the Location of Io in the Plasma Torus". In: *Icarus* 197, pp. 368–374. DOI: 10.1016/j.icarus.2008.03.026.

Southwood, D. J. and M. G. Kivelson (2001). "A New Perspective Concerning the Influence of the Solar Wind on the Jovian Magnetosphere". In: *Journal of Geophysical Research: Space Physics* 106.A4, pp. 6123–6130. ISSN: 2156-2202. DOI: 10.1029/2000JA000236.

Tsurutani, Bruce T. and Gurbax S. Lakhina (1997). "Some Basic Concepts of Wave-Particle Interactions in Collisionless Plasmas". In: *Reviews of Geophysics* 35.4, pp. 491–501. ISSN: 1944-9208. DOI: 10.1029/97RG02200.

Vasyliunas, V. M. (1983). "Physics of the Jovian Magnetosphere". In: *Physics of the Jovian Magnetosphere*. Ed. by A. J. Dessler. Cambridge University Press, pp. 395–453.

Vogt, Marissa F. et al. (2011). "Improved Mapping of Jupiter's Auroral Features to Magnetospheric Sources". In: *Journal of Geophysical Research: Space Physics* 116.A3. ISSN: 2156-2202. DOI: 10.1029/2010JA016148.

Vogt, Marissa F. et al. (2015). "Magnetosphere-Ionosphere Mapping at Jupiter: Quantifying the Effects of Using Different Internal Field Models". In: *Journal of Geophysical Research: Space Physics* 120.4, pp. 2584–2599. ISSN: 2169-9402. DOI: 10.1002/2014JA020729.

Waite, J et al. (May 2001). "An Auroral Flare at Jupiter". In: *Nature* 410, pp. 787–9. DOI: 10.1038/35071018.

Wannawichian, S., J. T. Clarke, and J. D. Nichols (2010). "Ten Years of Hubble Space Telescope Observations of the Variation of the Jovian Satellites' Auroral Footprint Brightness". In: *Journal of Geophysical Research: Space Physics* 115.A2. ISSN: 2156-2202. DOI: 10.1029/2009JA014456.

Weigt, D. M. et al. (2020). "Chandra Observations of Jupiter's X-ray Auroral Emission During Juno Apojove 2017". In: *Journal of Geophysical Research: Planets* 125.4, e2019JE006262. ISSN: 2169-9100. DOI: 10.1029/2019JE006262.

Weiss, J. W. (2004). "Appendix 2: Planetary Parameters". In: *Jupiter. The Planet, Satellites and Magnetosphere*. Ed. by F. Bagenal, T. E. Dowling, and W. B. McKinnon. Cambridge University Press, pp. 699–706. ISBN: 978-0-521-81808-7.

Wibisono, A. D. et al. (2020). "Temporal and Spectral Studies by XMM-Newton of Jupiter's X-ray Auroras During a Compression Event". In: *Journal of Geophysical Research: Space Physics* 125.5, e2019JA027676. ISSN: 2169-9402. DOI: 10.1029/2019JA027676.

Yung, Y. L. et al. (Mar. 1982). "H2 Fluorescence Spectrum from 1200 to 1700 A by Electron Impact - Laboratory Study and Application to Jovian Aurora". In: *The Astrophysical Journal* 254, pp. L65–L69. ISSN: 0004-637X. DOI: 10.1086/183757.

Zhang, Binzheng et al. (2021). "How Jupiter's Unusual Magnetospheric Topology Structures Its Aurora". In: *Science Advances* 7.15, eabd1204. DOI: 10.1126/sciadv.abd1204.

Zhu, B.X. et al. (2021). "Jupiter high-energy/high-latitude electron environment from Juno's JEDI and UVS science instrument background noise". In: *Nuclear Instruments and Methods in Physics Research Section A: Accelerators, Spectrometers, Detectors and Associated Equipment* 1002, p. 165244. ISSN: 0168-9002. DOI: https://doi.org/10.1016/j.nima.2021.165244. URL: https://www.sciencedirect.com/science/article/pii/S016890022100228X.